UNIVERSITY OF SOUTHAMPTON

BRIDGING THE PRESSURE GAP: TAKING SURFACE SCIENCE TO MORE REALISTIC PRESSURES

By David John Gilbert Quin

A Thesis submitted for the Degree of Doctor of Philosophy

FACULTY OF ENGINEERING, SCIENCE AND MATHEMATICS
School of Chemistry

UNIVERSITY OF SOUTHAMPTON

ABSTRACT

FACULTY OF ENGINEERING, SCIENCE AND MATHEMATICS
School of Chemistry
Doctor of Philosophy

BRIDGING THE PRESSURE GAP: TAKING SURFACE SCIENCE TO MORE REALISTIC PRESSURES

By David John Gilbert Quin

Traditional surface science experiments are conducted under ultra high vacuum conditions, this enables surface cleanliness to be strictly controlled and the use of electron based measurements, to determine surface structure and composition. Unfortunately, UHV conditions are very different from those in real world catalysis (e.g. car exhaust clean-up) and only limited insight can be obtained from such studies. For example, it has been found that certain catalytic species do not exist under UHV conditions. It is an essential step in the progression of surface science to move to more realistic conditions whilst still retaining the simplicity enabled by a UHV cleaned, ideal surface such as a single crystal. Within this thesis the development of two new pieces of equipment, which bridge this gap, at the SRS at Daresbury Laboratory are presented.

The High Pressure Reaction Cell (HPRC), based on the far-IR beamline 13.3 at Daresbury laboratory, enables samples to be cleaned under UHV conditions before being exposed to pressures, inside the cell, of up to 200 mbar of a chosen gas, without compromising the external vacuum. Far-IR RAIRS, which is useful for adsorbate investigations, is unaffected by the presence of a partial pressure of gas, enabling *in-situ* measurements as well as post-experiment UHV measurements. Results are presented for investigations into the high pressure oxidation and reduction of copper, these are supported by DFT calculations of the phonon modes for common copper oxides.

The High Ambient Pressure Photoelectron spectroscopY (HAPPY) system is a peripatetic end station designed to allow sample cleaning in UHV, before performing *in-situ* photoelectron spectroscopy at pressures up to 10^{-2} mbar. The commissioning experiments in which a commercial supported catalyst was studied are presented.

The future of these two newly developed pieces of equipment is discussed alongside the future of far-IR RAIRS as a whole.

TABLE OF CONTENTS

Acknowledgements

Primarily thanks must go to Dr. Andrea Russell and Dr. Mark Surman. Without these two guiding lights, in both an academic and an emotional sense, it is unlikely this thesis would have ever come to fruition. The absence of their ability to keep me on track will hopefully not be too greatly missed in future years!

I would like to thank the CCLRC for the research studentship. Additional thanks goes to those who helped with the academic side in Daresbury, specifically with the calculations from Adrian and Barry, with the HPRC and HAPPY from John P, Sunil, John F, Ian K, Ian B and Terry. To those who survived the experimental times; Nicholas, Anna and Louisa. To the Friday Ring of Bells crew, who always managed to turn a stormy mood around and finally to the many members of the catering services who, over the years, whilst not necessarily agreeing with their menu choices, often made me feel like part of the family! To Mike Busuttil, with whom I spent the best moments in Daresbury, never has an off-line area seemed so comfy or the tower so inviting!

Past members of the Russell group for passing on their wisdom over the years, specifically Chris for proving far-IR RAIRS is survivable! Richard and Helen – one for being silent but deadly (at sport) and the other for being not so silent especially regarding cake rotas, thanks also to Abbe, Gurjit and Sohrab. Current members who I haven't enough space to do justice to – Piotr, Gael, Praba, Dai and Fab, I wish you luck in your future endeavours. To Kate for her excessive use of the "W" word! To Suzanne for allowing us to discuss her award winning spheres. To Colin for reminding me that most things are best done with confidence, and to Peter who would never have allowed me to become overconfident!

Equally I can not think of a group of friends, external to my Ph.D., more deserving of the thanks that I will inadequately supply. To those I have lived with, aside from whom, special mentions go to Charlie, Mike, Jon, Katy, Shez and even to Abi who helped as much as she hindered. All have been there for support or a dose of normality when required, along with so many others.

Finally to my loving parents and the rest of my family, to those present at the start and to those who have swelled the ranks along the way.

Thank you all!

Chapter One – Introduction

This thesis is primarily concerned with developing methods to shift experimental focus from ultra high vacuum (UHV) techniques into more realistic conditions. Focussing on the widely studied oxidation of copper, the data obtained using far-infrared reflection absorption infrared spectroscopy (RAIRS), combined with complementary electronic structure calculations, can easily be compared to previously published results, to illustrate the added benefits of the new technique. A photoelectron spectrometer also capable of non-UHV operation was developed, the spectra of a real catalyst at high ambient pressures has been performed to demonstrate the capabilities of these new pieces of equipment available at the SRS at Daresbury laboratory.

1.1 Why use ultra high vacuum conditions?

Catalytic systems can often be highly complex and difficult to understand due to the large number of different parameters affecting the reaction. Traditional surface science experiments aim to simplify these parameters by observing reactions in UHV conditions and on idealised surfaces. Experiments under UHV conditions are defined here as those performed at pressures close to 1×10^{-10} mbar.

There are two main reasons behind the use of UHV conditions experimentally. Firstly pressures as low as these enable a surface to be cleaned to an atomic level, this level of cleanliness can be maintained for hours in pressures around 10^{-10} mbar. If the pressure was even as high as 1×10^{-6} mbar the surface would be bombarded at a rate of approximately 10^{14} to 10^{15} molecules cm^{-2} s^{-1} and would become contaminated within a matter of seconds [1]. The second reason to use a UHV environment is that many of the techniques used in surface science are electron based and as such require UHV conditions to operate, due to the massive reduction in the electron mean free path as the pressure increases. Many surface science experiments under UHV conditions are conducted with single crystal surfaces. Using these idealised surfaces instead of poly-crystalline samples means the structure of the surface is well known and reasonable conclusions regarding the active sites present on the clean surface can be drawn. Using a combination of these two features, surface science experiments have been highly successful over the years, providing valuable insight into many catalytic and reaction systems. However, it is worth taking note of the obvious differences between these idealised conditions and the conditions faced in real world catalysis.

1.2 The pressure and material 'gaps'

Misinterpretation of data can arise due to pressure and material 'gaps'; these are terms used to describe experimental discrepancies: those between idealised single crystals and polycrystalline samples, the material gap, and those between UHV and real-life pressures, the pressure gap.

A well known example of the pressure gap regards the oxidation of carbon monoxide over ruthenium. When atomically clean Ru single crystals are considered under UHV conditions it is found that they are amongst the worst catalysts for CO oxidation. However, under atmospheric conditions it is found that ruthenium surfaces become excellent CO oxidation catalysts [2]. It was discovered later that this was due to the formation of a (1 x 1) O adlayer present on the surface of the Ru which is consumed during the reaction but rapidly replaced under atmospheric pressures [3].

1.3 The achievements of far-IR RAIRS

Synchrotron radiation far-IR Reflection Absorption Infrared Spectroscopy (RAIRS) can be a very powerful tool when used to observe adsorbates at metal surfaces, due to the very high sensitivity and good resolution it offers. The technique has provided insight into many adsorbate systems, revealing information regarding adsorption sites, orientations and relaxation processes. The far-IR region is largely concerned with the metal adsorbate bonds, the peak position caused by the same adsorbate on the same surface can shift noticeably depending on which adsorption site is occupied. With a very successful experiment, sub-monolayer quantities are detectable using RAIRS, indicating what an incredible tool the technique can be.

Before the introduction of synchrotron radiation as the source for the RAIRS experiment the technique was largely limited to wavelengths above 400 cm^{-1}. Despite these issues a number of papers regarding the carbon-metal stretch of CO/Pt(111) were produced during the late 80s [4, 5], closely followed by a few investigations on polycrystalline Ag [6, 7]. With the introduction of synchrotron radiation the spectral range of wavelengths was extended and collection times greatly reduced as discussed in further detail in Chapter 2. This development led to some very interesting and ground breaking work. The first work using this new source was published in the early 90s by Hirschmugl *et al.*[8] the authors presented data from 180 to 500 cm^{-1} for the first time. With this extended spectral range the Cu-CO stretch was assigned for CO adsorbed on both Cu(100) and Cu(111) as well as a band assigned to a coupling from the normally forbidden frustrated CO rotation to an adsorption band. As the technique improved further work by the same group showed the importance of being able to probe the metal adsorbate bonds. Using a mixed isotope gas feed Hirschmugl *et al.*[9] presented appreciable differences in the Cu-CO isotopic stretches using SR-RAIRS.

The sensitivity of SR-RAIRS is a major selling point. Work by Raval *et al.*[10] presented evidence not only of submonolayers of adsorbate, but also that complex organic adsorbates could be detected as well as the simple molecules previously investigated. Whilst monitoring the deprotonation of formic acid over Cu(110), two Cu-O vibrations were detected and assigned to two chemically distinct formate species. The second important feature of this work is the detection of a species which is adsorbed to the surface by more than one bond, in this case the formate species. The group furthered this research by investigating larger molecules which can also bond to the copper surface via two oxygen atoms. In a recent paper β-ketoesters were investigated in the form of acetylacetone (AA), methylacetoacetone (MAA) and (R,R)-tartaric acid on Cu(110) [11]. It was shown with this paper that as the molecular body attached to the oxygen atom increases the stretching frequency measured tends towards lower wavenumbers as would be expected. This trend is illustrated in figure 1.1.

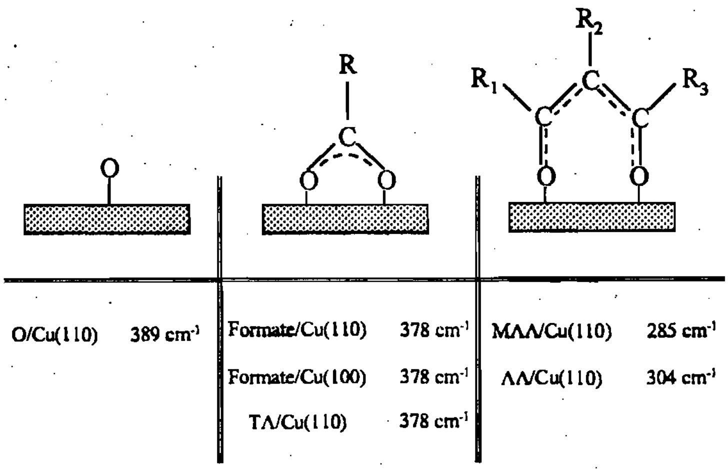

Figure 1.1 – Summary of Cu-O bands observed by Humblot *et al.*[11]

A final excellent example of the success of SR Far-IR RAIRS comes from the identification of the lifting of the reconstruction of the Pt(110) surface when exposed to CO. The clean Pt(110) surface had been shown previously, by low energy electron diffraction (LEED) [12], to reconstruct from the (1 x 1) face to a (1 x 2) "missing row" structure. This structure has been shown to lift when exposed to CO at 300 K, but upon adsorption at 250 K it had been suggested that the lifting of this reconstruction does not occur [13]. Work by Baily *et al.*[14] showed that small islands of the surface start to reform the (1 x 1) surface at temperatures as low as 204 K, 50 K lower than previously reported. It is hypothesised that the need for moderately long range order on the surface, when using LEED, meant the start of the lifting of the reconstruction goes unnoticed until being investigated by the much higher sensitivity of RAIRS.

RAIRS is a photon based technique and as such can easily combine UHV cleanliness with more realistic pressures. Generally a second smaller chamber is attached to the main body of the UHV experimental vessel, the samples are transferred from one chamber to the other and the chamber sealed. This enables the smaller chamber to be raised to pressures above what would normally be usable in a standard UHV chamber. This method has been used in conjunction with polarization modulation techniques by Goodman *et al.*[15] The drawback of having a side chamber attached to the main UHV vessel is that it can lead to an extended time period between experiments performed in UHV and those performed in the second chamber. If a set-up removed the need to transfer the sample between manipulators it may be possible to reduce this timescale.

1.4 The achievements of PES

X-ray photoelectron spectroscopy (XPS) and ultraviolet photoelectron spectroscopy (UPS) are used far more commonly in surface science than RAIRS. Both techniques provide information regarding the surface composition of a sample.

Not only can XPS detect any element with an atomic number above three, i.e. only hydrogen and helium are undetectable, but it also has a detection limit in the range of parts per thousand, making it a very powerful technique. In fact, nowadays, most UHV chambers will have an XPS system as standard to monitor surface contamination. Four major factors were involved in bringing XPS to the forefront of scientific experimentation. In 1887 Heinrich Hertz [16] discovered the photoelectric effect, discussed in greater detail in chapter 2, this effect is the backbone of XPS theory. However it was not until 1895 that X-rays were discovered by Röntgen [17], for many years they were termed Röntgen rays as shown in 1907, when P. D. Innes managed to record broad bands of electrons as a function of energy during one of his experiments “under the influence of Röntgen rays” [18], which, in essence, is the first XPS spectrum. However, the information provided by this spectrum was unclear and many experiments were performed to try and provide greater insight. It took until 1967 for sufficient enhancements to the technique to be put in place, when Siegbahn *et al.* published an overview of XPS as a technique including a number of high resolution spectra [19]. This work among other associated achievements led to him being awarded the Nobel prize, acknowledging his contribution in developing one of the most important techniques known to science.

With XPS being such an important technique it has, unsurprisingly, provided many important insights for the scientific community over the years. In the early seventies large volumes of work were published showing that the core-electron binding energies of a range of elements were sensitive to the chemical environment [20, 21]. Stainless steels are a highly important group of materials, being used for a wide array of applications, the chemical resistance and passivity of samples of different types of stainless steel, and as such where possible applications lie, are often investigated utilising the surface sensitivity of XPS [22]. Several techniques exist as side branches to XPS which allow the non-destructive depth analysis of thin films to be analysed, the development and subsequent uses of angle-resolved XPS (ARXPS) [23] and the controlled surface charging method proposed by Doron-Mor *et al.*[24] have broadened the uses of XPS yet further. Being such a versatile technique it is no surprise to find XPS being used by some of the major institutions of the world, for example a recent report details how NASA used the technique in combination with a number of other surface science techniques to investigate the tragic loss of the space shuttle Columbia in 2003 [25].

The UPS technique also reached maturity in the 60s with the first UPS valence band spectrum on copper being presented by Spicer *et al.*[26] with the first gas phase spectroscopy being performed by the Turner group [27] using equipment, the basis of which, is still used today. The simplest and most important information derived from UPS is the ionization energies for valence electrons. Many of the important discoveries within surface science using UPS have been performed by Eastman and co-workers, presenting spectra of CO exposed to Ni(100) [28], Ti [29] and W(100) [30]. It was shown that on Ni, resonances are observed which are comparable with those expected for free CO, whereas this was not the case for Ti and W. It was concluded that CO disassociates on these two surfaces and atomic C and O can be observed in the UPS spectra instead. A similar conclusion was achieved by Atkinson *et al.* when considering the CO/Mo system, where CO adsorbs at 80 K but disassociates as the system is warmed [31]. The power of UPS is further evidenced when considering the difference spectra presented by Demuth and Eastman [32] where adsorbates are shown to be detectable on metal surfaces. The authors showed using this technique which orbitals were involved in the adsorption process. Combining calculations to model expected results with those obtained experimentally using angle-resolved UPS (ARUPS), further expands the information gained from this technique. Hofmann *et al.*[33] presented data proving the ability to detect the presence of a 26° tilt when CO adsorbs on a Pt(110) surface, as well as confirming the absence of a tilt when adsorbing CO upon the Pt(111) surface.

As well as such important discoveries PES plays a small part in other pieces of surface science research, often only being used to confirm that the early stages of an experiment have gone accordingly before the new science begins.

In recent years *in situ* PES systems have been designed, utilising differential pumping systems to enable more realistic sample pressures whilst allowing the detector to operate at relatively low pressures. Systems in the USA [34] and Germany [35] have been developed with great success, however not only did these systems take a long time in development, they were also constructed on the basis of a very large budget. Such restrictions mean that only a limited part of the scientific community can gain access to a highly useful resource.

1.5 Bridging the Pressure Gap Thus Far

Potentially more than 13 orders of magnitude in pressure can be the difference between experiments performed under traditional UHV surface science experiments and the conditions typically found in industrial applications. Despite this massive difference, a number of examples exist which indicate the success the surface science approach can lead to, not least of these surrounds the Haber-Bosch process and ammonia synthesis using an iron catalyst [36]. However the extension of surface science theory does not always prove successful. The reasons behind this can be simply illustrated in two main areas.

Extrapolating UHV data to higher pressure conditions will not take into account thermodynamic and kinetic energy barriers. The higher pressure conditions may lead to new phases being thermodynamically favourable, it is possible these new phases are catalytically more reactive, or conversely, less reactive than the phases favoured at lower pressure, resulting in misleading results. The higher pressures may also favour certain reaction pathways which under traditional UHV conditions are kinetically unfavourable.

Surface science typically deals with fairly static conditions, these can be at odds with the non-equilibrium system represented in a catalysed reaction. It is possible these non-equilibrium conditions may affect the surface and by association the catalytic activity of the sample.

Due to these failings a concerted effort must be made to develop more *in situ* experimental methods as well as building more suitable model systems. Systems which are less complex than typical catalysis reactions, whilst still considering the features of the catalyst which directly affect the reaction. An excellent overview of the efforts made around the world following interdisciplinary routes can be found in a recent edition of PCCP [37], some of which is discussed here.

A range of techniques have been used in the literature to bridge the pressure gap including Sum Frequency Generation vibrational spectroscopy (SFG), X-ray Photoelectron Spectroscopy (XPS) and Scanning Tunneling Microscopy (STM).

SFG vibrational spectroscopy has the same immediate benefit as Reflection Absorbtion Infrared Spectroscopy (RAIRS) when considering the pressure gap, namely that it is a photon in-photon out technique, meaning the experiment can be performed at any pressure. SFG is a non-linear laser optical technique which obeys both the infrared (dipole) and Raman (polarisability) selection rules which makes it suitable for surface sensitive spectroscopy. Cremer *et al.* [38] were the first group to use SFG to monitor a catalytic reaction at high-pressure *in situ*, monitoring the hydrogenation of ethylene over a Pt(111) surface. Having shown that such *in situ* measurements could be obtained, the group investigated other hydrogenation reactions over Pt(111) [39, 40]. More recently SFG has shown that when exposing benzene to platinum surfaces, at pressures around 15 Torr, both chemisorbed and physisorbed species are present and that the interfacial structure of benzene depends upon which surface it is adsorbed upon [41, 42].

XPS is an electron based spectroscopic technique and therefore is strongly affected by the surrounding pressure. In order to compensate for this problem specially designed differential pumping systems have been constructed which enable high pressure XPS to be performed [34]. This equipment has been used, among other things, to monitor H_2/D_2 exchange upon Pt(111) and how it is affected by the presence of CO [43]. The authors illustrated that the binding energies of both C and O illustrated CO adsorbed in both atop and bridge positions, despite the knowledge that the room temperature structure was incommensurate with the Pt(111) surface. It was assumed that small displacements from those positions had relatively minor implications for the binding energies. Further examples of the work performed using high pressure XPS are discussed in Chapter 5.

Using STM it is possible to image the electronic structure of a small area which provides spatial information of individual atoms or molecules in real space. Although the STM uses electrons to probe the surface it is not affected by pressure due to the very small distances between surface and tip, which the electrons need to traverse. High Pressure STM was first utilised to bridge the pressure gap by McIntyre *et al.* [44] who developed a transfer system from UHV to the high pressure cell. The system was later improved to allow *in situ* HP-STM measurements up to 675 K [45]. Unfortunately despite the immediate potential of HP-STM there are a couple of limitations regarding the nature of work that can be performed. The time resolution of an STM image is limited to the scanning speed of the tunnelling tip, approximately 100 Å msec^{-1}. Under reaction conditions, a model catalyst surface is often covered by mobile adsorbate species which may diffuse too rapidly to be imaged by STM. Instead the reaction needs to be poisoned in order to reduce the mobility of the surface species. As such the technique is limited to spectator species adsorbed on the surface or conditions where the surface has low reactivity. Rider *et al.* have used HP-STM to show single molecule changes in the coverage of CO and NO co-adsorbed on Rh(111) [46]. The authors have also provided further evidence of how important it is to bridge the pressure gap by identifying a novel NO adsorption structure on Rh(111) which only occurs at high pressure [47]. Additionally other groups have used HP-STM to illustrate situations where the UHV surface science approach has been successful. Under UHV conditions it has been shown that H coverages on Cu(110) induce a (1 x 2) missing row reconstruction of the surface at room temperature [48]. However this is complicated by the low sticking probability of H_2 on Cu(110) at these temperatures. Compensated under UHV by pre-dissociation of H_2 or use of supersonic molecular beams it was theorised that the low sticking coefficient could be overcome by using a high flux of impinging molecules, i.e. *in situ* measurements at higher pressure of H_2. Österlund *et al.* [49] published images captured at 2 mbar H_2 which only showed the (1 x 1) structure and images captured at 20 mbar which showed both (1 x 1) and (2 x 1) regions, confirming the conclusions of the surface science experiments.

HP-STM has also been used to clear confusion regarding the possibility of a pressure gap in the NO/Pd(111) system. Ozensoy *et al.* used polarisation modulation reflection absorption infrared spectroscopy (PM-RAIRS) to investigate the system at a range of pressures. PM-RAIRS is a derivative of traditional RAIRS which uses polarised light combined with the inherent selection rules of RAIRS to investigate the difference between species adsorbed at surfaces and those in the gas phase. The technique is photon based and can be used at any pressure of gas, however, structural information is only inferred by PM-RAIRS and further experimental or theoretical data is required for confirmation. The authors noted considerable differences between spectra obtained at 13.3 mbar NO and 400 mbar NO over Pd [50]. Combining their data with DFT calculations the authors concluded that at higher pressures a new (3 x 3) NO structure was present, in comparison to the (2 x 2) coverage found in UHV studies [51]. Using HP-STM, Vang *et al.* [52] showed that the coverage of NO/Pd(111) at 720 mbar was in fact consistent with the (2 x 2) structure and could find no evidence for a (3 x 3) structure. Nor could the authors explain the difference observed in the spectra published by Ozensoy *et al.*

A final example of data which illustrates both the successes and failures of the surface science approach can be seen when considering an Au/Ni alloy. UHV studies of an Au/Ni(111) indicated that the alloy may be a better catalyst for the steam reforming of natural gas in comparison to the traditional Ni based catalyst. This is attributed to the impedence of Ni-C bonding by the presence of Au atoms. This theory was tested and a high surface area oxide supported Au/Ni catalyst was found to have increased durability for steam reforming [53]. This is another example of a successful extrapolation from surface science results to real life. However, more recently the system was viewed using HP-STM [54], it was found that under 1 bar of CO at RT the sample underwent severe structural changes. Gold clusters were seen to form upon the Ni(111) surface, an indication of a segregation occurring between the metals due to exposure of high pressures of CO. No phase separation has ever been observed under

UHV this is attributed to the fact that it is kinetically unfavourable at the low temperatures often used in surface science. This result also gives a clear illustration that it can be unwise to consider a surface as a static checkerboard in order to simplify understanding.

1.6 Thesis Outline

There is a steady progression, experimentally, to develop systems and techniques which can shift between UHV and atmospheric pressures and, as such, bridge the pressure gap. This thesis will continue the trend, describing two different pieces of newly developed equipment; the high pressure reaction cell (HPRC) for RAIRS and the high ambient pressure photoelectron spectroscopy (HAPPY) analyser, both of which were constructed at the SRS at Daresbury Laboratory, UK.

Chapter four of this thesis discusses the original development of the HPRC and the modifications made as experimentation continued. The HPRC allows experimental data to be collected in UHV and in pressures of gas up to 1 bar with a much shorter time delay in comparison to a separate chamber RAIRS system. Results are presented for the oxidation and reduction of a Cu(100) crystal in this high pressure environment monitored using far-IR RAIRS. Some supporting DFT calculations are also presented.

Chapter five covers the design of the HAPPY chamber and analyser which enables PES data to be collected up to 10^{-2} mbar, and was achieved at a fraction of the price of current available equipment. Some preliminary XPS data on a mounted sample of Pt/C is presented which confirms the potential of the system and the further development of the system is discussed. The intention was to go on to study the oxidation and reduction of the Cu surface using this system, unfortunately due to failures of the SRS combined with time constraints this was not possible.

1.7 References

1. McCash, E.M., *Surface Chemistry*. 2001, Oxford: Oxford University Press.
2. Peden, C.H.F. and Goodman, D.W., *J. Phys. Chem.*, 1986. **90**(7): p. 1360.
3. Peden, C.H.F., Goodman, D.W., Weisel, M.D., and Hoffmann, F.M., *Surf. Sci.*, 1991. **253**(1-3): p. 44.
4. Hoge, D., Tushaus, M., Schweizer, E., and Bradshaw, A.M., *Chem. Phys. Lett.*, 1988. **151**(3): p. 230.
5. Ryberg, R., *Phys. Rev. B*, 1989. **40**(12): p. 8567.
6. Wang, X.D. and Greenler, R.G., *Surf. Sci.*, 1990. **226**(1-2): p. L51.
7. Wang, X.D. and Greenler, R.G., *Phys. Rev. B*, 1991. **43**(8): p. 6808.
8. Hirschmugl, C.J., Williams, G.P., Hoffmann, F.M., and Chabal, Y.J., *Phys. Rev. Lett.*, 1990. **65**(4): p. 480.
9. Hirschmugl, C.J. and Williams, G.P., *Phys. Rev. B*, 1995. **52**(19): p. 14177.
10. Raval, R., Williams, J., Roberts, A.J., Nunney, T.S., and Surman, M., *Nuovo Cimento Soc. Ital. Fis. D-Condens. Matter At. Mol. Chem. Phys. Fluids Plasmas Biophys.*, 1998. **20**(4): p. 553.
11. Humblot, V., Bingham, C.J.A., Le Roux, D., Marti, E.M., McNutt, A., Nunney, T.S., Lorenzo, M.O., Roberts, A.J., Williams, J., Surman, M., and Raval, R., *Surf. Sci.*, 2003. **537**(1-3): p. 253.
12. Fery, P., Moritz, W., and Wolf, D., *Phys. Rev. B*, 1988. **38**(11): p. 7275.
13. Ferrer, S. and Bonzel, H.P., *Surf. Sci.*, 1982. **119**(2-3): p. 234.
14. Baily, C.J., Surman, M., and Russell, A.E., *Surf. Sci.*, 2003. **523**(1-2): p. 111.
15. Ozensoy, E., Meier, D.C., and Goodman, D.W., *J. Phys. Chem. B*, 2002. **106**(36): p. 9367.
16. Hertz, H., *Ann. Physik*, 1887. **31**: p. 983.
17. Roentgen, W.C., *Sitzber. Physik. Med. Ges.*, 1895. **137**: p. 1.
18. Innes, P.D., *Proc. Roy. Soc. Lon. Ser. A*, 1907. **79**: p. 442.
19. Siegbahn, K., Nordling, C., Fahlman, A., Hamrin, K., Hedman, J., Ndberg, R., Jahansson, C., Bergmark, T., Karlsson, S.E., Lindgren, I., and Lindberg, B., *Nova Acta Regiae Soc. Sci. Ups.*, 1967. **20**: p. 1.
20. Schwartz, M.E., *Chem. Phys. Lett.*, 1970. **6**(6): p. 631.
21. Jolly, W.J., *J. Amer. Chem. Soc.*, 1970. **92**(11): p. 3260.

22. Rossi, A. and Elsener, B., *Mat. Sci. Forum*, 1995. **185-188**: p. 337.
23. Arranz, A. and Palacio, C., *Surf. Sci.*, 1996. **355**(1-3): p. 203.
24. Doron-Mor, H., Hatzor, A., Vaskevich, A., van der Boom-Moav, T., Shanzer, A., Rubinstein, I., and Cohen, H., *Nature*, 2000. **406**(6794): p. 382.
25. McDanels, S.J., *Strain*, 2006. **42**: p. 159.
26. Spicer, W.E. and Berglund, C.N., *Phys. Rev. Lett.*, 1964. **12**(1): p. 9.
27. Turner, D.W. and Al-Joboury, M.I., *J. Chem. Phys.*, 1963. **37**: p. 3007.
28. Eastman, D.E. and Cashion, J.K., *Phys. Rev. Lett.*, 1971. **27**(22): p. 1520.
29. Eastman, D.E., *Solid State Comm.*, 1972. **10**(10): p. 933.
30. Baker, J.M. and Eastman, D.E., 1973. **10**(1): p. 223.
31. Atkinson, S.J., Brundle, C.R., and Roberts, M.W., *Chem. Phys. Lett.*, 1974. **24**(2): p. 175.
32. Demuth, J.E. and Eastman, D.E., *Phys. Rev. Lett.*, 1974. **32**(20): p. 1123.
33. Hofmann, P., Bare, S.R., Richardson, N.V., and King, D.A., *Solid State Commun.*, 1982. **42**(9): p. 645.
34. Ogletree, D.F., Bluhm, H., Lebedev, G., Fadley, C.S., Hussain, Z., and Salmeron, M., *Rev. Sci. Instrum.*, 2002. **73**(11): p. 3872.
35. Pantforder, J., Pollmann, S., Zhu, J.F., Borgmann, D., Denecke, R., and Steinruck, H.P., *Rev. Sci. Instr.*, 2005. **76**(1).
36. Stoltze, P. and Norskov, J.K., *Phys. Rev. Lett.*, 1985. **55**: p. 2502.
37. *Phys. Chem. Chem. Phys.*, 2007. **9**(27).
38. Cremer, P.S., Stanners, C., Niemantsverdriet, J.W., Shen, Y.R., and Somorjai, G.A., *Surf. Sci.*, 1995. **328**: p. 111.
39. Cremer, P.S., McIntyre, B.J., Salmeron, M., Shen, Y.R., and Somorjai, G.A., *Catal. Lett.*, 1995. **34**: p. 11.
40. Cremer, P.S., Su, X.C., Shen, Y.R., and Somorjai, G.A., *J. Chem. Soc. Faraday Trans.*, 1996. **92**: p. 4717.
41. Bratlie, K.M., Kliewer, C.J., and Somorjai, G.A., *J. Phys. Chem. B*, 2006. **110**(36): p. 17925.
42. Bratlie, K.M., Montano, M.O., Flores, L.D., Paajanen, M., and Somorjai, G.A., *J. Am. Chem. Soc.*, 2006. **128**(39): p. 12810.
43. Montano, M., Bratlie, K.M., Salmeron, M., and Somorjai, G.A., *J. Am. Chem. Soc.*, 2006. **128**(40): p. 13229.

44. McIntyre, B.J., Salmeron, M., and Somorjai, G.A., *J. Vac. Sci. Technol. A*, 1993. **11**: p. 1964.
45. Jensen, J.A., Rider, K.B., Chen, Y., Salmeron, M., and Somorjai, G.A., *J. Vac. Sci. Technol. B*, 1999. **17**: p. 1080.
46. Rider, K.B., Hwang, K.S., Salmeron, M., and Somorjai, G.A., *J. Am. Chem. Soc.*, 2002. **124**: p. 5588.
47. Rider, K.B., Hwang, K.S., Salmeron, M., and Somorjai, G.A., *Phys. Rev. Lett.*, 2001. **86**: p. 4330.
48. Hayden, B.E., Lackey, D., and Schott, J., *Surf. Sci.*, 1990. **239**: p. 119.
49. Osterlund, L., Rasmussen, P.B., Thostrup, P., Laegsgaard, E., Stensgaard, I., and Besenbacher, F., *Phys. Rev. Lett.*, 2001. **86**: p. 460.
50. Ozensoy, E., Hess, C., Loffreda, D., Sautet, P., and Goodman, D.W., *J. Phys. Chem. B*, 2005. **109**: p. 5414.
51. Conrad, H., Ertl, G., Kuppers, J., and Latter, E.E., *Surf. Sci.*, 1977. **65**: p. 235.
52. Vang, R.T., Wang, J.G., Knudsen, J., Pedersen, T.M., An, T., Laegsgaard, E., Stensgaard, I., and Besenbacher, F., *J. Phys. Chem. B*, 2005. **109**: p. 14262.
53. Besenbacher, F., Chorkendorff, I., Clausen, B.S., Hammer, B., Molenbrock, A.M., Norskov, J.K., and Stensgaard, I., *Science*, 1998. **279**: p. 1913.
54. Vestergaard, E.K., Vang, R.T., Knudsen, J., Pedersen, T.M., An, T., Laegsgaard, E., Stensgaard, I., Hammer, B., and Besenbacher, F., *Phys. Rev. Lett.*, 2005. **95**: p. 126191.

Chapter Two – Experimental Methods

2.1 Ultra High Vacuum (UHV) Techniques

Ultra High Vacuum is the term used to describe the experimental pressure region below 10^{-7} mbar [1] although UHV experiments are generally performed around 10^{-9} mbar. In order to obtain these low pressures the chambers are constructed from argon-welded stainless steel, which are continuously pumped, typically by diffusion and/or turbo pumps backed by a rotary pump. Inside the chamber there is a mu-metal lining which provides magnetic shielding for low energy electron techniques. The chamber used in the research presented in this thesis was designed so that it can be heated to approximately 120 °C by several ceramic bakeout heaters. This is a little lower than standard UHV chambers which can be heated to 180 °C, due to the CsI windows attached to the chamber. This process, known as baking, accelerates the desorption of water vapour and other gases from the chamber walls, which can then be pumped away. As the system cools down, a cold trap inside the chamber is filled with liquid N_2, this causes many contaminants in the chamber to condense from the gas phase onto the cold metal surface. Generally pressures will drop from 10^{-8} mbar down to 10^{-10} following the bake and filling of the cold trap.

2.1.1 Dosing Set-up

Gases to be introduced into the chamber were attached to a single gas line on the chamber, and dosed through a leak valve. Gas samples were opened to a small section of gas line using Nupro valves to hold the pressure, this gas was expanded up to the leak valve. The gases were dosed by back filling the chamber. Gases used in High Pressure Reaction Cell used a different gas line set-up which is described in section 4.3.

2.1.2 Sample Cleaning

Cleaning of the Cu(100) crystal was achieved using ion bombardment, followed by annealing. Cycles of sputtering with argon, 3 x 10^{-5} mbar for 30 min, with a beam energy of 0.5 keV, were followed by heating the crystal to approximately 650 K and allowing it to cool to approximately 350 K.

2.1.3 Ion Bombardment

The most common contaminants of metal single crystals are oxygen, carbon and sulphur. The most effective method of cleaning crystals in surface science is ion bombardment of the sample with noble gas ions e.g. Ne^+ or Ar^+. Ion bombardment is performed by backfilling the chamber with a noble gas and using an ion gun to produce a beam of noble gas ions. The ion gun operates by heating a filament which in turn produces electrons, these electrons collide with the noble gas atoms to produce positively charged ions. These noble gas ions are then accelerated towards the sample via the application of a large potential. After bombardment an annealing cycle is used to reorder the surface due to the disturbance of the surface atoms. Another effect of the annealing is to draw contaminants out of the bulk to the surface, as such an atomically clean crystal is obtained by cycles of both ion bombardment and annealing [2].

2.1.4 Photoelectron Spectroscopy (PES)

PES can provide very important information regarding the elemental surface composition of the single crystal surface [3]. The technique requires vacuum conditions due to the otherwise short mean free path of electrons. Once under vacuum the sample is irradiated with photons; for X-ray photoelectron spectroscopy (XPS), an X-ray source, typically with an Al or Mg anode is used; for ultraviolet photoelectron spectroscopy (UPS), a UV source utilising He(I/II) discharge lamp is often used [4]. Upon irradiation the surface atoms emit photoelectrons, in XPS these are core level electrons, in UPS they are valence shell electrons which have received a direct transfer of energy from photons of greater energy than the work function of the solid. These emitted electrons are then separated, according to energy, and counted using a concentric hemispherical analyser. The photoemission effect, illustrated in figure 2.1, means that the energy of the emitted photoelectrons is directly related to both the atomic and molecular environment from which they originate. The number of photoelectrons emitted is correlated to the concentration of emitting atoms in the sample [5].

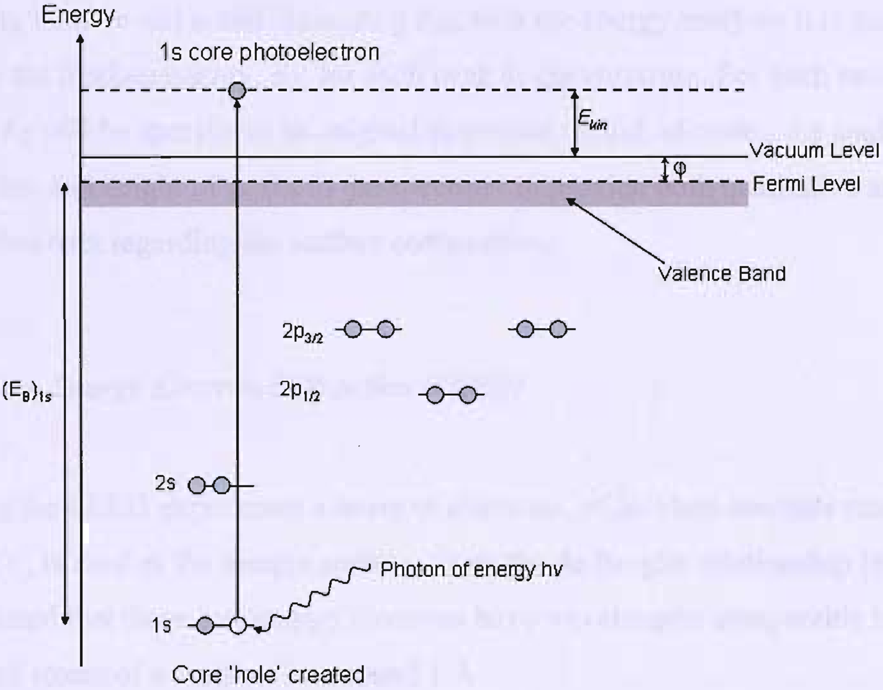

Figure 2.1 – X-ray photoemission of a 1s core electron

Applying the principle of conservation of energy, the kinetic energy of the photoelectrons, E_{kin}, is equal to:

$$E_{kin} = h\nu - E_B - \varphi \qquad \textbf{2.1}$$

where:
$h\nu$ is the energy of the incident photons
E_B is the binding energy of the ejected electron
φ is the work function of the surface

The binding energy is defined as the energy difference between the core level of the emitted electron and the Fermi level. The work function is defined as the minimum energy required to remove an electron situated in the highest occupied energy level in the solid to the vacuum level. However, this equation is the simplest approximation of the photoemission process, the frozen-orbital approximation. As such it fails to take into account that upon photoemission, the surface species will have a $+e$ charge which then presents a different potential to both the outgoing photoelectron and the surrounding electrons [4].

Knowing both hv and φ and measuring E_{kin} with the energy analyser it is possible to calculate the binding energy, E_B, for each peak in the spectrum. For each emitted electron E_B will be specific to its original elemental orbital, allowing the analysis of the position and height of peaks in the spectrum to provide both qualitative and quantitative data regarding the surface composition.

2.1.5 Low Energy Electron Diffraction (LEED)

During the LEED experiment a beam of electrons, of incident energies ranging from 30-300 eV, is fired at the sample surface. From the de Broglie relationship [6], it can be calculated that these low energy electrons have wavelengths comparable to the spacing of atoms of a surface, i.e. around 1 Å.

$$\lambda = \frac{h}{mv} = \sqrt{\frac{1.504 \times 10^{-18} eV\, m^2}{E}} = \sqrt{\frac{150.4\, eV\, \text{Å}^2}{E}} \qquad \textbf{2.2}$$

where:
λ is the electron wavelength in Å
m is the mass of an electron
v is the velocity
h is Planck's constant
E is the energy of the electron in eV

Since the electron wavelengths are of a similar magnitude to the spacing between atoms of a crystal surface, the electrons are diffracted (elastically backscattered) from the surface onto the detector. The diffraction patterns visible on the detector are due to constructive interference from the elastically scattered electrons (figures 2.2 and 2.3) according to the Bragg equation (eqn. 2.3).

$$n\lambda = a\sin\theta \tag{2.3}$$

where: n is the order of diffraction, an integer
λ is the electronic wavelength, in Å
a is the interatomic distance, in Å
θ is the angle from incident

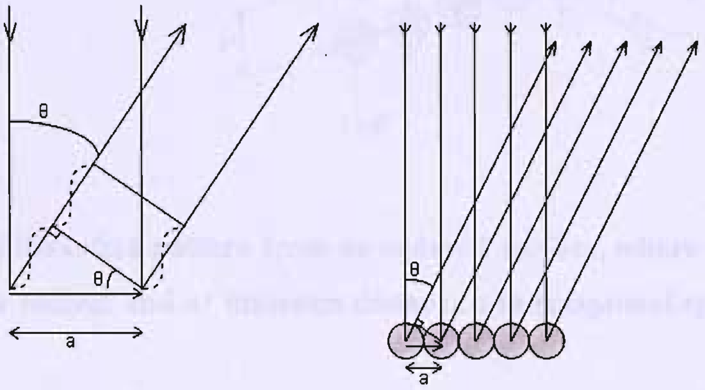

Figure 2.2 – Constructive interference of diffracted electrons from a one dimensional periodic array

Following this theory into a two dimensional array, such as an ordered surface, would produce an equivalent two dimensional diffraction pattern on the screen as shown in figure 2.3. Therefore if the diffraction occurs due to an ordered surface then by studying the diffraction pattern it is possible to gain information about the structure of the surface. For example, the symmetry of the surface is always the same as the symmetry of the diffraction pattern. The diffraction pattern is given in reciprocal space, this means that longer distances on the surface will give rise to shorter distances on the diffraction pattern, which enables the orientation of rectangular lattices to be assigned.

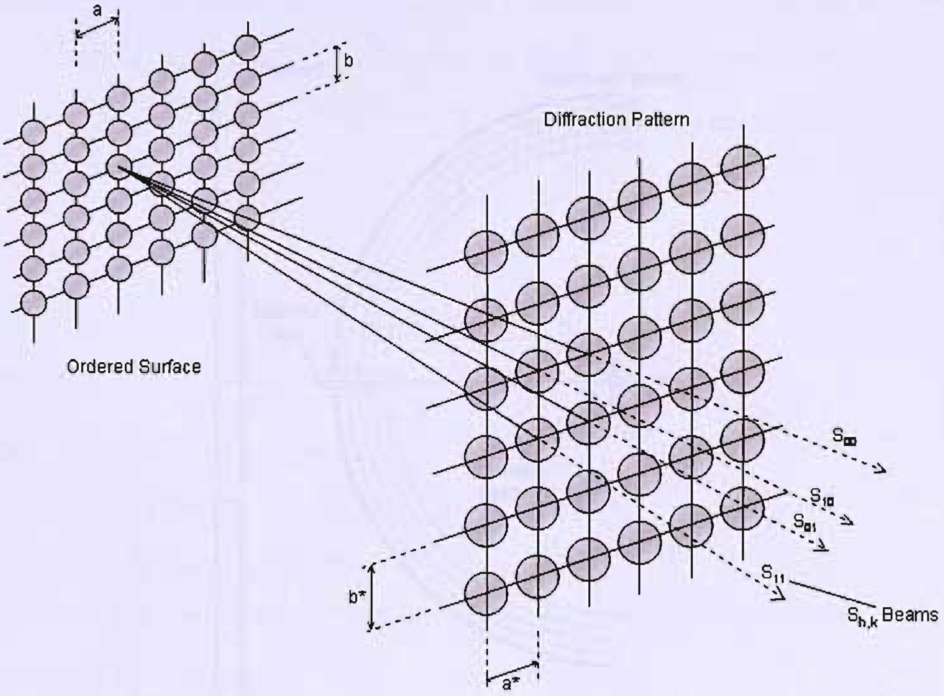

Figure 2.3 – Diffraction pattern from an ordered surface, where h and k are Miller indices and a* indicates distance a in reciprocal space

The setup of the LEED optics, a retarding field analyser (RFA) is shown in figure 2.4, it contains a system of grids (G1-4) used to minimise the diffuse background resulting from inelastically scattered electrons which make up 99 % of the scattered electrons. The outer grid (G4) nearest to the sample is earthed, this provides a field-free region for the electrons to move within. The innermost grid (G1) is also held at earth in order to shield the electrons from any high voltages placed on the phosphor screen. This field-free region ensures that the electrons scattered from the surface travel in a straight line. The final pair of grids (G2 and G3) serve as a cut-off filter and are held at variable negative potentials to retard the inelastically scattered electrons which have a lower energy than the diffracted electrons. The elastically scattered, diffracted, electrons are accelerated towards the fluorescent screen, which is held at approximately +6 keV. This ensures that the electrons have enough kinetic energy to cause light emissions when they hit the coated fluorescent glass screen. The diffracted electrons give rise to a pattern consisting of bright spots on a dark background, which as mentioned earlier, reflects the symmetry and crystalline order of the surface. The image can then be recorded through the view port using a digital camera.

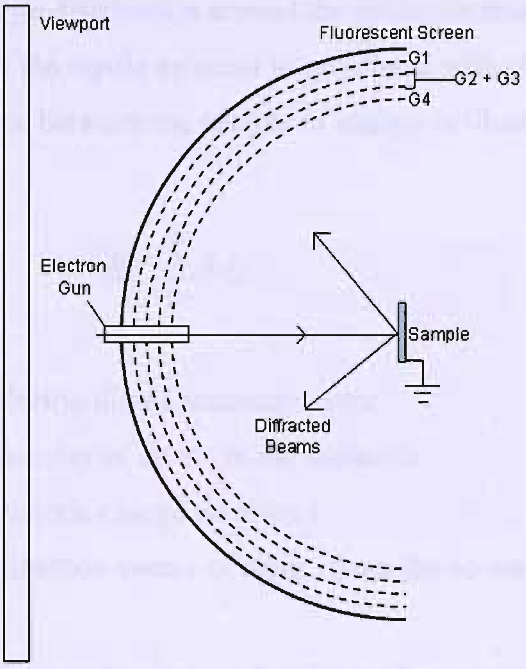

Figure 2.4 – Typical LEED Optics [7]

If molecules or atoms adsorb on the surface, they will often form ordered structures on top of the surface, this ordered layer will give rise to diffraction and an additional set of spots will be visible on the LEED screen.

2.2 *Reflection Absorption Infrared Spectroscopy (RAIRS)*

RAIRS is an optical technique used in surface analysis, this technique provides useful information about the structure and bonding of adsorbed species by the absorption of infrared radiation [8, 9]. The technique is non-destructive and can be used in a non-vacuum environment.

2.2.1 Theory of RAIRS

In order for an adsorbed species to be detectable in the infrared the molecule must have a fluctuating electric dipole moment associated with the vibrational movement.

This is the conventional infrared selection rule known from transmission spectroscopy. This rule means the charge distribution around the molecule must not be symmetrical, a dipole. The strength of the dipole moment is associated with charge difference on the molecule and the distance between the centres of charge as illustrated in equation 2.4.

$$\underline{\mu} = \sum_{i=1}^{N} q_i \underline{r_i} \qquad \textbf{2.4}$$

where: $\underline{\mu}$ is the electric dipole moment vector

N is the number of atoms in the molecule

q_i is the electric charge on atom i

r_i is the direction vector of atom i from the centre of mass of molecule

Whilst the molecule bends and stretches, the dipole changes, setting up an electric field around the molecule. An interaction occurs if the alternating electric field of the infrared radiation matches, in frequency, one of the natural oscillatory frequencies of the molecule. This interaction results in a resonant energy transfer and a change in the amplitude of the motion, it is this change which can be monitored for information about the strength of the excited bonds.

There is a second factor which needs to be taken into consideration with the experiment, the interactions between the surface and the adsorbate as well as with the infrared radiation. The electric field of the infrared radiation will also interact with valence electrons in the metal surface, which results in the excitation of both the electric dipole of the molecule and its image in the surface [10]. This means the vector sum of the fields of the electric dipole and its image is of great importance. If the dipole of the molecule is perpendicular to the surface the field will be enhanced by the incident electric field associated with the infrared radiation. However, a dipole which sits parallel to the surface will result in a quadrupole, this leaves no overall dipole moment to interact with the electric field as it is effectively shielded by the surface as presented in figure 2.5.

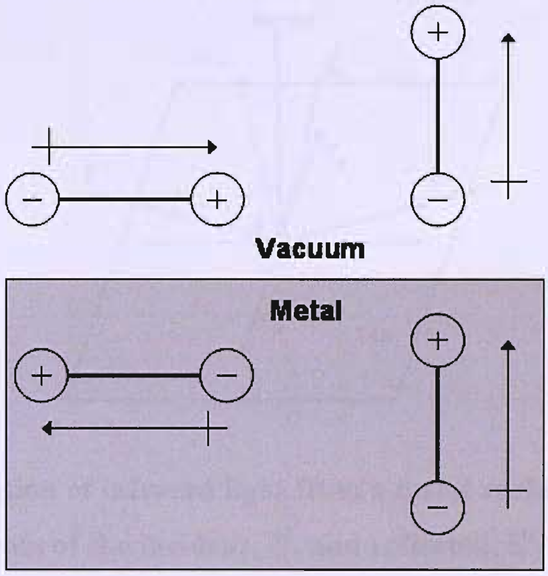

Figure 2.5 - The screening and enhancements of a metal surface with respect to parallel and perpendicular dipoles

2.2.2 Interaction between Infrared Radiation and the Surface

Using the Fresnel equations (2.5 - 2.7) [11] it is possible to describe the interaction of infrared radiation with a clean metal surface. This interaction causes a change in the intensity, R, and a shift in the phase, δ, of the reflected light, which are dependent on the orientation of the electric field vectors of the radiation.

There are two components of light, designated s- and p-, which are associated with the direction of polarisation, s-polarised light has its electric field vector perpendicular to the plane of incidence and the p-polarised light has an electric field vector parallel to the plane of incidence. Figure 2.6 illustrates that the electric field vectors of the infrared radiation can be reduced to their individual parallel and perpendicular components when deriving the Fresnel equations [12].

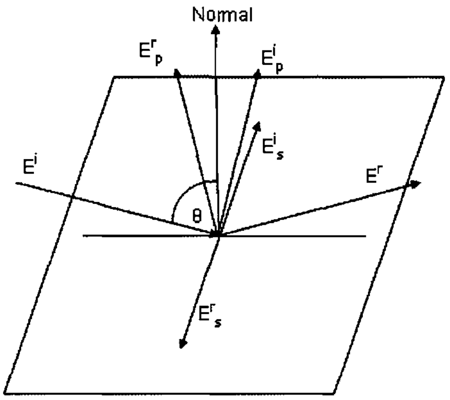

Figure 2.6 – Reflection of infrared light from a metal surface. Showing s and p components of the incident, E^i, and reflected, E^r, radiation.

The Fresnel equations (2.5 – 2.7) which describe the interaction between infrared light and the surface are shown below.

$$R_p = \frac{(n - \sec\theta)^2 + k^2}{(n + \sec\theta)^2 + k^2} \tag{2.5}$$

$$R_s = \frac{(n - \cos\theta)^2 + k^2}{(n + \cos\theta)^2 + k^2} \tag{2.6}$$

$$\tan\Delta = \tan(\sigma_p - \sigma_s) = \frac{(2k\tan\theta\sin\theta)}{\tan^2\theta - (n^2 + k^2)} \tag{2.7}$$

where: R_p / R_s are the reflected intensities for p- and s- polarised light

σ_p / σ_s are the phase shifts felt by p- and s- polarised light on reflection

θ is the angle of incidence

n is the refractive index of the metal

k is the absorption constant of the metal

Both the reflected intensities and the phase shifts for p- and s- polarised light can be calculated as a function of the angle of incidence, the plots of which are shown in figure 2.7.

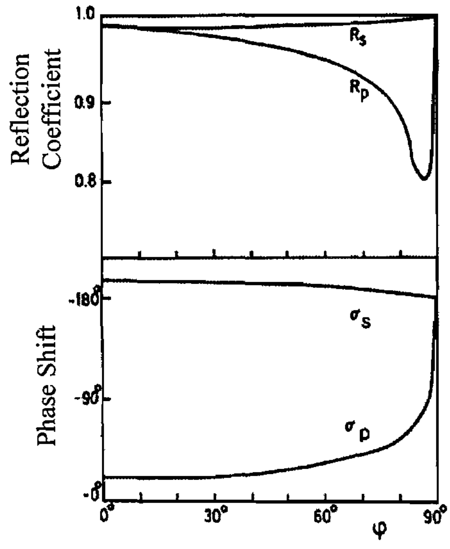

Figure 2.7 – Reflection coefficients, *R*, and phase shifts, *σ*, of the s and p components of the IR radiation from a metal surface as a function of angle of incidence (from normal), *φ* [13]

The resultant field at the surface is a combination of the amplitude of the incident electric field, $E^i \sin\theta$, and the field due to the reflected wave, E^i r sin $(\theta + \sigma)$, and can be represented by equations 2.8 and 2.9 for p- and s- polarised light.

$$E_p = E_p^i\left[\sin\theta + r_p \sin\left(\theta + \sigma_p\right)\right] \qquad \textbf{2.8}$$

$$E_s = E_s^i\left[\sin\theta + r_s \sin\left(\theta + \sigma_s\right)\right] \qquad \textbf{2.9}$$

where: E^i is the incident electric field
E is the resultant electric field
θ is an arbitary phase
r is the reflection coefficient
σ is the phase shift

In the case of s-polarised light the phase shift is very close to 180° and from figure 2.7 the reflection coefficient can be shown to be close to one for all angles of incidence. If these values are placed in equation 2.8 it is possible to see that the phase shift is destructive and results in no electric field at the surface, therefore no interaction can occur with any vibrational dipoles present. P-polarised light on the other hand has components both parallel, $E_p^{//}$, and perpendicular, $Ep^{\perp}$, to the surface. From figure 2.7 it can be seen that as the angle of incidence changes both the phase shift and the reflection coefficient both change to a far greater extent when considering p-polarised in comparison to s-polarised light.

In order to optimise the constructive interference between the incident and reflected waves the phase shift needs to be 90°, from figure 2.7 it can be seen that this correlates to an angle of incidence of approximately 88°.

2.2.3 *The Adsorbate Layer*

The adsorbate layer can be modelled as a three-phase system originally presented by Greenler [13] and shown in figure 2.8. It consists of a homogeneous isotropic layer placed on a surface, which is characterised by an estimate of the dielectric constant for the adsorbate layer in the calculations. These calculations were further simplified by McIntyre and Aspnes [10].

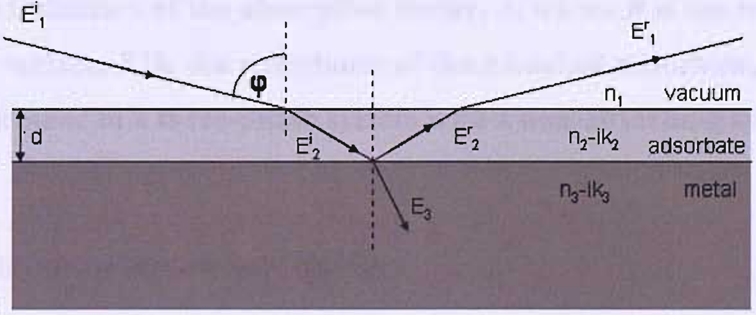

Figure 2.8 – The three-phase model, showing the various optical properties needed to calculate the optimum angle of incidence for a specific system under study [13]

Typically for a single crystal in UHV, with a monolayer of adsorbate, the optimum angle of incidence, φ, is found to be 88° [13, 14]. An additional benefit of this grazing incidence is that the surface area exposed to the incident radiation will be greatly increased.

During the RAIRS experiment information is obtained by looking at the loss in intensity of the reflected radiation, in the presence of the adsorbed layer. This loss can correspond to the vibrational modes of either the adsorbed species or the interaction of the adsorbed species with the surface atoms of the substrate. The absorption factor is a convenient way to measure the depth of an infrared absorption band obtained from the reflection sampling system, and is shown in figure 2.9 (developed from reference 6.)

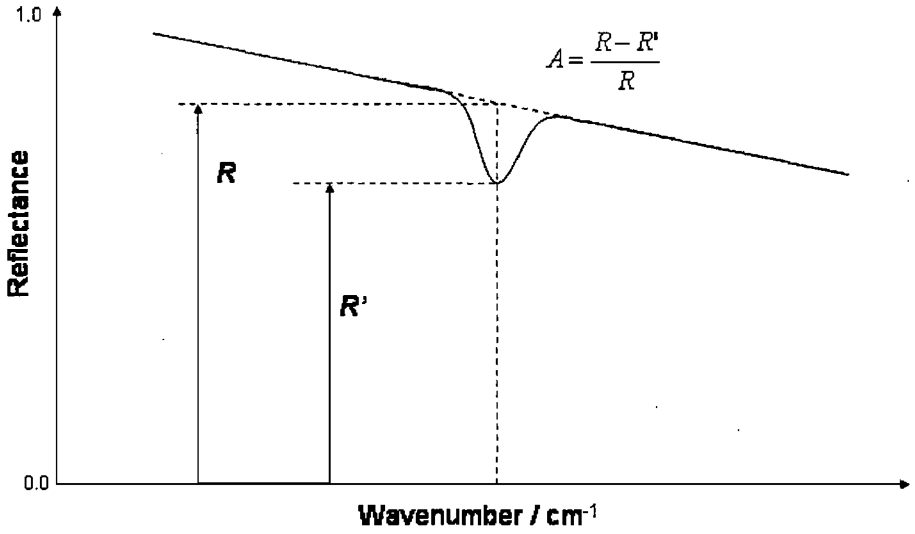

Figure 2.9 – Definition of the absorption factor, *A*, where *R* is the reflectance of the original surface, *R'* is the reflectance of the modelled adsorbate, and *R-R'* is the reflectance in a three-phase system with a non-adsorbing adsorbate

2.2.4 Bonding Site Allocation with RAIRS

When a simple linear molecule is adsorbed in an on-top position the symmetry of the molecule is $C_{\infty v}$ and four possible vibrations exist. Two A_1 modes are present, the C-O stretch, the M-CO stretch (frustrated translation) and two E modes related to the frustration of the rotation of the CO molecule and of a linear translation parallel to the surface. Of these only the A modes are IR active due to the dipole selection rule.

When the CO molecule is bonded in a bridge position the degeneracy of the two E modes is removed. The symmetry drops to C_{2v} and additional rotation and parallel translation frustrated modes are added. Although the frustrated modes are still not IR active, the two A modes will have shifted to lower frequencies.

If the symmetry of the adsorbed molecule is lowered yet further to C_s, i.e. the CO molecule is adsorbed in an asymmetric bridge site, then two additional IR peaks may be detected for the frustrated rotation and translation modes [15].

2.2.5 Vibrational Shifts Due to Coverage

It has been shown in the literature that as the coverage of adsorbate increases the frequency of the stretching vibration steadily shifts upwards as seen with CO adsorbed on Pd(100) at 100 K [16]. These shifts are attributable to intermolecular interactions which can be placed in three categories – vibrational coupling, chemical interactions and intermolecular repulsions.

2.2.5.1 Vibrational Coupling

There are two ways in which dipole-dipole coupling can happen in an adsorbate layer, it can occur either through space [17] or through the metal electrons in the surface [18].

Some of the reason the vibrational frequency of a molecule changes when it is adsorbed to a surface is because the dipole of the molecule interacts with an equivalent dipole image in the metal surface. It makes sense then to consider the dipole of a molecule may also interact with both the dipole of other adsorbed molecules and their related images. An equation has been proposed by Pfnür *et al.* [19] which approximates the frequency shift as a function of coverage, essentially the equation shows that the frequency is shifted to lower frequencies by its own image but to higher frequencies upon interaction with other dipoles and images. Developments were made by removing the self image from the lattice calculation involved in the equation, instead including it in the molecular polarisability. This change enabled Persson and Ryberg to provide consistent theoretical and experimental results for CO adsorbed on Cu and Pd [20].

Through metal electron interactions can be considered similar in their effects, from a mathematical stand point, as through space coupling. However in a physical sense they are quite different. When using molecular orbitals to describe a molecule adsorbed on a surface, two oscillators are incorporated when a neighbouring molecule is considered. Therefore when the strength of one bond is altered there will be a direct influence on the other bond.

Experimentally these two vibrational coupling effects shift the frequency to higher values and it is not possible to distinguish between the two.

2.2.5.2 Electrostatic and Chemical Effects

These effects are assigned to the presence of back-donation from the metal to the CO molecule. When a CO molecule adsorbs to a surface a chemical bond is formed by charge transfer from the 5σ orbitals of CO into the metal and with back-donation from the metal into the unoccupied $2\pi^*$ molecular orbitals of CO. Whilst the 5σ orbitals are weakly bonding, the $2\pi^*$ MOs are strongly anti-bonding, as such the C-O bond is weakened by adsorption to a surface leading to a lowering of the stretching frequencies.

As coverage increases it has been shown that the frequency increases in opposition to this effect. Blyholder [21, 22] has proposed that this is due to increased competition for the electrons from the metal surface which are back-donated into the $2\pi^*$ orbitals of the CO molecules. If this is the case the level of back-donation per CO molecule will fall, consequently the strength of the C-O bond will rise along with the stretching frequency.

Unlike vibrational coupling effects it is possible to distinguish chemical frequency shifts experimentally. It has been shown theoretically that only molecules with the same vibrational frequency couple strongly, it was proposed that using an isotopic mixture these effects may be removed [17]. A few years later this was proved experimentally, King *et al.* [23, 24] gradually diluted a ^{13}CO layer in ^{12}CO on Pt(111) and showed how much of the shift was due to dipole coupling. Once the ^{13}CO molecules reached its dilution limit it was no longer affected by any other ^{13}CO

molecules. However, it would still be chemically affected by the presence of ^{12}CO, therefore any frequency shift still present could be attributed to a chemical affect.

A further example of the use of isotopic substitution can be found when considering CO on Cu(111). Hollins and Pritchard showed that the presence of a small shift (approximately 8 cm^{-1}) from low coverage to high coverage was actually due to two competing effects [25, 26]. A vibrational coupling effect to higher frequency and an unusual chemical shift to lower frequency, this chemical shift differs from what is observed on transition metal surfaces and has been attributed by the authors to a gradual alteration in the σ- and π-bonding compostition [25].

2.2.5.3 Intermolecular Forces

Forces between adsorbed molecules will increase as the coverage increases, these forces have also been related to an increase in the C-O stretching frequency [27]. As the intermolecular distances get shorter the overlap of the wave functions increases, this results in a reduction in the occupation of the $2\pi^*$ MOs, which as mentioned before strengthens the C-O bond. Ortega *et al.* [28] have released experimental observations to confirm this theory, working with CO on Pd(100). Observing the M-CO bond the stretching frequency remains constant until coverage reaches ½ monolayer, at this point the frequency drops indicating a weakening of the M-CO bond. This coincides with a compression of the CO layer and would suggest it is related to the rise in intermolecular repulsion associated with the compression.

2.3 Spectrometers for RAIRS

2.3.1 Dispersive Instruments

The majority of early RAIRS experiments were performed using dispersive spectrometers or monochromators. The radiation of a source is monochromatised via the use of diffraction gratings, the maximum energy from which is termed the 'blaze wavelength'. This wavelength is determined by an angle related to the grating and the grooves present on the grating. Either side of this angle and the energy efficiency decreases, therefore if broad spectral ranges are desired then more than one monochromator is required. Diffraction gratings can also be affected by radiation from higher diffraction orders, these can be removed by using 'cut-off' filters. Over a large spectral range, for example 4000 – 650 cm^{-1} three different gratings and filters would be required [15]. In this thesis interferometry is preferred to dispersive instrumentation.

2.3.2 Fourier Transform Infrared (FT-IR) Spectroscopy

The theory of FT-IR is based on interferometry, and the use of Fourier transformation to obtain spectral information from the interferogram, this technique has been discussed by many authors [29, 30].

The use of FT in infrared spectroscopy originates from the development of the integral part of the spectrometer, the Michelson interferometer [31], shown in figure 2.10. Rayleigh then realised the interferogram required the use of the Fourier transform in order to interpret the output usefully [32].

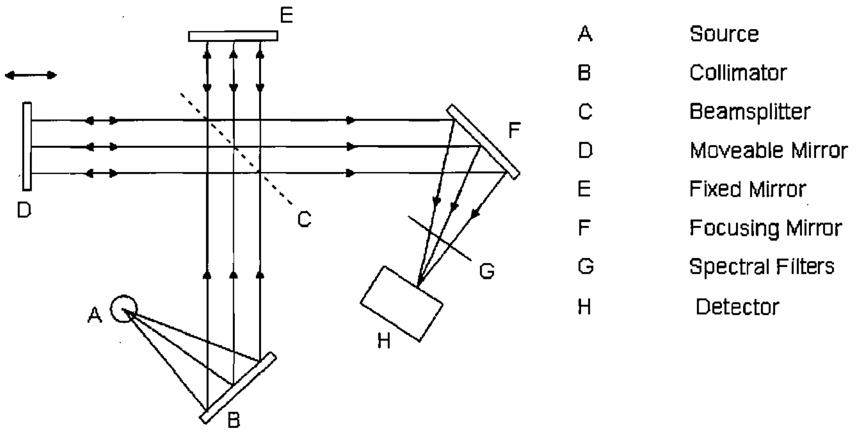

Figure 2.10 – The Michelson interferometer optical system adapted from reference 15

The interferometer works by collecting light from an infrared source (A) and directing it to a beamsplitter (C). Here the radiation is split in half, one half passes to a moving mirror (D), whilst the second half is transmitted to a fixed mirror (E). The two mirrors sit perpendicular to each other, upon reflection the beams recombine to create an interferogram, which is due to the difference in the path length of the light introduced by the moving mirror. A Fourier transform of the signal reaching the detector (H) is performed, when plotted against wavenumber a graph of intensity vs. wavenumber is produced, see figure 2.11, it is the ratio of these intensity graphs which produce the infrared spectrum.

There are three main advantages of the FT system over dispersive instruments. The main one of these is the multiplex (Fellgett) advantage, where all light from a source can be detected at any instant. Every point on the interferogram contains information from each wavelength present in the input light signal, whereas, for a dispersive instrument, only one wavelength is detected at any given time. The Fellgett advantage also relates to the throughput of the signal; for measurements taken at equal resolution, over the same spectral range and with the same collection time, the signal-to-noise ratio, $S{:}N$, of the spectrometer will be $\sqrt{n}$ times greater than the $S{:}N$ of spectra measured using a dispersive instrument, where n is the number of resolution elements. In simpler terms this means that measurements made at the same $S{:}N$ can be made n times faster using an FT spectrometer [33]. This benefit is largely diminished if experiments are only concerned with a single narrow vibrational band, as the rest of the spectral range would contain no information.

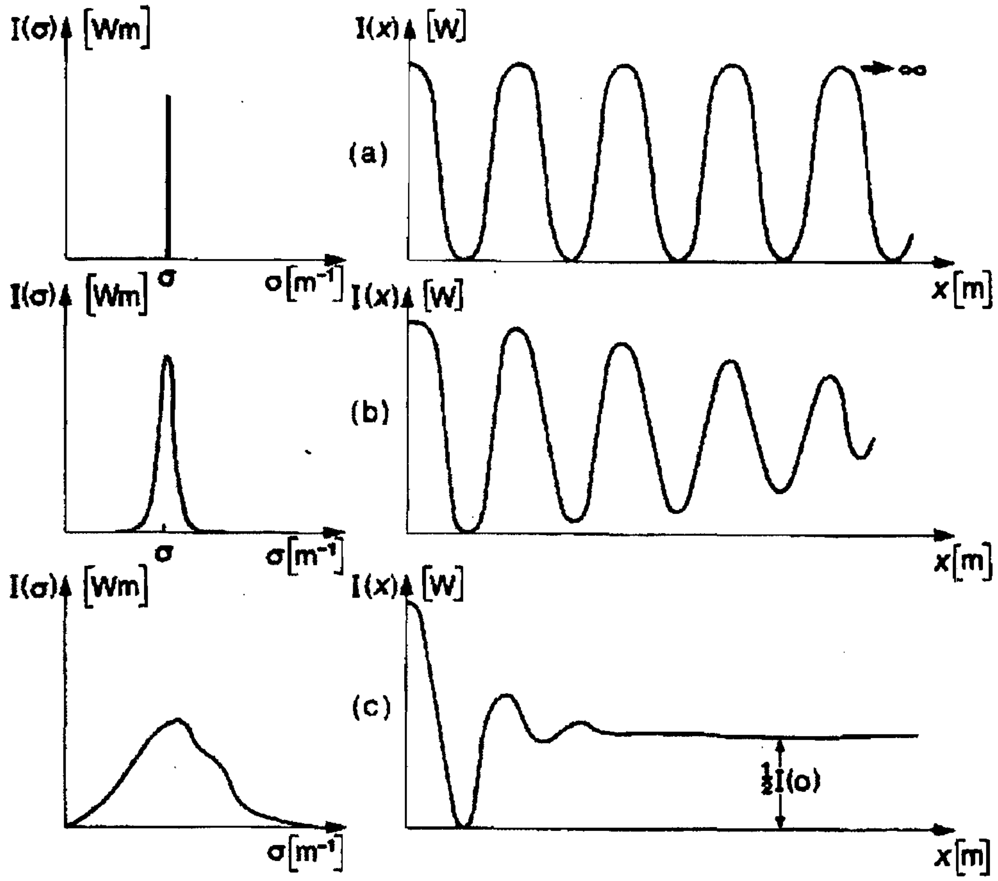

Figure 2.11 – Relation between the detected spectrum *I(φ)* and the interferogram signal *I(x)* produced by it: (a) monochromatic spectrum; (b) quasi-monochromatic spectrum; (c) broad-band spectrum [30]

The second advantage is the Jacquinot, or throughput advantage, this arises due to the simplicity of the optical path of the spectrometer. In an FT instrument there are fewer optical elements and no gratings in comparison to the dispersive spectrometer. In particular, there are no entrance and exit slits which reduce intensity; in general for a conventional dispersive spectrometer the narrower the slits are, the better the resolution, however, this comes at the expense of the throughput. The use of an FT interferometer allows more energy through to the spectrometer and it follows that there would therefore be more signal at the detector. At a specific resolution more flux can pass through an interferometer than a monochromater, this leads to a greater spectral resolution without decreasing the light throughput. This is quite important in conventional bulk sample spectroscopy, however in surface infrared spectroscopy it is more likely that the small image size and solid angle at the sample is the throughput limiting feature of the experiment [34].

The final advantage is the Connes advantage, which is associated with frequency precision. In an FT-IR system a monochromatic light source, generally a He:Ne laser, is used as an internal frequency standard. This source is used to monitor mirror movement and the detector sampling of the signal, it is also used to calculate all the frequencies in the output spectrum. This technique enables the FT-IR to achieve frequency precision and accuracy of around 0.01 cm^{-1}.

The main disadvantage of the FT-IR system is that a background scan separate to the sample scan needs to be obtained, requiring all experimental conditions to remain constant between the two.

There are three main types of noise [35] which can affect recorded data, the first of these is termed Johnson noise. This type of noise arises from the thermally agitated motion of electrons in circuits and is generally reduced by cooling the experimental apparatus. The quantity of Johnson noise recorded is not related to the spectrum therefore as the signal increases the level of this type of noise remains constant. This means the effect of Johnson noise is greatly reduced by Fourier transform spectrometric measurements.

The second type of noise arises from the quantized nature of electrical measurement and is called shot noise. Due to the random emittance of photons from typical sources there will be fluctuations in intensity on a microscopic level, these fluctuations scale with the square root of the intensity of the beam. This type of noise can cancel the multiplex advantage for Fourier transform spectrometers.

The final type is called flicker noise, which is related to the slow drift of electrical components caused by temperature fluctuations etc. The intensity of this noise increases directly with signal.

The relative arguments for and against dispersive and interferometric instruments for RAIRS are covered in more detail by Bradshaw and Schweizer [36].

2.4 Sources for RAIRS

Three types of sources have traditionally been used for surface infrared spectroscopy; thermal emitters, tunable lasers and synchrotron sources. Thermal emitters are discussed briefly here, whilst synchrotron radiation, with specific focus upon the Daresbury SRS, is discussed in more detail in section 2.6.1. Discussions regarding laser sources are available in the literature [37].

2.4.1 Thermal emitters

Thermal emitters are also referred to as black-body sources, from the Stefan-Boltzmann law it is possible to see that the power emitted from a source into an area, *A*, is proportional to the temperature, *T*, of the source.

$$P \approx A\sigma T \qquad \textbf{2.10}$$

where: σ is 5.667 x 10^{-8} W m^{-2} K^{-4} [15]

For spectroscopy only a certain range of wavelengths is of interest, for example λ to dλ, therefore the spectral distribution is of interest and can be calculated using Planck's radiation law.

$$P_\lambda = \frac{c_1}{\lambda^5} A \frac{d\lambda}{\exp(c_2/\lambda T) - 1} \qquad \textbf{2.11}$$

where: $c_1 = 2\pi h c^2 = 3.74 \times 10^{-16}\ W\ m^2$

$c_2 = hc/k = 1.44 \times 10^{-2}\ m K$ [15]

Two conclusions may be drawn from this equation that the power output increases with temperature but that as the wavelength increases (decreasing wavenumbers) the spectral distribution falls off sharply. This second conclusion makes blackbody sources difficult to use for far-IR work and experiments require sensitive detectors due to the low power output.

2.4.2 Synchrotron Radiation

If a charged particle, e.g. an electron, is accelerated it emits electromagnetic radiation. At non-relativistic velocities a cosine distribution is observed and the radiation has a characteristic frequency, figure 2.12, Case I. However, if the velocity of the particle approaches the speed of light, relativistic effects alter the distribution so that it peaks sharply in the direction of the movement of the charged particles, figure 2.12, Case II.

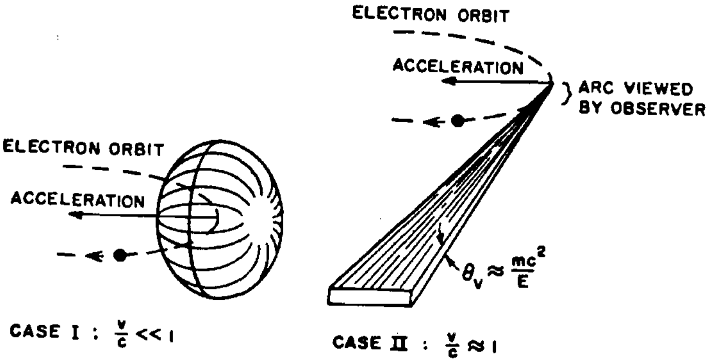

Figure 2.12 - Radiation emission pattern of electrons in circular motion: Case I, nonrelativistic electrons. Case II, relativistic electrons [38]

The radiation produced by these electrons travelling close to relativistic velocity is termed synchrotron radiation. This radiation is highly collimated, 100 % plane polarised in the orbit plane and has a continuous energy distribution from the infrared to the hard X-ray part of the electromagnetic spectrum. This wide range makes synchrotron radiation a remarkably tunable source.

The power of the synchrotron radiation emitted from an accelerator is shown in eqn. 2.12 adapted from reference 32. In order to maximise the synchrotron radiation a smaller radius is preferable as well as using a lighter charged particle such as an electron instead of protons or positrons.

$$Power \propto \frac{E^4}{m^4 R^2} \quad \textbf{2.12}$$

where: E is the energy of the particle

m is the mass of the particle

R is the radius of the curved path [39]

2.4.3 Synchrotron Far-IR Spectroscopy

The far-IR region is defined as the part of the infrared spectrum below 700 cm^{-1}, and is the only part of the spectrum investigated within this thesis. In the 1970s, calculations indicated that synchrotron radiation could be used as a source of infrared radiation [39, 40] in addition to X-rays [41] and UV radiation [42].

Due to the large flux of synchrotron radiation, as a source, it is able to overcome the "energy limit" problem, which describes the difficulty in achieving good signal to noise ratios in the far-IR region. Using synchrotron radiation the data acquisition time can also be greatly reduced.

Other advantages of synchrotron radiation in comparison to a black body source are that the radiation produced is highly focussed and collimated which allows small samples to be studied as well as obtain a high level of resolution. These advantages lend themselves well to RAIRS of adsorbates on single crystals which requires a small image size, due to grazing incidences, and low beam divergence, the product of which is known as the étendue.

RAIRS combines both high sensitivity, about 0.01 monolayers of a strong absorber, and high resolution, typically 1 cm^{-1}. These factors make it a very attractive technique for surface scientists. It has been suggested that in order to obtain the same intensity far-IR radiation as a synchrotron source, a globar would need to be heated to over 90,000 K [43]. The other method of increasing the intensity of a globar source is to increase the étendue of the source, however this would, as mentioned earlier, be detrimental to the RAIRS experiment.

The high brilliance of the synchrotron source is approximately 1000 fold increase on that obtained from conventional sources. Although in reality it is not this clear cut, as the emittance of the synchrotron radiation varies as a function of the wavelength being considered. Due to the diffractive splitting of the beam the SRS has an absolute lower limit of 100 cm^{-1}, and the emittance falls off with increasing wavenumber throughout the far and mid infrared. It decreases from 1 to 10^{-4} mm^2 sr, between 10 and 3300 cm^{-1}. This means that at higher wavenumbers the emittance falls below that required for RAIRS, as such synchrotron radiation only gains an advantage over thermal sources in the far-IR region for RAIRS studies

A final advantage of using synchrotron radiation for the RAIRS experiment is associated with the polarisation of the light. As mentioned previously the surface selection rule states that light must be polarised perpendicular to the surface. The light emanating from the synchrotron is polarised in the plane of the storage ring, which will be perpendicular to a vertically mounted sample.

One major drawback associated with synchrotron radiation as a source for far-IR experiments regards the stability of the beam. A globar will remain in a constant position and the intensity of the signal will also remain consistent. However, with the SRS, the beam position can "relax" within the system the longer the beam is stored, which means the optimal position for experimentation can change over time. This fact, combined with the gradually degradation in signal as the beam energy drops, means experiments can suffer from long term drift. These factors promote having rapid data collection, as such 256 co-added scans are more preferable with SR far-IR RAIRS to a higher number of scans.

The comparison of synchrotron to blackbody sources for IR experiments has been discussed and quantified in greater detail in a number of reports in the literature, which have been condensed into a number of pertinent reviews [44, 45].

2.5 Detecting Infrared Radiation

Infrared detectors are often required to be highly sensitive, monitoring absorption changes of 0.1 %. The sensitivity of a detector is quantified by the "amount of radiant power which must fall on it to give a root mean square electrical signal equal to the rms value of the noise introduced by the detector" [46], this is referred to as the Noise Equivalent Power (NEP). Most detectors have an NEP of 10^{-8}-10^{-10} W at room temperature, this value is too high for general surface infrared spectroscopy as the power reaching the detector is only 10^{-7} W. In order to lower the noise of the detector they are cooled either by liquid nitrogen or helium.

Two main types of detector exist for infrared experiments; photoconductive instruments and thermal detectors. Thermal detectors are better in low level background environments, they also have a slower reaction time than the photoconductive instruments. Traditionally photoconductive detectors had the limitation of a limited spectral range and therefore the detector needed to be specifically chosen for the experiment. The range of detection is related to the band gap of the material used in the detector, the smaller the band gap, the lower the wavenumber. With mercury cadmium telluride alloys the band gap can be continually altered by varying the composition of the HgTe and CdTe mixture [34], however those mixtures with small band gaps suffer from worse detectivity. Photoconductive detectors often work best with dispersive instruments as they can suffer from non-linearity which would affect their response with interferometry.

On beamline 13.3 a liquid helium cooled Si bolometer is used to monitor the IR beam. The detector consists of an absorber, in this case silicon, which has a thermal capacity, C, and is thermally connected to a heat reservoir at temperature T_0 by a weak thermal link, conductance G. The silicon is exposed to the power of the incoming light, Q, and an electrical bias power, P = IV. With this method the change in temperature of the absorber can be calculated by equation 2.13. The set up of a bolometer is shown in figure 2.13.

$$T = T_0 + \frac{(P+Q)}{G} \qquad \textbf{2.13}$$

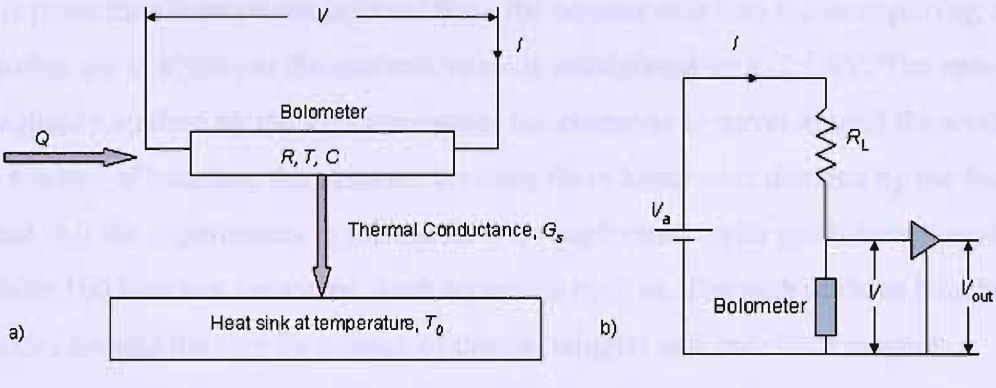

Figure 2.13 – Diagrams of a) the bolometric detector and b) the electrical bias and measuring circuit.

The temperature rise experienced by the absorber causes its resistance to change and as such the voltage across it, this change is then amplified and then measured. Due to this, materials which are chosen for the absorber, need to have a large change in resistance for a small change in temperature.

2.6 UHV RAIRS at the Daresbury Synchrotron Radiation Source (SRS)

The UHV RAIRS data presented in this thesis were obtained on beamline 13.3 at the SRS in Daresbury, UK. The UHV chamber was set up in such a way that synchrotron radiation was used as the primary infrared source, with a globar available as a backup source.

2.6.1 The Daresbury SRS

The SRS at Daresbury, as with most synchrotron facilities, consists of a linear accelerator (LINAC), a booster ring and a storage ring. The LINAC produces an electron beam, which is accelerated by a klystron. This klystron produces microwaves which interact with the electrons and gives them an energy boost to propel them along. Once the beam has reached an energy of 12 MeV it is injected into the booster ring.

Once in the booster ring the electron beam is further accelerated to 600MeV and at this point the electrons are injected from the booster ring into the storage ring. Using another set of klystrons the electron beam is accelerated up to 2 GeV. The radio frequency applied by the klystron causes the electrons to travel around the storage ring in a series of bunches, the distance between these bunches is dictated by the frequency used. All the experiments in this thesis were performed under multi-bunch mode, where 160 bunches are stored, each separated by 2 ns. The path of these bunches are guided around the ring by a range of dipole, wiggler and undulator magnets.

As the electrons pass around the ring they can collide with any gas molecules present. To reduce this risk the storage ring is kept under ultra high vacuum conditions, typically 10^{-10} mbar. Despite this, collisions still occur and with each one the electrons lose energy and so the beam current decays. To keep a reasonable beam the electrons are dumped and refills occur typically every 12 hours.

The UHV RAIRS data presented in this thesis were obtained on beamline 13.3 at the SRS in Daresbury, UK. The UHV chamber was set up in such a way that synchrotron radiation was used as the primary infrared source, with a globar available as a backup source.

2.6.2 *Experimental setup of far-IR beamline 13.3 at Daresbury*

Due to the large divergence of the infrared beam when leaving the storage ring the first mirror (M_1) used to deflect the beam, so that it can be used on the 13.3 beamline, needs to be placed as close as possible to the ring. This enables the mirror to collect as much radiation as possible whilst keeping the size of the mirror to a minimum. The arrangement of the first two mirrors is shown in figure 2.14, the plane mirror (M_1) deflects the beam vertically through the concrete shielding to the second elliptical mirror (M_2), which deflects the beam horizontally.

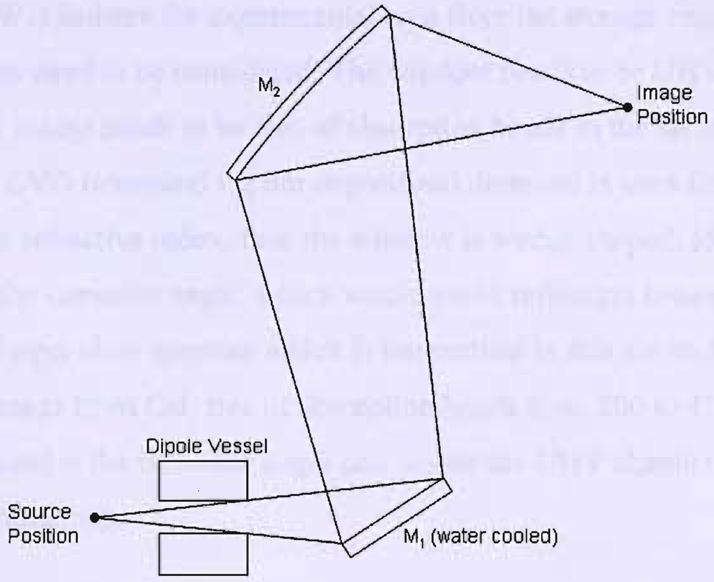

Figure 2.14 – The initial beam transport from the SRS to the end station [47]

The experimental part of the system, from M$_2$ onwards is shown in figure 2.15. The chamber is equipped with a quadrupole mass spectrometer (QMS) (C), an ion gun (J), low energy electron diffraction (LEED) optics (I), X-ray gun (D), hemispherical analyser (E) and reflection adsorption infrared spectroscopy windows (W$_2$ and W$_3$).

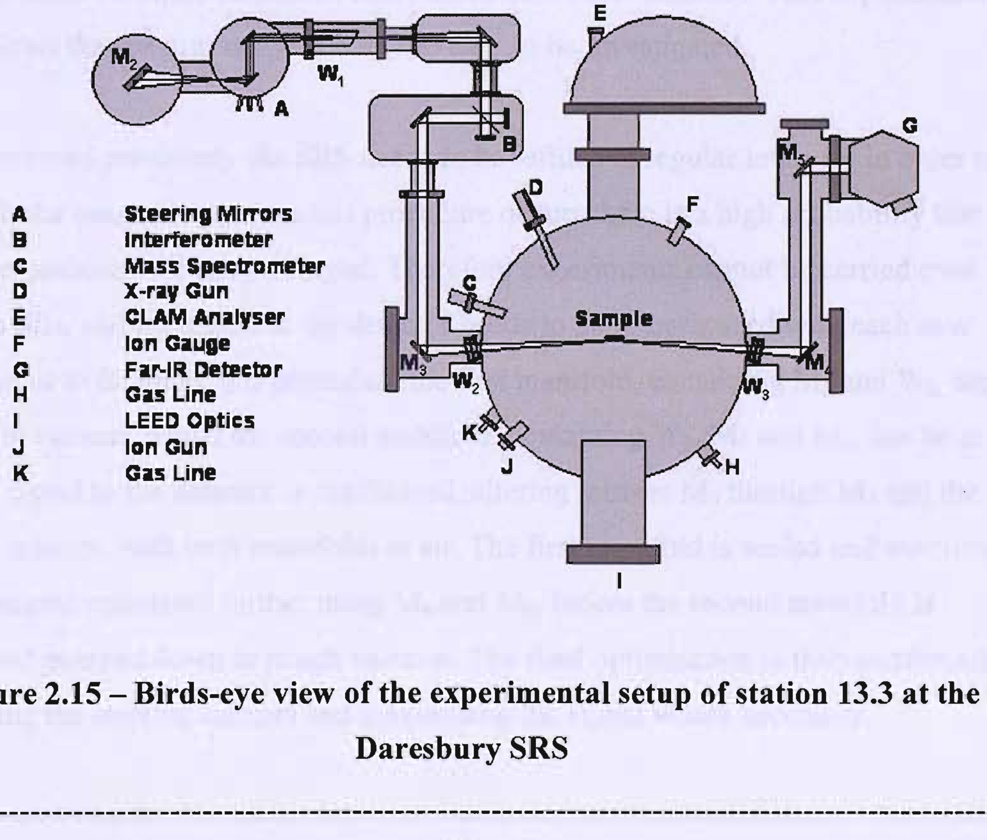

Figure 2.15 – Birds-eye view of the experimental setup of station 13.3 at the Daresbury SRS

Window one (W_1) isolates the experimental area from the storage ring. As such, a number of factors need to be considered. The window needs to be UHV compatible, to ensure isolation, it also needs to be free of absorption bands in the far infrared region, 20 – 1000 cm^{-1}. CVD (chemical vapour deposition) diamond is used for this window, which has a high refractive index, thus the window is wedge shaped. Ideally this would be set at the Brewster angle, which would avoid reflection losses, this would require a much larger clear aperture which is impractical in this situation. Windows W_2 and W_3 are made from CsI, free of absorption bands from 200 to 4000 cm^{-1}; these windows are placed at the Brewster angle and isolate the UHV chamber from the beam transport manifolds.

Once the infrared beam is in the plane of the 13.3 UHV chamber, the light is deflected, via M_2, to a set of steering mirrors, A. The beam then passes through W_1 and is directed, via the interferometer, B, and through a set of manifolds at rough vacuum, by additional optics to the UHV chamber through W_2. The beam is reflected at near-grazing incidence off the single crystal metal surface, and exits via W_3 into a second manifold also at rough vacuum. Due to the arrangement of the system and the nature of synchrotron radiation, the light used is polarised perpendicular to the surface. Once the light has passed into the second manifold it is directed by two further mirrors into a far-infrared liquid helium cooled silicon bolometer detector. This experimental setup allows the spectral range 200 to 700 cm^{-1} to be investigated.

As mentioned previously the SRS needs to be refilled at regular intervals in order to replenish the beam. Every time this procedure occurs there is a high probability that the beam position will have changed. Therefore experiments cannot be carried over between fills, and the signal to the detector needs to be re-optimised with each new fill. In order to facilitate this procedure the first manifold, containing M_3 and W_2, can be held in vacuum whilst the second manifold, containing W_3, M_4 and M_5, can be at air. The signal to the detector is maximised, altering mirrors M_3 through M_5 and the steering mirrors, with both manifolds at air. The first manifold is sealed and evacuated and the signal optimised further using M_4 and M_5, before the second manifold is sealed and pumped down to rough vacuum. The final optimisation is then confirmed by altering the steering mirrors and maximising the signal where necessary.

2.7 References

1. Vickerman, J.C., *Surface Analysis - The Principal Techniques.* 1997, Chichester: John Wiley & Sons Ltd.
2. McCash, E.M., *Surface Chemistry.* 2001, Oxford: Oxford University Press.
3. Samorjai, G.A., *Introduction to Surface Chemistry and Catalysis.* 1994, New York: John Wiley & Sons Ltd.
4. Chung, Y.W., *Practical Guide to Surface Science and Spectroscopy.* 2001, San Diego: Academic Press.
5. Seah, M.P. and Briggs, D., *Practical Surface Analysis by Auger and X-ray Photoelectron Spectroscopy.* 1992, Chichester: John Wiley & Sons Ltd.
6. Clarke, L.J., *Surface Crystallography - An Introduction to Low Energy Electron Diffraction.* 1985, Salisbury: John Wiley & Sons Ltd.
7. Attard, G. and Barnes, C., *Surfaces.* Oxford Chemistry Primers, ed. R.G. Compton. Vol. 59. 1998: Oxford University Press.
8. Surman, M., Hagans, P.L., Wilson, N.E., Baily, C.J., and Russell, A.E., *Surf. Sci.*, 2002. **511**(1-3): p. L303.
9. Raval, R., Parker, S.F., Pemble, M.E., Hollins, P., Pritchard, J., and Chesters, M.A., *Surf. Sci.*, 1988. **203**(3): p. 353.
10. McIntyre, J.D. and Aspnes, D.E., *Surf. Sci.*, 1971. **24**(2): p. 417.
11. Francis, S.A. and Ellison, A.H., *J. Opt. Sci. Am.*, 1959. **49**: p. 131.
12. Hayden, B.E., Kretzschmar, K., Bradshaw, A.M., and Greenler, R.G., *Surf. Sci.*, 1985. **149**(2-3): p. 394.
13. Greenler, R.G., *J. Phys. Chem.*, 1966. **44**: p. 310.
14. Greenler, R.G., *J. Phys. Chem.*, 1969. **50**: p. 1963.
15. Hoffmann, F.M., *Surf. Sci. Rep.*, 1983. **3**: p. 107.
16. Ortega, A., Hoffmann, F.M., and Bradshaw, A.M., *Surf. Sci.*, 1982. **119**: p. 79.
17. Hammaker, R.M., Francis, S.A., and Eischens, R.P., *Spectrochim. Acta*, 1965. **21**: p. 1295.
18. Moskovits, M. and Hulse, J.E., 1978. **78**: p. 397.
19. Pfnur, H., Menzel, D., Hoffmann, F.M., Ortega, A., and Bradshaw, A.M., *Surf. Sci.*, 1980(93): p. 431.
20. Persson, B.N.J. and Ryberg, R., *Phys. Rev. B*, 1981. **24**: p. 6954.

21. Blyholder, G., *J. Phys. Chem.*, 1964. **68**: p. 2773.
22. Blyholder, G., *J. Phys. Chem.*, 1975. **79**: p. 756.
23. Crossley, A. and King, D.A., *Surf. Sci.*, 1977. **68**: p. 528.
24. Shigeishi, R. and King, D.A., *Surf. Sci.*, 1976. **58**: p. 379.
25. Hollins, P. and Pritchard, J., *Surf. Sci.*, 1979. **89**: p. 489.
26. Hollins, P. and Pritchard, J., *Chem. Phys. Lett.*, 1980. **75**: p. 378.
27. Grimley, T.P., *Proc. Phys. Soc. (London)*, 1962. **79**: p. 1203.
28. Ortega, A., Garbout, A., Hoffmann, F.M., Stenzel, W., Unwin, R., Horn, K., and Bradshaw, A.M. in *IVC-8, ICSS-4, ECOSS-3*. 1980. Cannes.
29. Bell, R.J., *Introductory Fourier Transform Spectroscopy*. 1972, New York: Academic Press.
30. Chamberlain, J., *The Principles of Interferometric Spectroscopy*. 1979, New York: John Wiley.
31. Michelson, A.A., *Phil. Mag.*, 1892. **34**: p. 280.
32. Lord Rayleigh, *Phil. Mag.*, 1892. **34**: p. 407.
33. Griffiths, P.R., *Transform Techniques in Chemistry*. 1978, London: Heyden.
34. Chabal, Y.J., *Surf. Sci. Rep.*, 1988. **8**: p. 211.
35. Williams, R., *Spectroscopy and the Fourier Transform: An Interactive Tutorial*. 1996, Cambridge: VCH Publishers, Inc.
36. Bradshaw, A.M. and Schweizer, E. Advances in Spectroscopy, ed. R.J.H. Clark and R.E. Hester. Vol. 23. 1988, Chichester: Wiley. 413.
37. Lambert, D.K., *J. Elec. Spectr. Rel. Phen.*, 1983. **30**: p. 59.
38. Winick, H. and Doniach, S., *Synchrotron Radiation Research*. 1980, New York: Plenium Press.
39. Stevenson, J.R., Ellis, H., and Bartlett, R., *Appl. Optics*, 1973. **12**(12): p. 2884.
40. Duncan, W.D. and Williams, G.P., *Appl. Optics*, 1983. **22**(18): p. 2914.
41. Kunz, C., *Synchrotron Radiation - Techniques and Applications*. 1979, Berlin: Springer-Verlag.
42. Madden, R.P., Ederer, D.L., and Codling, K., *Appl. Opt.*, 1967. **6**: p. 31.
43. Yarwood, J., Shuttleworth, T., Hasted, J.B., and Nanba, T., *Nature*, 1984. **312**(5996): p. 742.
44. Hayden, B.E., *Reflection Absorption Infrared Spectroscopy*. Vibrational Spectroscopy of Molecules on Surfaces, ed. J.T. Yates and T.E. Madey. Vol. 1. 1987, New York: Plenum. 265.

45. Hollins, P. and Pritchard, J., *Prog. Surf. Sci.*, 1985. **19**: p. 275.

46. Conn, G.K.T. and Avery, D.G., *Infrared Methods*. 1960, New York: Academic Press. 65.

47. Slater, D.A., Hollins, P., Chesters, M.A., Pritchard, J., Martin, D.H., Surman, M., Shaw, D.A., and Munro, I.H., *Rev. Sci. Instrum.*, 1992. **63**(1): p. 1547.

Chapter Three – Theoretical Methods

3.1 Introduction

To aid the understanding of many experimental surface science investigations, electronic structure calculations are performed. With regards to this thesis, calculations are often used to help assign various infrared bands in the spectra obtained. These calculations focus on the known structures of copper oxides, CuO and Cu_2O, and on the vibrational modes of those structures.

The calculations were performed in a number of steps. First the basis sets for Cu and O, were obtained from the official CRYSTAL website [1]. These local basis sets are representations of atomic, or in the case shown here, ionic orbitals, and are linear combinations of Gaussian-type orbitals. These local orbitals are used to construct Bloch functions, which provide an approximation to the Schrödinger equation for a periodic system. This approximation is refined via a set of self consistent field iterations leading to an approximate ground state wavefunction. The lattice parameters and internal co-ordinates of the unit cell were then optimised. For the internal co-ordinates analytic first derivatives (gradients) are available while for the cell approximate gradients were constructed via finite differences. These calculations were performed using B3LYP, a hybrid density functional used as an approximation to the exchange and correlation potential, within the CRYSTAL06 program. With a slight change to the submitted code, the optimisation can be changed from the internal coordinates to that of the unit cell parameters. Once the ground state structure has been obtained via geometry optimisation, the force constants for different bonds within the structure can then be determined via finite differences of the first derivatives. This is not ideal but currently analytic second derivatives are not available within the CRYSTAL code. From these force constants the vibrational modes can be obtained.

3.2 Development of Computational Chemistry

3.2.1 The Schrödinger Equation

The major aim in quantum chemistry is the approximate solution of the time-independent, non-relativistic Schrödinger equation.

$$H\Psi = E\Psi \qquad \mathbf{3.1}$$

where: H is the Hamiltonian operator containing N electrons.

Ψ is the wavefunction for the system in question.

and E is the numerical value of the energy of the state described by Ψ.

Taken as a whole, even with modern day computational abilities, the Hamiltonian operator is too complicated for calculation of a solid. For example, a wavefunction needs to be calculated for each one of an essentially infinite number of electrons, spread over the entire space of the solid. A number of approximations have been developed in order to simplify the calculations.

3.2.2 Bloch's Theorem

One of the first important methods of reducing the number of necessary calculations was proposed by Bloch in 1928 [2]. The author proposed that if the ions in a perfect crystal, at 0 K, are arranged in a periodic manner, then the external potential felt by the electrons could also be related to this periodic nature – the unit cell. This can be expressed mathematically as shown in equation 3.2 where R is any lattice vector of the unit cell.

$$V(r) = V(r + R) \qquad \mathbf{3.2}$$

for any value of r.

With this starting point it is possible to present the wavefunction in a more general case as shown in equation 3.3.

$$\psi(r) = f(r)u(r) \qquad \textbf{3.3}$$

where u(r) is a periodic function as in equation 3.2 and f(r) is to be determined.

As the potential, V(r), is periodic, this dictates that all the observable quantities of an electron must also be periodic. Most importantly this carries through to the electron density, given by $|\psi(\mathrm{r})|^2$, and as such the following equation must be true.

$$|f(r+R)|^2 = |f(r)|^2 \qquad \textbf{3.4}$$

Only one function can satisfy this requirement for all values of R, this leads to the Bloch function given in equation 3.5 [3].

$$\psi_k r = e^{ik.r} u_k(r) \qquad \textbf{3.5}$$

where k is any allowed wave-vector for the electron.

Overall Bloch's theorem implies that the probability of finding an electron is the same at any equivalent point in a lattice, thus reducing the need to calculate the infinite number of one-electron wavefunctions down to a calculation of the one-electron wavefunctions for the number of electrons in the unit cell of a crystal.

3.2.3 The Born-Oppenheimer Approximation

Another of the very important approximations applied in quantum chemistry is the Born-Oppenheimer approximation [4] the basis of which is to consider the nuclei as fixed in space with the electrons free to move around them. This assumption is deemed reasonable due to the large mass differences between the nuclei and the electrons. On an electronic time scale this enables the kinetic energy of the nuclei to be set to zero and the potential energy due to inter-nuclear repulsion can be considered a constant.

3.2.4 The Hartree-Fock Approximation

A number of other simplifications are made, these are collectively embodied in the Hartree-Fock (HF) approximation, which is the cornerstone of all wavefunction based calculations. One part of the HF approximation is to ignore any potential relativistic effects on the mass of moving particles.

One of the important parts of the HF approximation involves the use of a Slater determinant (eqn 3.6) for the total wavefunction. When determining the properties of a material, using quantum mechanics, the correlations between electrons can be a major problem, largely in relation to the sheer number of interactions. The positions and motions of particles within a molecule are correlated because as they move, they interact and exert forces upon each other. The Pauli exclusion principle states that two spin parallel electrons will tend to avoid each other and as such have a very small electrostatic interaction. Consequently, two anti-parallel spin electrons will be unaffected and will be, on average, closer together and therefore have a larger electrostatic interaction. The Slater determinant assures an anti-symmeterised function from the outset, obeying the Pauli exclusion principle as the determinant will vanish if any of the two spin-orbitals are identical, for this leads to two identical rows.

$$\Psi(x_1, x_2, \ldots, x_N) = \frac{1}{\sqrt{N!}} \begin{vmatrix} \chi_1(x_1) & \chi_1(x_2) & \cdots & \chi_1(x_N) \\ \chi_2(x_1) & \chi_2(x_2) & \cdots & \chi_2(x_N) \\ \vdots & \vdots & & \vdots \\ \chi_N(x_1) & \chi_N(x_2) & \cdots & \chi_N(x_N) \end{vmatrix} \qquad \textbf{3.6}$$

where: Ψ is the total wave function.

N is the number of electrons.

and $\chi_i(x_j)$ are the spin-orbitals which indicate the position and spin of the electrons.

A new approximate operator can be formed, the Fock operator. This new Hamiltonian operator contains a sum of kinetic energy operators for each electron, the internuclear repulsion energy (as mentioned earlier, now a constant), a sum of nuclear-electronic coulombic atttraction terms and the electronic coulombic repulsion terms. This final term is composed of a net repulsion energy for every electron in the system, calculated by treating all other electrons as if they were a smooth distribution of negative charge. This Fock operator is then placed within the Schrödinger equation, which is then solved to produce a new set of approximate one-electron orbitals. These orbitals are then used to create another Fock operator which is reintroduced into the Schrödinger equation. This iterative procedure is continued until a negligible difference is found between two successive results. The results which provide these are then termed self-consistent one-electron orbitals, because of this, the routine is also called a self consistent field (SCF) procedure.

Whilst the HF approximation is still the starting point for many computational methods it has a few faults. The final assumption which leads to the electron correlation only considering spin parallel electrons and ignoring other electron interactions can bring about unacceptable errors in comparison to experiment. To correct for these errors a number of developments have been added and these are termed post-HF methods. Another disadvantage for Hartree-Fock theory is that it is based upon the complicated N-electron wavefunction, which in turn relies on 3N spatial and N spin based variables, which can be very heavy on computational power. Density functional theory (DFT) tries to replace the wavefunction by a far simpler quantity, the electron density.

3.2.5 The Hohenberg-Kohn Theorems

The first attempts to prove the legitimacy of using the electron density as the guiding system for computational chemistry are almost as old as quantum mechanics. The Thomas-Fermi model was proposed in 1927, and although not necessarily in use anymore, showed solid insights into the problem. Slater also added his own density based approximation to the HF exchange method in 1951, although not specifically with DFT in mind [5]. In truth, density functional theory as it is known today was born in 1964 with a paper entitled "Inhomogeneous Electron Gas" by Hohenberg and Kohn [6]. Within this paper the authors proved two of the theories on which modern day DFT is based.

The first Hohenberg-Kohn theorem proves that the electron density can uniquely define the Hamilton operator and, by association, all the properties of the system. The proof is approached by taking two external potentials, V_{ext} and V'_{ext}, which must differ by more than a constant, as a constant would not affect the wavefunction, and that these external potentials will lead to the same electron density, $\rho(r)$, associated with the corresponding non-degenerate ground states of N particles. The two differing external potentials will give rise to two Hamiltonians which will differ in this one respect, (Eqn 3.7a and b). These two Hamiltonians, by extension, will relate to two different ground state wavefunctions, Ψ and Ψ', and two differing ground state energies, E_0 and E'_0.

$$H = T + V_{ee} + V_{ext} \qquad \textbf{3.7a}$$

$$H' = T + V_{ee} + V'_{ext} \qquad \textbf{3.7b}$$

where: H is the Hamiltonian operator.
T is the kinetic energy of the electrons.
V_{ee} is the potential energy for the interaction between electrons.
and V_{ext} is the external potential energy.

By introducing the variational theorem; which states that if you know the Hamiltonian of a system, then any predicted normalized wavefunction, φ, will provide an expectation value of the Hamiltonian which will always be greater than or equal to the ground state energy; equations 3.7a and b can be worked to produce equations 3.8a and b.

$$E_0 < E'_0 + \int \rho(r)\{V_{ext} - V'_{ext}\}dr \qquad \textbf{3.8a}$$

$$E'_0 < E_0 - \int \rho(r)\{V_{ext} - V'_{ext}\}dr \qquad \textbf{3.8b}$$

On addition of these equations (eqn 3.9), it can be shown that the original hypothesis of two differing values for the external potential leading to the same electron density is impossible, and therefore proving that the electron density does indeed uniquely define the Hamiltonian.

$$E_0 + E'_0 < E'_0 + E_0 \qquad \mathbf{3.9}$$

The second Hohenberg-Kohn theorem again uses the variational theorem to prove that the Hohenberg-Kohn functional will deliver the lowest energy only if the input density is the ground state density, ρ_0. With these two theorems in mind the Hohenberg-Kohn functional, $F_{HK}[\rho]$, can be introduced, which concerns the kinetic energy, T, and the electron-electron interaction energy, E_{ee}, and can be considered universally valid.

$$F_{HK}[\rho] = (T[\rho] + E_{ee}[\rho]) \qquad \mathbf{3.10}$$

If this functional were known exactly, then the Schrödinger equation could also be solved exactly as the rest of the information needed to calculate the ground state energy, $E_0[\rho_0]$, is straight forward, if system dependant.

$$E_0[\rho_0] = \int \rho_0(r) V_{Ne} dr + F_{HK}[\rho_0] \qquad \mathbf{3.11}$$

where: V_{Ne} is the potential energy due to nuclei-electron attraction.

In this way Hohenberg and Kohn showed that DFT was a valid path to follow without providing information on how calculations could be performed.

3.2.6 The Kohn-Sham Approach

A year after the Hohenberg and Kohn paper [6], the second major paper of DFT was published by Kohn and Sham [7]. The authors realised that many of the problems surrounding direct density functionals were attributable to the way in which the kinetic energy was determined and that HF methods dealt with it much more successfully. The method introduced by Kohn and Sham uses a non-interacting reference system which is built from a set of orbitals (similar to HF methods) allowing the major part of the kinetic energy to be calculated in this way. This enables a large portion of the kinetic energy to be calculated exactly, leaving only a small part to be calculated by an approximate functional. The remainder of the kinetic energy to be determined is merged with non-classical contributions to the unknown, but fairly small, electron-electron repulsion. With this in mind Kohn and Sham introduced the exchange correlation energy, E_{XC}, defined in equation 3.12, and its relation to the main functional is shown in equation 3.13.

$$E_{XC}[\rho] \equiv (T[\rho] - T_S[\rho]) + (E_{ee} - J[\rho]) = T_C[\rho] + E_{ncl}[\rho] \qquad \textbf{3.12}$$

$$F[\rho(r)] = T_S[\rho(r)] + J[\rho(r)] + E_{XC}[\rho(r)] \qquad \textbf{3.13}$$

where: T_S is the kinetic energy predicted by the Kohn-Sham approach.

J is the classical Coulomb contribution to the electron-electron interaction.

T_C is the residual part of the true kinetic energy.

and E_{ncl} is the non-classical contribution to the electron-electron interaction.

The exchange correlation energy contains everything which is unknown; the non-classical effects of self-interaction correction, exchange and correlation, which contribute to the potential energy and a small quantity related to the kinetic energy. Once again if this factor could be calculated, then the Schrödinger equation could be solved exactly as thus far no approximations have been introduced. However this is as far as this procedure can get without attempting to approximate this exchange correlation energy and the quality of the density functional will rely on the accuracy of this approximation.

3.2.7 The Local Density Approximation (LDA)

This approximation forms the backbone of most approximate exchange correlation functionals used. The basis of this model concerns a hypothetical uniform electron gas, where electrons move around a positive background charge distribution which leads to an electrically neutral system. If the volume of the gas and the number of electrons are considered to approach infinity, then the electron density can be assumed to be constant. Whilst fairly unrealistic, this approximation is the only way to enable the exchange correlation energy to be calculated to a high degree of accuracy.

$$E_{XC}^{LDA}[\rho] = \int \rho(r)\varepsilon_{XC}(\rho(r))dr \qquad \textbf{3.14}$$

In this equation, ε_{XC} is the exchange correlation energy per particle of a uniform electron gas of density $\rho(r)$. This value can be split further into exchange, ε_X, and correlation, ε_C, segments, of which, the exchange segment has been derived by Bloch [8].

$$\varepsilon_X = -\frac{3}{4}\sqrt[3]{\frac{3\rho(r)}{\pi}} \qquad \textbf{3.15}$$

A number of approximations have been constructed for the correlation part over the years. Using the best of these, results for molecular properties, such as equilibrium structures, harmonic frequencies or charge moments, can be calculated with great success. However when considering the energetic properties of the system, such as bond energies, the LDA approach is rather unspectacular, even if it is still an improvement on HF methods. Typically Hartree-Fock methods underestimate atomisation energies etc. whereas LDA suffers in the opposite direction and generally overbinds, i.e. predicts a binding energy greater than that observed experimentally. The local density approximation predicts overbinding due to the method not coping well with atomic systems.

3.2.8 The Generalized Gradient Approximation (GGA)

The main theoretical step between LDA and GGA is how the density is taken into consideration. The generalised gradient approximation (GGA) uses not only the information about the density used in LDA but also how the charge density is changing in that area, or in other words the gradient of the density. To do this the local density approximation is placed as the first term of a Taylor expansion and is extended to the next lowest term. Unfortunately this straight forward approach removes many of the useful features of the LDA. In order to address these new problems, crude hole-constraints are introduced whereby if any feature violates the requirement of the system being negative everywhere then it is set to zero and effectively removed. How the gradient is detected and used once again relies on the introduction of a functional. The GGA version of the exchange correlation energy splits the exchange and correlation parts, with each part containing a functional. It is at this point where many groups have developed their own functionals, for example the PW91 [9] and B86 [10] functionals which are used to approximate the exchange part of the exchange correlation and the LYP [11] functional used to approximate the correlation part.

3.2.9 Hybrid Functionals

Whilst the GGA can provide a useful approach to many systems it in many ways makes life difficult, as it has already been stated that the exchange segment is already known exactly. As such the exact exchange energy can be taken from the Hartree-Fock system and the missing part can be filled in using Kohn-Sham approximate functionals for the correlation energy; these systems are termed hybrid functionals. However, the idea has undergone many changes during the 1990s in order to help the functional perform better, to the point that explaining the process would entail more detail than necessity dictates here. For example the B3LYP functional [12], used in this thesis, is shown below, it is one of the most successful functionals and equation 3.16 gives an indication of its complexity.

$$E_{XC}^{B3LYP} = (1-a)E_X^{LSD} + aE_{XC}^{\lambda=0} + bE_X^{B88} + cE_C^{LYP} + (1-c)E_C^{LSD} \qquad \textbf{3.16}$$

In this equation, a is a constant which controls the contribution of exact exchange, whilst b and c control quantities of exchange and gradient correlations to the local density approximation. In essence, the functional takes the exact exchange given by the Hartree Fock approximation and damps it to a more reasonable level, as if the dielectric constant of the material being investigated had been taken into account.

The B3LYP functional is used within the calculations presented within this thesis, a review of the main qualities of this functional and a comparison to other functionals mentioned above can be found in the second half of Koch and Holthausen's book [4].

3.3 Calculation Procedure

As mentioned previously the starting point for a calculation is the basis set for each element involved in this case the 86-4111(41d)G basis set [13] is used for Cu. The name of the basis set is derived systematically from how it has been constructed; G indicates the basis set is constructed from Gaussian orbitals; 8, 6 and 4 are the number of orbitals used to simulate the 1s, 2s2p and 3s3p shells respectively. The 4s4p and 5s5p shells are simulated as split valence shells using 1 Gaussian each, the 3d simulated by 4 Gaussians and a split 4d shell with 1 Gaussian. This basis set has been designed for positive ions of copper only, which allows the 4s state to be under-defined in comparison to what would be required for the neutral $4s^1$ state. Another basis set is required for oxygen, in this case the 8-411G [14], which is named systematically as before.

The other major factor in the calculation is to input the ionic structure of the system of interest. In this case fortunately the lattice structures for both CuO and Cu_2O are known and are shown in table 3.1. The positions where each atom is situated within the unit cell are also added to the calculation and are shown in table 3.2.

Oxide	a / Å	b / Å	c / Å	α / °	β / °	γ / °
CuO[15]	4.68	3.42	5.13	90.00	99.54	90.00
Cu_2O[16]	4.27	4.27	4.27	90.00	90.00	90.00

Table 3.1: Structures of the common copper oxides

CuO	(x, y, z) co-ordinates
Cu(1)	(¼, ¼, 0)
Cu(2)	(¾, ¼, ½)
O(1)	(0, 0.4184, ¼)
O(2)	(0, 0.4184, ¾)
Cu_2O	
Cu	(0, 0, 0)
O	(¼, ¼, ¼)

Table 3.2 – Internal co-ordinates for copper and oxygen in the unit cell

These values are, however, just a starting point and the internal coordinates of the system need to be optimised. This is achieved by finding the forces acting upon each point using a SCF procedure, once the energy change in successive cycles is minimal for a point, the next is considered. Comparison of the theoretical predicted values to the recognised structure gives an estimate of the error in the calculations. After this the individual forces can then be placed upon the atoms and the minimised energy structure can be obtained, being optimised with the BFGS algorithm [17-20], or damped molecular dynamics.

Once this has been achieved a change to the input code enables the cell to be optimised. Within the code used in this thesis work there was no opportunity to use analytical stresses directly upon the cell and therefore a different procedure to that used for the internal coordinates needed to be followed. The procedure followed a finite difference method, where lattice parameter a is given an energy E_1, and lattice parameter b, where $b = (a + x)$, is given an energy E_2. The energy values can be optimised using an SCF system and the force can then be calculated as

$(E_1 - E_2) / (a - b)$. The geometry can then be optimised by finding a local energy minimum using the BFGS algorithm or damped molecular dynamics.

With an optimised structure it is now possible to calculate the phonon modes associated with that structure. This is achieved by moving two atoms by a small amount and monitoring the forces present in those positions. Using a finite difference method upon those forces the second derivative can be obtained. This second derivative will provide the force constant of the bond between the two atoms. This process is repeated throughout the lattice and a matrix is constructed with the force constants. Upon diagonalisation of this matrix the frequencies are obtained as the eigenvalues and the shifts associated with those modes as the eigenvectors. It should be noted that this procedure gives all the vibrational modes of the system and the IR and Raman active modes need to be selected from those obtained.

The procedure followed was similar for the calculations performed for both CuO and Cu_2O. However the setup of the input had some noticeable differences. These calculations are concerned with the electrons within the crystal structure, meaning the different oxidation states of copper play an important role. The oxidation state of Cu in Cu_2O is +1 which means the electronic structure involves a full 3d shell leading to a non-magnetic character. For CuO the oxidation state is +2 leading to nine electrons in the 3d shell, however CuO does not behave as one might expect a $3d^9$ transition metal compound to. Copper (II) oxide is instead a strongly correlated insulator of the "charge-transfer" type according to the theory of Zanaan *et al.*[21], and it undergoes two magnetic transitions. Below $T_{N1} = 231$ K an incommensurate magnetic structure is observed and at $T_{N2} = 212.5$ K an antiferromagnetic structure is formed [22]. To understand this structure better, a detailed powder diffraction study was performed by Yang *et al.*[23] combined with polarised neutron diffraction. The authors found that the magnetic unit cell has a volume twice that of the chemical unit cell with spin directions alternating along the $[10\bar{1}]$ chains. In order to compensate for this effect the calculation uses the 'SUPERCELL' instruction which repeats the positions of the unit cell whilst allowing the spins to be set on each individual ion.

3.4 References

1. http://www.crystal.unito.it/.
2. Bloch, F., *Z. Physik*, 1928. **52**: p. 555.
3. Omar, M.A., *Elementary Solid State Physics*. 1975, Massachusetts: Addison-Wesley Publishing Company Inc.
4. Koch, W. and Holthausen, M.C., *A Chemist's Guide to Density Functional Theory*. 2000, Weinheim: Wiley-VCH.
5. Slater, J.C., *Phys. Rev.*, 1951. **81**: p. 385.
6. Hohenberg, P. and Kohn, W., *Phys. Rev.*, 1964. **136**: p. B864.
7. Kohn, W. and Sham, L.J., *Phys. Rev.*, 1965. **140**: p. A1133.
8. Bloch, F., *Z. Physik*, 1929. **57**: p. 545.
9. Perdew, J.P., *Unified Theory of Exchange and Correlation Beyond the Local Density Approximaton*. Electronic Structure of Solids, ed. P. Ziesche and H. Eschrig. 1991, Berlin: Akademie Verlag.
10. Becke, A.D., *J. Chem. Phys.*, 1986. **84**(8): p. 4524.
11. Lee, C.T., Yang, W.T., and Parr, R.G., *Phys. Rev. B*, 1988. **37**(2): p. 785.
12. Stephens, P.J., Devlin, F.J., Chabalowski, C.F., and Frisch, M.J., *J. Phys. Chem.*, 1994. **98**(45): p. 11623.
13. Towler, M.D., Dovesi, R., and Saunders, V.R., *Phys. Rev. B*, 1995. **52**(14): p. 10150.
14. Towler, M.D., Harrison, N.M., and McCarthy, M.I., *Phys. Rev. B*, 1995. **52**(7): p. 5375.
15. Kliche, G. and Popovic, Z.V., *Phys. Rev. B.*, 1990. **42**(16): p. 10060.
16. Balamurugan, B. and Mehta, B.R., *Thin Solid Films*, 2001. **396**(1-2): p. 90.
17. Broyden, C.G., *J. Inst. Math. Appl.*, 1970. **6**: p. 76.
18. Fletcher, R., *Comp. J.*, 1970. **13**: p. 317.
19. Goldfarb, D., *Math. Comp.*, 1970. **24**: p. 23.
20. Shanno, D.F., *Math. Comp.*, 1970. **24**: p. 647.
21. Zaanen, J., Sawatsky, G.A., and Allen, J.W., *Phys. Rev. Lett.*, 1985. **55**: p. 418.
22. Yang, B.X., Thurston, T.R., Tranquada, M., and Shirane, G., *Phys. Rev. B*, 1989. **39**(7): p. 4343.
23. Yang, B.X., Tranquada, M., and Shirane, G., *Phys. Rev. B*, 1988. **38**: p. 174.

Chapter Four – The Far-IR High Pressure Reaction Cell

4.1 Introduction

Copper is one of the most widely used elements, it is utilised in a large range of catalytic processes due to its high activity and selectivity as an oxidation/reduction catalyst [1]. The oxidation state of copper changes as a function of temperature and oxygen partial pressure, between Cu, Cu_2O (cuprite) and CuO (tenorite) as shown by the Pourbaix diagram in figure 4.1.

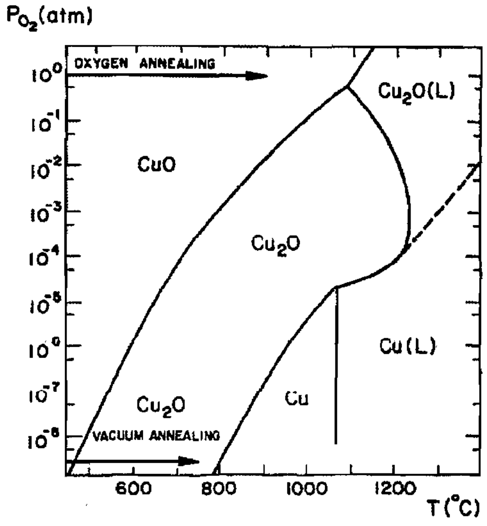

Figure 4.1 – Pressure vs. temperature diagram showing the stability of different copper and oxygen mixtures [2]

Copper has found a use in high speed, reduced sized circuits thanks to its low thin film resistivity and high electro-migration resistance [3]. A major drawback of using copper in these systems is the ease with which it oxidises and that this process is not self-limiting as it is, for example, with aluminium. The copper oxides are often chemically and mechanically unstable under the standard working conditions of the circuits.

Copper oxides have also evoked much interest due to the close relation to high T_C superconductors which often contain Cu_2O planes. Not only this, but CuO also shares many physical and chemical attributes found in many undoped antiferromagnetic cuprates, e.g. La_2CuO_4 and $YBa_2Cu_3O_6$ [4, 5].

It becomes clear then, why there is a large body of work available on copper, its oxides and the formation thereof; which makes it useful to test new theories and equipment upon. However, the oxidation process itself is still not fully understood, which leads to new research being published in the area every year.

Reflection Absorption Infrared Spectroscopy (RAIRS) has over the years, been shown to be a very powerful technique for monitoring molecular adsorption at crystal surfaces, many of the best examples of this are discussed in Chapter 1. To reduce the complexity of the observed reactions the samples are often kept under ultra high vacuum (UHV) conditions, which allow the surfaces to be cleaned to an atomic level. However, with most UHV chambers this restricts the maximum exposure pressure for the reactants. These reduced pressures can lead to misinterpreted results when it comes to real world catalysis.

In this chapter the design of a system which allows IR data to be collected at more realistic gas pressures is discussed. RAIRS is a photon based spectroscopic technique and is unaffected by higher gas pressures, unlike other electron based surface science techniques. This benefit means the system could be developed within the existing UHV chamber based on the far-IR beamline at Daresbury laboratory, as opposed to designing an entirely new piece of equipment.

4.1.1 The Interaction of Oxygen and Cu(100) in Surface Science

For this adsorption system a number of disagreements have appeared in the literature, and are briefly reviewed in this section; the saturation coverage of the O/Cu(100) system has raised wide discussion in the literature, the presence of a faint four spot LEED pattern during low-level exposure of oxygen to the Cu(100) surface, observed by Lee and Farnsworth [6], the origin of which was a keen focal point for many years. And finally the nature of a reconstruction of the surface upon oxygen exposure remained unconfirmed until more recently.

The saturation coverage of oxygen adsorbed on a Cu(100) surface has at times been proposed to be ¾ of a monolayer [7, 8], however more recently it has been confirmed to be ½ monolayer coverage [9].

In the literature up to three superstructures have been proposed for the adsorption of O on Cu(100), these are the aforementioned four-spot structure, centred on the (½, ½) positions, a (√2 x √2)R45° structure also known as a c(2 x 2) structure and a (2√2 x √2)R45° structure [10].However, some authors have acknowledged only the presence of the (2√2 x √2)R45° structure, attributing the four-spot LEED pattern to the fact that the expected quarter-order spots are too weak to be detected, and excluding the c(2 x 2) phase entirely (refs). It is worth noting that many of these investigations involved either high adsorption temperatures or annealing at relatively high temperatures which is known to favour the formation of the (2√2 x √2)R45° structure. It was eventually confirmed that a pseudo c(2 x 2)-O phase occurs below 0.34 ML coverage, which exists without long range order. It was proposed from SEXAFS [11] that the structure involved atomic oxygen adsorbed in the four-fold hollow sites present on the Cu(100) surface, and confirmed a few years later by scanning tunnelling microscopy performed by Fujita *et al.*[12] . The authors found the phase consists of grouped nano-sized c(2 x 2) domains, with a high density of anti-phase domain boundaries, which reaches a maximum around 0.3 ML. Using HREELS the vibrational frequencies of the metal-adsorbate bond for these two structures have been obtained. The two υ(Cu-O) frequencies, 290 cm^{-1} [(2√2 x √2)R45°] and 340 cm^{-1} [c(2 x 2)], are suitably different in order to allow differentiation between these structures using vibrational techniques [9, 13].A third, highly reactive, type of oxygen adsorbate has also been detected, with υ(Cu-O) around 380 cm^{-1}, the higher stretching frequency of this bond indicates the species being adsorbed at lower coordination sites [14].This species is observed when Cu(100) is exposed to oxygen at low temperature (100 K) and disappears upon annealing to 300 K, suggesting that it is due to oxygen atoms which lack the energy to move to the more stable four-fold hollow adsorption sites.

A reconstruction of the Cu(100) surface occurs upon formation of the (2√2 x √2)R45° structure which has been observed with STM [15], LEED I(V) [16] and XRD [17]. The reconstruction is viewed as an oxygen covered (100) face where every fourth Cu row is missing in both the [001] and [010] directions. Tanaka *et al.* [18] explained the driving force behind the reconstruction as the same reason large c(2 x 2)-O domains are not formed upon the Cu(100) surface. The authors found that although oxygen atoms readily migrated across the surface at room temperature, from one c(2 x 2) phase to a nearby anti-phase c(2 x 2) domain, no large single phase c(2 x 2) domains existed. This was assumed to be due to a non-linear proportional increase in the adsorption induced local stress as the domain size increased. The large stress associated with the formation of a large c(2 x 2)-O domain was therefore assigned as the driving force behind the reconstruction observed upon formation of the (2√2 x √2)R45° structure.

It is worth noting that during the work presented in this thesis the level of noise experienced upon beamline 13.3 would have unfortunately been too high to observe any of these features, before the larger bulk oxidation effects were observed.

4.1.2 The Oxidation of Copper at Realistic Pressures

As with many areas of science further discoveries make some sections of earlier work obsolete as understanding and the availability of better technology grows. Despite this, the comprehensive reviews of the early work on the oxidation of bulk copper by Tylecote [19] and from Ronnquist and Fischmeister [20] are still relevant. In the 1960s and earlier, due to limited resources it was very difficult to obtain exact stoichiometries for the oxides formed upon bulk copper and the time scale to fully oxidise a sample of bulk copper would be unfeasible, research turned to the oxidation of thin films of copper instead. Equipment was developed by Wieder and Czanderna [21] which utilised a transparent substrate, attached to a microbalance, upon which copper was evaporated. In this manner, it was not only possible to calculate the thickness of the copper film deposited, due to weight gain and known deposition area, but also to monitor any changes occurring due to oxidation, via weight gain. Optical measurements were also possible due to the transparent substrate. Copper films ranging in thickness between 200 and 1630 Å were investigated by the group. The films were heated in 100 Torr (133 mbar) of oxygen and the oxidation monitored at progressively higher temperatures. Five regions of interest were observed during the oxidation process as shown in figure 4.2.

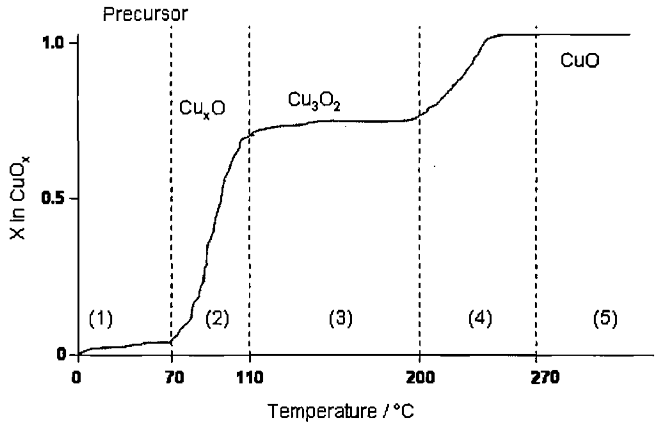

Figure 4.2 - Formation of different copper oxides as a function of temperature at 133 mbar O_2, developed from reference 8.

In region (1) oxidation progresses slowly with the growth of an amorphous oxide. In regions (2) and (4) oxidation occurs but as a rate limited process, and as film thickness increases the uptake of oxygen was found to decrease. In the region above 270 °C oxygen uptake ceased and the ratio of Cu to O was found to be 1:1 showing that oxidation had reached conclusion and cupric oxide, CuO, had formed. It is in region (3) where an unexpected feature was observed, once again there was a period of negligible uptake of oxygen, it was concluded a stable oxide had been formed. The composition of the oxide was not $CuO_{0.5}$ as might have been expected, but rather $CuO_{0.67}$. It was found that this stable oxide form could be obtained by direct oxidation on films between 200 and 1085 Å thick. However with a thicker film, 1630 Å, oxidised at 180 °C, a stable oxide occurred with the expected composition of $CuO_{0.5}$, or Cu_2O, after approximately 25 hours. It was only by increasing the temperature to 200 °C and leaving for 100 hours that $CuO_{0.67}$ was obtained. The stability of the different oxide layers was also confirmed with optical transmission measurements which only changed during regions (1), (2) and (4), i.e. when oxygen uptake occurred. Weider and Czanderna concluded that $CuO_{0.67}$ was a gross defect structure of Cu_2O. They were, however, unable to provide evidence to conclude that a meta-stable, ordered Cu_3O_2 structure existed. The authors found that the electron diffraction patterns of Cu_2O and $CuO_{0.67}$ were identical, but that the oxides could be distinguished due to a greater optical band gap for $CuO_{0.67}$ than that of Cu_2O; 2.20 and 1.95 eV respectively. This work was later supported by Lefez *et al.*[22] who reported that oxidation of bulk copper in dry synthetic air, at 150 °C, for 96 hours led to the formation of Cu_3O_2. This data led to the suggestion that such a composition of copper oxide will not rapidly form on bulk copper, as temperatures any higher would drive the oxidation to form CuO instead.

In a continuation of the work in reference 8, it was found that thin single crystal films, in this case (100) Cu films, oxidised fully quicker than polycrystalline films of similar thickness [23]. However, it was also found that for single crystal films thicker than 505 Å the stable oxide ratio shifted closer to $CuO_{0.5}$ in contrast to the 1085 Å for polycrystalline films, as described above. The authors argued that the single crystal films were not as continuous as the deposited polycrystalline films and that any errors in film thickness could be assigned to the presence of voids.

Under slightly less oxidising conditions, 76 mm Hg (101 mbar) oxygen, temperature shifts from this behaviour were noted by Hapase *et al.*[24] with a polycrystalline copper film, 860 Å. Despite this, the formation of a stable phase of $CuO_{0.67}$ was again found in preference to Cu_2O. The authors concluded that at lower temperatures the system does not reach oxygen chemisorption equilibrium due to an electron deficiency; rapid field transport of copper ions through vacancies keeps the surface concentration of oxygen low thus favouring the formation of $CuO_{0.67}$.

Up until the mid-1990s only measurement of the optical band gap of a sample enabled scientists to distinguish between Cu_2O and Cu_3O_2. A second method was found using UV-Visible-NIR diffuse reflectance spectrometry, Cu_2O can be easily characterised by bands in the range 450 – 650 nm, whilst Cu_3O_2 may be identified by its intense photoluminescence emission at 760 nm [22].

Despite what has been presented in the literature, the formation of $CuO_{0.67}$ or Cu_3O_2 during the oxidation of copper, is an area which not all scientists appear to agree on. Even in thin film experiments the potential presence of Cu_3O_2 has often been ignored, for example in work by Li *et al.*[25] on the oxidation of Cu and Cu-alloy thin films in air. The authors state that copper thin films (800 Å) are rapidly oxidised to Cu_2O when heated to 200 °C in air and then to CuO at the surface at 300 °C. O'Reilly *et al.*[26] investigated the oxidation of bulk and thin film (800 – 5000 Å) copper, X-ray diffraction was used to monitor the surfaces. In both these papers no mention was made regarding the presence or absence of Cu_3O_2 during oxidation.

In work on the low temperature oxidation of bulk copper performed before the 1990s only Neumeister and Jaenicke [27] mention the formation of Cu_3O_2. In 1995, Lenglet *et al.*[28] monitored the oxidation of bulk copper to CuO using a range of techniques including XRD, UV-Vis-NIR diffuse reflectance spectroscopy and XPS and concluded that Cu_3O_2 was indeed part of the bulk oxidation process. Despite this, as recently as 2001 [29] papers concerning the oxidation of copper have been released which make no suggestion of the formation of Cu_3O_2, referring only to CuO and Cu_2O. Other groups such as Zhou *et al.*[30] make reference to the possibility but admit they are unable to factor it into their supporting calculations as the optical constants for this phase are unknown and, as such, they rely largely on visual stimuli (red for Cu_2O and black for CuO) for information. Another example of changing opinions can be seen in work reported by the Cocke group. In their original paper researching copper oxidation with pulsed field desorption mass spectrometry [31] there is mention only of CuO and CuO_2 layers. As the group's understanding has broadened they have reviewed the data presented in this paper and re-assigned some of the features seen to the presence of Cu_3O_2 [32].

In fact Cocke *et al.* have, in recent years, pushed strongly for other scientists to acknowledge the presence of Cu_3O_2 in the low temperature oxidation of copper. Linear sweep voltammetry (LSV) had previously been used by two other groups [33, 34] to slowly strip the oxide layers present on the surface of a treated copper sample. LSV has the benefit of being able to detect compounds which may be present in only very small quantities and are difficult to detect with other more common techniques. In the previous work the authors mention the presence of another form of copper oxide, but no peaks were assigned. However, the presence of a precursor oxide containing both Cu(0) and Cu(I) was suggested in both these reports. Upon deconvolution of the LSV peak obtained by the Cocke group the presence of Cu_3O_2 was confirmed [35, 36]. In a second paper the authors show evidence to suggest the possibility of copper oxide decomposition at the metal-oxide interface which occurs at higher temperature oxidation. This decomposition is also noted by its correlation to an absence of the precursor copper oxide in the LSV data [37]. From this data a schematic was suggested for the low temperature oxidation of copper around atmospheric pressures which is shown in figure 4.3. In an effort to further support this model the group attempted some XPS sputter depth profiling [38]. The results, however, were inconclusive. This was attributed to the phenomenon of sputter reduction, where the sputtering process used to investigate within the film itself, causes the reduction of Cu^{2+} to Cu^{+}, thus obscuring any results. With this fact recognized the authors were unable to add to their previous findings.

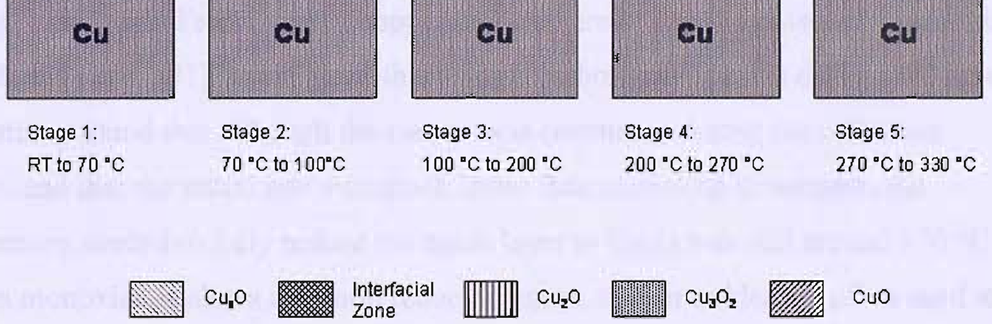

Figure 4.3 – Complex oxide layer structures formed during low temperature oxidation of copper around atmospheric pressure developed from reference 24

4.1.3 Reduction of Copper Oxides

There are many ways in which the reduction of copper oxides has been achieved, with no mention of Cu_3O_2 in most reports. As suggested from the Pourbaix diagram, in figure 4.1, vacuum annealing is the simplest way to reduce a copper oxide layer. In a paper by Li *et al.*[2] the authors state that the reduction of a thin film of CuO to Cu_2O begins at 350 °C and that the phase transition is completed by 610 °C. For a bulk copper sample the transformation is found to be completed at the slightly higher temperature of 680 °C. The reduction does not reach conclusion if the thin film sample is kept at 350 °C *in vacuo* as there was still evidence of both CuO and Cu_2O after 12 hours. During their reduction experiments the authors did find another copper oxide structure other than the cuprite and tenorite structures. This phase Cu_4O_3 (paramelaconite) was first reported by O'Keeffe and Bovir [39] in the late seventies. However, in the reduction experiments it was only obtained via sputtering a CuO film and therefore would not be expected during regular reduction processes. Further thermal reduction work has been performed by Kirsch and Ekerdt[40], by monitoring the surface of thin Cu films (20 Å) which have been oxidised to CuO using XPS and TPD. The authors noted that CuO films were stable, in their carefully controlled C-free environment, up to 500 °C, reduction to Cu_2O had begun by 600 and was complete by 700 °C. Continuing to higher temperatures the authors concluded that the Cu_2O layer was stable up to 800 °C. The higher stability obtained in these experiments was attributed to the quality of the C-free environment used.

Aside from thermal reduction of copper oxides there is also the potential of chemical reduction. Li *et al.*[41] investigated this using a carbon 'cap' on top of the CuO layer. The authors found that although the carbon was consumed during the reduction process and that the initial rate was much faster than annealing in vacuum, the temperature needed to fully reduce the oxide layer to Cu_2O was still around 750 °C. Carbon monoxide is also a common reducing agent, copper oxides are often used to catalyse the oxidation of CO, leading to a number of studies in the literature. Work by Nagase *et al.*[42] using 5 % CO/He shows that CuO is more easily reduced in the presence of CO than Cu_2O, reacting at 100 and 200 °C, respectively. Another interesting result from this paper concerns the reoxidation of the reduced copper surfaces the difference in surface species suggest that copper surfaces and their oxides retain a "history" which suggests the copper sample may need to be fully cleaned between experiments.

More recently Wang *et al.*[43] monitored the reduction reaction using TPR and XRD. The authors reported that CuO reduction started to occur around 200 °C and by 236 °C, only Cu was detectable by XRD. CO_2 production was found to reach a maximum around this temperature, however, CO_2 was still detectable up to 585 °C.

During isothermal results it was consistently found that CuO reduced much more rapidly than Cu_2O regardless of the temperature used, which agrees with the vacuum annealing results. These results were obtained under a strong flow of 5 % CO/He. However, when investigating the reduction under a very limited flow of the same gas at 224 °C the change from CuO – Cu_2O – Cu was observed by XRD.

Hydrogen gas has also been used to reduce copper oxide layers, Hu *et al.*[29] concluded from their experiments that the reduction of the copper oxide proceeded from the metal oxide interface, which adds weight to the copper oxide decomposition idea mentioned earlier and proposed by Cocke *et al.*[37] The authors also found, using sheet resistance measurements on thin copper oxide films., that under 10 % H_2/Ar, reduction at 400 °C was almost instantaneous whilst still fairly rapid (< 60 s) at 230 °C. Further work in the area by Kim *et al.*[44] found a similar situation to that of CO reduction. Under excess reducing agent the reduction occurs directly from CuO to Cu, however, when the supply is limited, reduction by H_2 proceeds from CuO to Cu via the Cu_2O intermediate. Their results agreed with other reduction methods that Cu_2O is harder to reduce than CuO.

The final methods of reduction worth taking note of were presented by Kirsch and Ekardt [40]. Along with their thermal reduction work mentioned earlier, the authors also investigated the use of radical species for reduction, in the form of D· and CH_3·. Reduction with deuterium radicals was found to be very successful even at low pressures, reducing Cu_2O below 150 °C, whereas exposure to D_2 at similar temperature and pressure produced negligible reduction. Experiments on thin films of CuO once again agreed with previous findings that it is easier to reduce than Cu_2O. Similar findings were reported for the methyl radical species.

A number of reports suggest Cu_4O_3 as a potential intermediate between CuO and Cu_2O. However no evidence of its existence in the reduction process has been found. This is not unsurprising, due to the large differences in the position of oxygen atoms between paramelaconite and cuprite structures.

4.1.4 Vibrational Spectroscopic Determination of Copper Oxides

For vibrational spectroscopy the symmetry of the unit cell provides very useful information. From it, it can be possible to conclude which vibrational modes are present and which are active in different forms of vibrational spectroscopy (i.e. IR or Raman active). The unit cell of Cu_2O can be thought of as a body centred cubic lattice of oxygen. The central oxygen atom is then surrounded by four Cu atoms in a tetrahedron at approximately (¼, ¼, ¼), (¾, ¾, ¼), (¼,¾,¾) and (¾,¼,¾). Cuprite belongs to the O_h^4 (Pn3m) space group [45]. The unit cell of CuO can be considered a body centred monoclinic lattice (β = 99.54°) of copper containing four oxygen ions at approximately (¼, ¼, ¼), (¼, ¼, ¾), (¾, ¾, ¼) and (¾, ¾, ¾). Tenorite can be considered as part of the C2/c-C_{2h}^6 space group [46]. The two oxide structures are shown in figure 4.4 where the closest left hand corner is designated as (0, 0, 0).

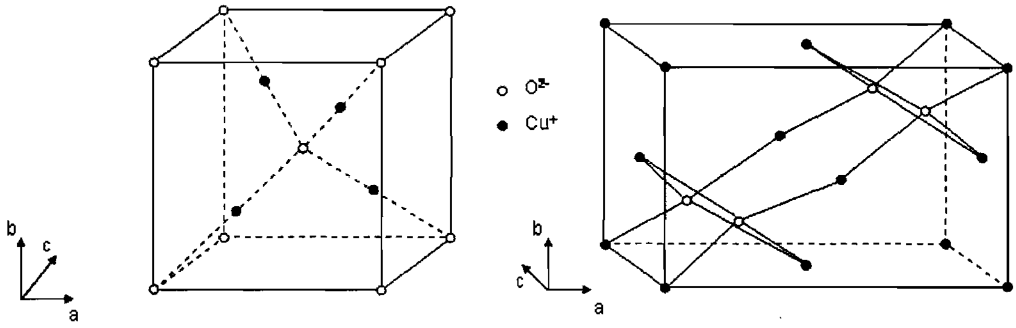

Figure 4.4 – Unit cell of cuprite (Cu_2O) [45] and tenorite (CuO) [46]

By placing displacement vectors upon the atoms and examining their transformation properties under the group it is possible to see which vibrational modes are present due to certain atoms. For Cu_2O, Cu motions give rise to $2F_{1u} + F_{2u} + E_{2u} + B_u$ and the O motions to $F_{1u} + F_{2g}$ vibrational modes [47]. Of these the F_{2g} mode is expected to be Raman active and two of the F_{1u} modes are expected to be IR active, all three modes are shown in figure 4.5. In a perfect lattice the other vibrations are silent, however, cuprite has been found to be nonstoichiometric and this can lead to a breakdown of the selection rules allowing other vibrations to be detected [48].

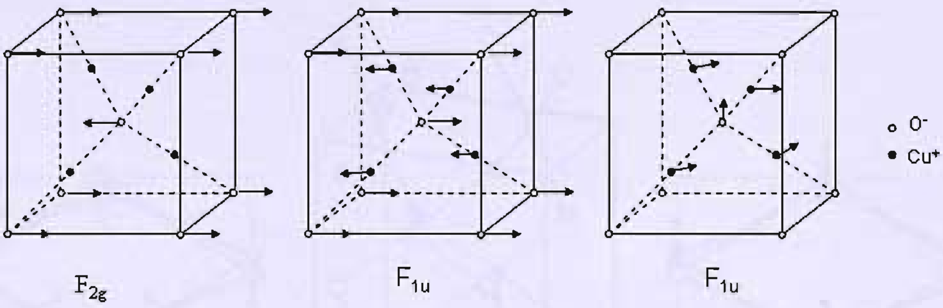

Figure 4.5 – One Raman and two IR active vibrations of Cu_2O [48]

Tenorite can also be analysed in this manner, motion of the Cu atoms give rise to 3 A_u and 3 B_u vibrations and motion of the O atoms gives rise to A_g, 2 B_g, A_u and 2 B_u modes. Of these one A_u and two B_u modes are acoustic modes, leaving three Raman active modes (A_g and two B_g) and six IR active modes (three A_u and three B_u). These nine modes are shown in figures 4.6 and 4.7 [49]. To help visualise the vibrational modes, two structural views are required. These are different to the unit cell shown in figure 4.3 in orientation only, the structure itself is identical.

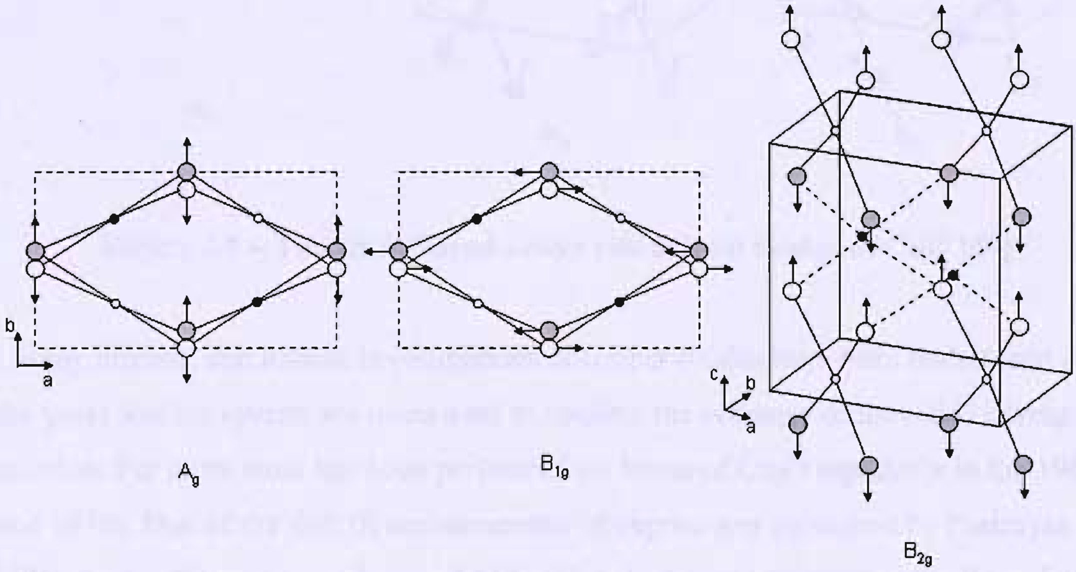

Figure 4.6 – The three Raman active vibrational modes of CuO [49]

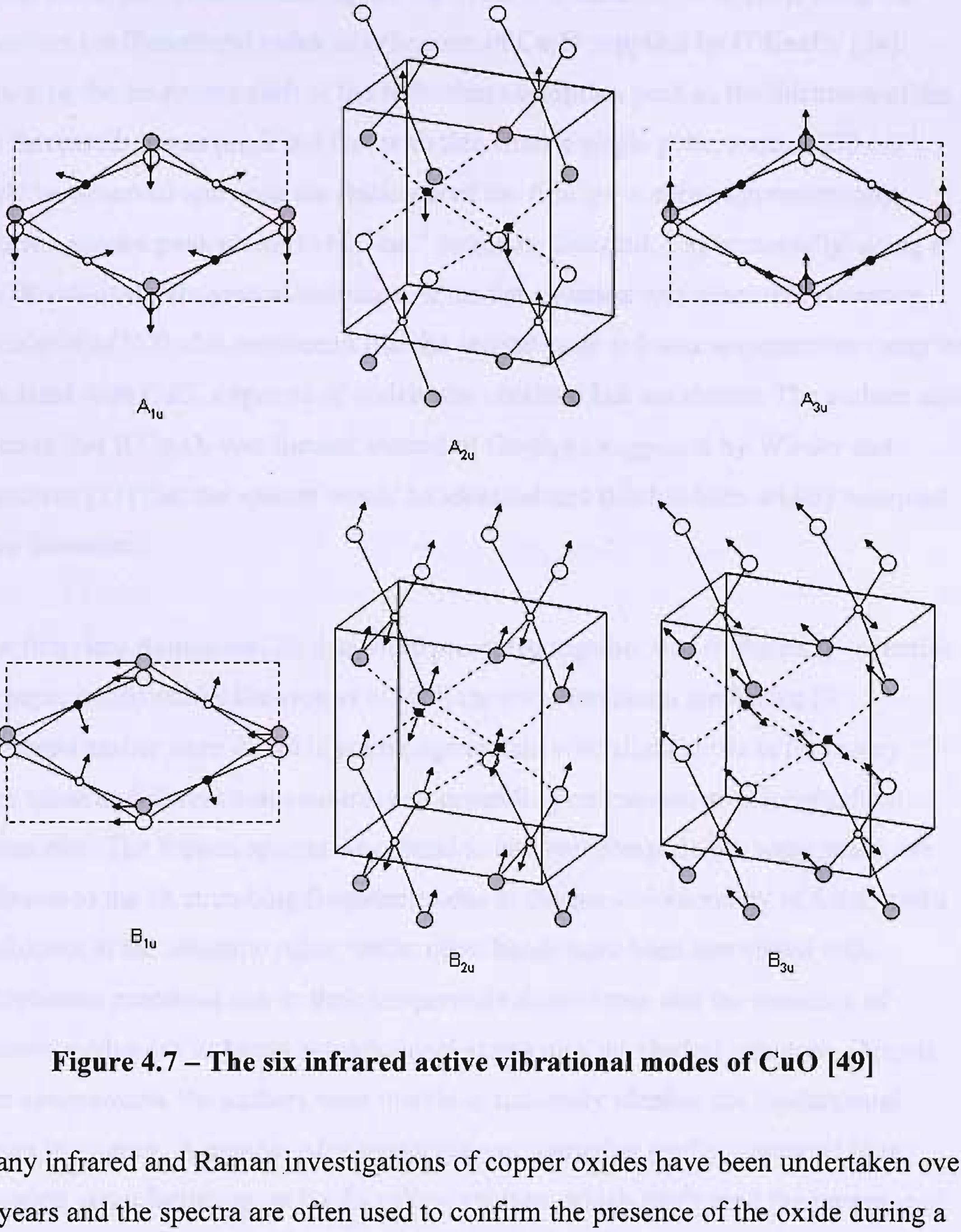

Figure 4.7 – The six infrared active vibrational modes of CuO [49]

Many infrared and Raman investigations of copper oxides have been undertaken over the years and the spectra are often used to confirm the presence of the oxide during a reaction. Far more work has been performed on forms of Cu_2O especially in the 1960s and 1970s. One of the first IR measurements of cuprite was published by Pastrnyak [50]; one band was observed around 600 cm^{-1}, which was attributed to the first of the F_{1u} vibrational modes shown in figure 4.5. The second of the IR active vibrational modes was detected around 150 cm^{-1} a few years later by Bouster *et al.*[51]. These values were found to be in reasonable agreement with the calculations of Helmetes [52], who used classical dispersion theory as well as those from Carabatos [47] performed using rigid ion lattice dynamics concerning the long wave limit.

In the initial papers documenting the use of RAIRS Greenler *et al.*[53], using the extinction coefficient and index of refraction of Cu_2O supplied by O'Keeffe [54], calculated the frequency shift of the reflection absorption peak as the thickness of the film increased. It was predicted that with thin films a single peak, around 650 cm^{-1}, would be observed and once the thickness of the film grew above approximately 4200 Å a second peak closer to 600 cm^{-1} would be detected. Experimentally, using a mid-IR reflection absorption technique, a similar situation was observed. However, Greenler *et al.*[53] also mentioned that the second peak at lower wavenumbers may be associated with CuO, a spectra of which was obtained but not shown. The authors also assumed that if Cu_3O_2 was formed instead of Cu_2O, as suggested by Wieder and Czanderna [21] that the spectra would be identical and this has been widely accepted in the literature.

The first time Raman and IR data were presented together was in the early seventies in a paper published by Dawson *et al.*[48], the two vibrational modes for IR mentioned earlier were found in strong agreement, with slight shifts in frequency when taken at different temperatures and depending on transverse or longitudinal frequencies. The Raman spectra was found to be more complicated; some peaks are attributed to the IR stretching frequencies due to the nonstoichiometry of Cu_2O and a breakdown in the selection rules, whilst other bands have been associated with multiphonon processes due to their temperature dependence and the presence of resonant modes due to heavy substitutional atoms on a tetrahedral structure. Despite these assignments, the authors were unable to rationally identify the fundamental Raman frequency. A number of resonant Raman scattering studies appeared in the following years focussing on the 1s yellow exciton, which confirmed the presence of many muliphonon bands [55-58]. The Raman peak for Cu_2O has now been categorically assigned to a peak around 530 cm^{-1} by Chan *et al*, who also detected both IR stretches [59].

Aside from a very brief mention in one of the cornerstone papers for reflection absorption spectroscopy by Greenler *et al.*[53] infrared work on CuO did not appear until comparatively much later. One of the earliest examples was provided by Tevault *et al.*[60] and involved the reaction of copper and ozone molecules in an argon matrix and monitored with mid-IR. CuO was formed and a peak around 630 cm^{-1} was assigned to it. The authors also gave details of the effects of isotopic substitution. By the end of the 1980s a few more papers had been released, however rather than being solely concerned with CuO, many were comparing the oxide form to high temperature superconductors, for example in the mid-IR [61] and far-IR [5]. Around this time the three expected Raman peaks were observed and assigned by Chrzanowski and Irwin [62] who used polarization techniques, with a fourth band assigned to two phonon scattering. The three main peaks were found to sharpen upon cooling as well as an additional band forming below the Néel temperature of 200 K. A year later Hagemann *et al.*[63] confirmed many of the findings for the Raman spectra and were the first to show the far-IR spectrum in comparison. However this data suffered with poor signal-to-noise below 350 cm^{-1}. In 1990 a very detailed paper was published by Kliche and Popovic [49] covering the far-IR spectrum of polycrystalline pressed samples of CuO. At room temperature the group observed six vibrational modes between 100 and 600 cm^{-1}. As the temperature was lowered some of the bands were found to shift and sharpen, especially below the Néel temperature. The authors used their knowledge of the structure of PdO, of which CuO is a twisted derivative, to help assign many of the bands to specific vibrational modes for the first time. Subsequently, using polarized infrared reflectance Guha *et al.*[64] confirmed many of these assignments at room temperature. Lower temperature polarization measurements were also published by Homes *et al.*[65]. Coordinate analysis enabled Narang *et al.*[66] to calculate the Raman and infrared vibrational modes for CuO and compare them with obtained spectra from a paraffin mull of the polycrystalline sample.

The first time far-IR experiments were used to differentiate between the two oxide phases during the oxidation of copper was around 1995, with the release of two papers, one published by Lenglet *et al.*[28] and the other by Lefez *et al.*[67], the published results are compared alongside other experiments in tables 4.1 and 4.2

By the end of the 1990s the bands in the far-IR attributed to CuO and Cu_2O were widely accepted and more often used in confirming results of experiments. In, for example, laser ablation of copper atoms and dioxygen in an argon matrix [68], as well as experiments of CO oxidation over a copper oxide surface [42], for both experiments the peaks found using mid-IR were fairly consistent with those in the literature. A lot of work around this period also concerned solution based measurements during electrochemical oxidation of copper. This introduces the possibility of observing hydroxide species on the surface of the oxide and both far-IR [69] and Raman [59, 70, 71] were used successfully in this area.

A change in the understanding of the structure of CuO came in 2001, when Kuz'menko *et al.*[46] released results which showed the presence of the six major peaks in the far-IR but also of many minor bands. These minor bands were attributed to the fact that the space group is probably of lower symmetry than had previously been reported, but the authors concluded that the assigned space group, $C2/c\text{-}C_{2h}^{6}$, is still a reasonable representation.

Tables 4.1 and 4.2 present an overview of the stretching frequencies observed using Raman and IR spectroscopy in the literature for different forms of copper oxide. From these tables it can be seen that as techniques have improved the correlation between results has become much greater. It can be concluded from these tables that within the region of interest for this thesis, 200 – 700 cm^{-1}, one peak for Cu_2O should be observed around 640 cm^{-1} (F_{1u}) and four or five peaks for CuO around 330 cm^{-1} (A_{2u}), 420 cm^{-1} (A_{3u}), 480 cm^{-1} (B_{2u}), 530 cm^{-1} (B_{3u}) and a peak occasionally observed but unassigned or assigned to the B_{3u} mode appearing around 600 cm^{-1}. However, there is a large variation in the band positions reported by different groups.

Sample	Technique	Frequency / cm^{-1}	Reference
Thin film	Transmission	433/483/526/609/661/695/791	[54]
Thin film	Reflectance	146/613	[52]
Calculation	Infrared	(TO) 146/611 (LO) 161/642	[47]
Calculation	Raman	98.6/110	[45]
Thin film	Reflectance	(TO) 146/609 (LO) 149/638	[48]
Thin film	Raman	100/110/300/515	[48]
Single crystal	Resonance Raman	86/109/153/218	[58]
Thin film	Resonance Raman	86/109/153/350/515/640/680	[55]
Thin film	Reflectance	640	[28]
Thin film	Reflectance	(TO) 610 (LO) 650	[67]
Anodic film	Synchrotron Far-IR	630/790/1110	[69]
Pressed powder	Transmission	631	[42]
Anodic film	Surface Enhanced Raman	150/528/623	[59]
Nanocrystalline film	Transmittance	617	[73]
Anodic film	Transmittance	620	[72]

Table 4.1 – Vibrational frequencies from the literature for Cu_2O

Sample	Technique	Frequency / cm^{-1}	Reference
Copper and ozone in Ar matrix	Transmission	630	[60]
Pressed powder	Transmission	484/534/582	[61]
Pressed powder	Reflectance	148/165/323/446/481/598	[5]
Pressed powder	Raman	133/217/305/350/635	[5]
Pressed powder	Raman	218/303/350/465/635	[62]
Single crystal	Raman	297/344/629	[63]
Pressed powder	Transmission	452/483/542/583	[63]
Pressed powder	Reflectance	147/161/321/478/533/587	[49]
Single crystal	Raman	296/346/636	[64]
Single crystal	Reflectance	146/164/355/480/542/603	[64]
Paraffin mull	Absorption	147/163/324/444/515/586	[66]
Calculation	Infrared	140/164/327/438/515/590	[66]
Thin film	Reflectance	445/485/555/605/611	[28]
Thin film	Reflectance	(TO) 480/530 (LO) 580	[67]
Single crystal	Reflectance	148/167/324/450/516/566	[65]
Anodic film	Synchrotron Far-IR	160/524/551	[69]
Pressed powder	Transmission	540	[42]
Single crystal	Reflectance	145/161/322/409/470/523	[46]
Nanocrystalline film	Transmittance	416/441/453/513/568	[73]
Anodic film	Transmittance	531/592	[72]

Table 4.2 – Vibrational frequencies from the literature for CuO

In this chapter the development of a new High Pressure Reaction Cell (HPRC) for far-IR RAIRS is discussed. Installed within a UHV chamber, this new cell allows samples to be cleaned and characterised under ultra high vacuum conditions. The samples are then trapped within the HPRC and can be exposed to more realistic pressures of gas. RAIRS experiments can then be performed and, if desired, the sample can be removed from the cell and re-examined using the techniques available in the UHV chamber. The data presented for the oxidation of a copper surface shows excellent agreement with the literature and are also supported by density functional theory calculations. The possibility of investigating the reduction of the oxide layer using carbon monoxide within the HPRC is also discussed.

4.2 Development of the High Pressure Reaction Cell

4.2.1 The Original Design

The High Pressure Reaction Cell (HPRC) is located on beamline 13.3 at Daresbury laboratory, a permanent end station specifically for RAIRS experiments. During the original design process of the HPRC a number of factors needed to be considered:

1. An optical path which also included a reflection off the sample
2. A vacuum seal capable of withstanding 1 atm gas pressure
3. A separate lid and goblet, to allow other techniques to be performed on the sample
4. The ability to store the goblet so it does not interfere with other UHV experiments performed on the beamline

In order to meet these requirements the HPRC was designed as a three part system; a landing stage, a goblet and a lid which was attached to an x, y, z, θ manipulator.

The landing stage is situated at the base of the UHV chamber well below the RAIRS experiment level. The stage is a 'U' shape so that a gas feed pipe passes through the stage into the bottom of the goblet. On each one of the longer sides of the landing stage there is a locking pintle, this ensures that the goblet can be securely fixed when disengaging the lid from the goblet.

The goblet, shown in figure 4.7, is an aluminium vessel comprising of two windows, a base flange and an entrance hole for the lid section. The vessel has two locking slots, situated near the base flange, used for securing the goblet to the landing stage. Also present, but not shown in this diagram, are four locking pintles, situated near the lid entrance, used for securing the lid to the goblet, these will be discussed in more detail later. Gas is introduced into the goblet via the base flange which is connected to a coiled, thin bore metal tube (not shown), the other end of which attaches to the gas line system shown in figure 4.14. The form of the metal tubing was chosen in order to ensure both minimal strain on the tubing as the goblet is manipulated, as well as reducing any tension on the manipulator that may be caused by inflexible piping.

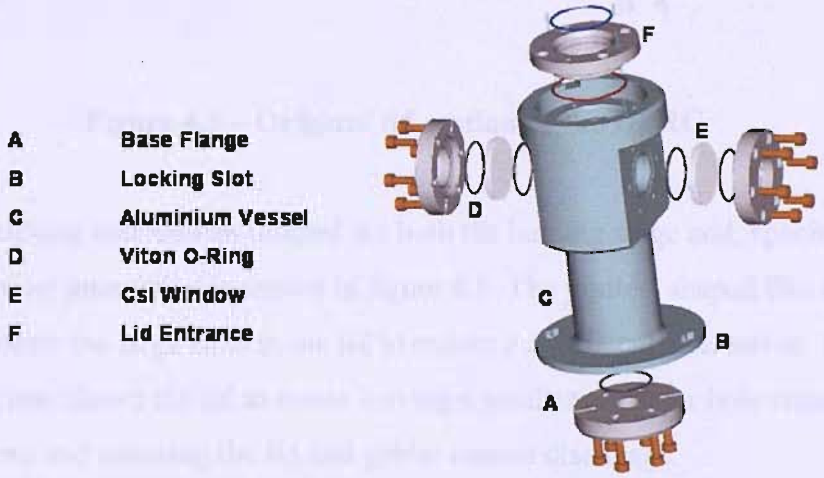

Figure 4.7 – Original design of the goblet section of the HPRC

The caesium iodide windows present in the vessel allow the infrared light to enter the goblet and reflect off the sample at grazing incidences. The viton O-ring seals enable a high pressure to be contained with the HPRC, without compromising the vacuum of the UHV chamber. The entrance hole also uses a trapped O-ring system to maintain a good pressure once the lid has been engaged with the goblet.

The original lid design is shown in figure 4.8, comprising of a main section attached directly to the manipulator and a bonnet with electrical feedthroughs. The two pieces are attached using spring mounted screws, this arrangement minimises any torque applied to the goblet from the coiled gas tubing. Two of the mounting pins were used to hold the sample in place, whilst the other two held and supplied power to a filament, used to heat the sample.

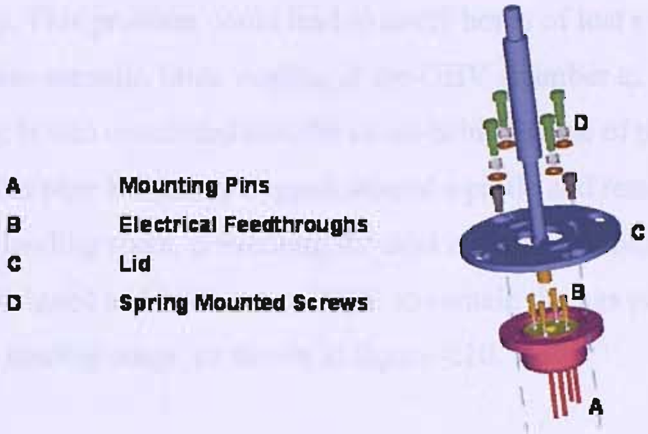

Figure 4.8 – Original lid section of the HPRC

The pintle locking mechanism utilised for both the landing stage and, specifically, the lid and goblet interaction is shown in figure 4.9. The pintles, shaped like arrow heads, help locate the large slots in the lid to ensure a consistent interaction. The shaft of the arrow then allows the lid to rotate leaving a smaller diameter hole situated behind the head and ensuring the lid and goblet cannot disengage.

Figure 4.9 – The pintle locking system of the lid and goblet

4.2.2 The Second Stage of Development

Whilst the original design of the HPRC managed to fulfil the four aims mentioned in section 4.2.1 a number of problems became apparent in the primary testing period.

One of the major issues faced involved the regular manipulation of the goblet, due to limited visibility it was found to be very difficult to consistently raise and land the goblet successfully. This problem could lead to many hours of lost experimental time and in the worst case scenario force venting of the UHV chamber to alleviate the situation manually. It was concluded that the cause behind some of the difficulties was a coil of the gas inlet pipe becoming trapped around a pintle and remaining between the goblet and the landing stage, preventing the docking of the goblet. To prevent this, a nose cone was designed and built out of PTFE to contain the gas pipe and help guide the goblet into the landing stage, as shown in figure 4.10.

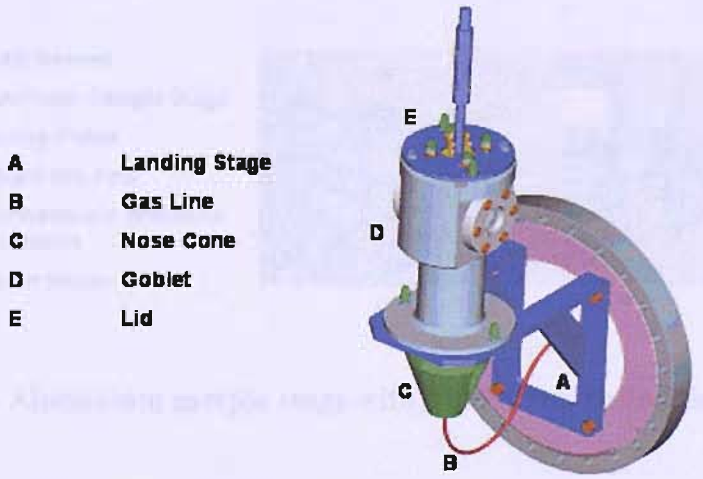

Figure 4.10 – Landed HPRC with the additional nose cone

Two further developments were made to minimise control issues with the HPRC. Firstly a pointer was installed within one of the view ports of the UHV chamber and a marker machined into the body of the goblet. When these two features are in line it confirms that the orientation of the goblet is in line with the locking pins on the landing stage. A change was also made to the UHV chamber itself, two new view ports were installed one on each side of the chamber in line with the landing stage allowing a clear view of each one of the pintles. These three changes ensured that the coupling, unlocking of the goblet, locking of the lid and raising of the goblet followed by the opposite procedure during landing, could be performed smoothly and efficiently time and again, with no complication.

Another issue that arose during the original testing of the HPRC occurred whilst heating the crystal. In the original design the sample was heated using a filament situated behind the crystal. Tungsten filaments are very useful for heating samples in UHV, however in higher pressures of oxygen the tungsten oxidises rapidly and the filament breaks down. To avoid this problem the sample had to be heated in the HPRC under vacuum and the filament switched off before the oxygen could be introduced to the cell. In order to remove this need, a new sample stage was designed to attach to the bonnet that had already been designed for the HPRC. Shown in figure 4.11 the new stage was made of aluminium and incorporated an oxygen tolerant button heater and the temperature monitored using a thermocouple.

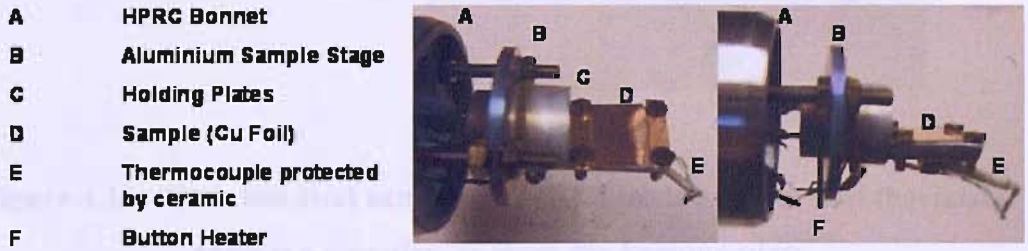

Figure 4.11 – Aluminium sample stage with button heater and thermocouple

To test the new sample stage, a polycrystalline Cu foil sample was used. This provided the security of not having to worry about damaging a more expensive single crystal, and allowing the oxidation process to be taken further as the sample was easily replaceable. During experimentation it was found that the temperature reading was unreliable, once the button heater was activated the temperature would go down before eventually increasing again. This was attributed to the thermocouple junctions to the electrical feedthroughs being situated directly above the button heater. As the button heater warmed up the connections above the heater would also warm, before the bulk of the aluminium and sample would have, this would make the sample appear to cool in comparison to the temperature external to the UHV chamber. A preliminary experiment was still performed and it was found on removal from the UHV chamber that under the highly oxidising conditions the copper film had reacted with the aluminium sample stage. Due to these issues a second sample stage was designed and constructed. Made from stainless steel it incorporated the button heater but also used a Pt resistance thermometer, situated behind the crystal, to monitor the sample temperature; the new sample stage is shown in figure 4.12.

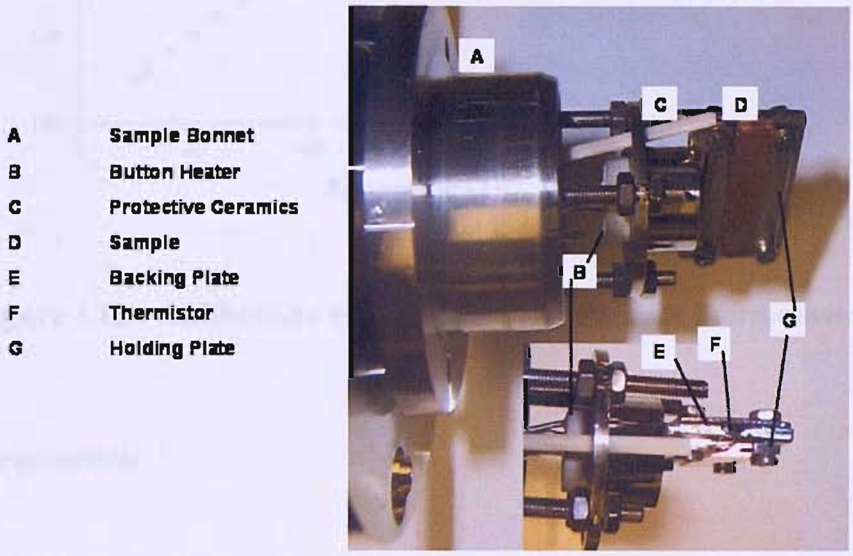

Figure 4.12 – Stainless steel sample stage with button heater and thermistor Inset is a side view to show the backing plate

The resistance of a Pt resistance thermometer increases with temperature. In order for this to be directly useful in an experiment the response of the thermistor needs to be calibrated. This was achieved by using the manipulator outside of the UHV chamber with the temperature being monitored separately by a thermocouple attached directly to the crystal, during heating and cooling of the sample. The resistance and temperature measurements could then be correlated for future reference, this relationship is shown in figure 4.13.

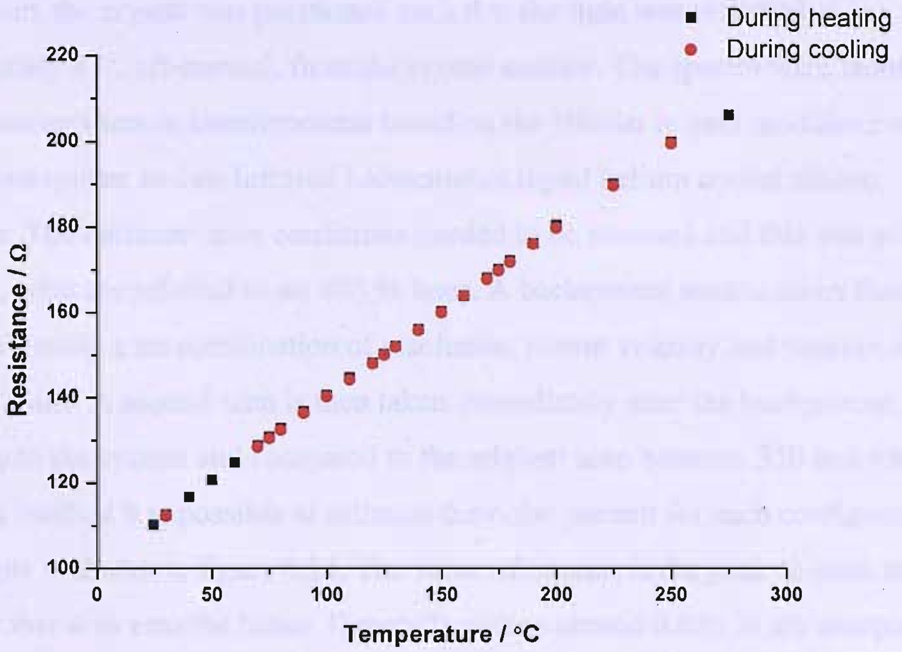

Figure 4.13 – Calibration of the platinum resistance thermometer

4.3 Experimental

The far-IR experimental results presented in this chapter were obtained using beamline 13.3 at Daresbury laboratory. A diagram of the UHV chamber used can be found in figure 2.13 in Chapter 2 of this thesis.

The UHV chamber obtained a base pressure of 1 x 10^{-10} mbar, following a bakeout and was evacuated with a diffusion pump. The chamber was equipped with LEED (low energy electron diffraction), XPS (X-ray photoelectron diffraction) and RAIRS (reflection absorption infrared spectroscopy). The chamber was also fitted with a QMS (quadrupole mass spectrometer) and an ion gun.

The Cu(100) crystal (20 x 4 x 1 mm) was mounted upon a specially designed manipulator and could be heated using an oxygen tolerant ceramic button heater, as described above. The temperature was monitored using a platinum resistance thermometer. The crystal was cleaned by repeated cycles of 500 eV Ar^+ sputtering and annealing to 650 K.

Once clean, the crystal was positioned such that the light was reflected at approximately 87°, off-normal, from the crystal surface. The spectra were recorded using a custom vacuum interferometer based on the Nicolet impact modulator with a silicon beamsplitter and an Infrared Laboratories liquid helium cooled silicon bolometer. The optimum scan conditions needed to be assessed and this was achieved by taking, what are referred to as, 100 % lines. A background scan is taken from 200 to 700 cm^{-1} using a set combination of resolution, mirror velocity and number of co-added scans. A second scan is then taken immediately after the background, with no change to the system and compared to the original scan between 350 and 450 cm^{-1}. Using this method it is possible to estimate the noise present for each configuration. An example is shown in figure 4.14. The value of interest is the peak-to-peak ratio and the closer this is to zero the better. Generally values around 0.030 % are acceptable values as low as 0.005 % were obtained under optimal conditions.

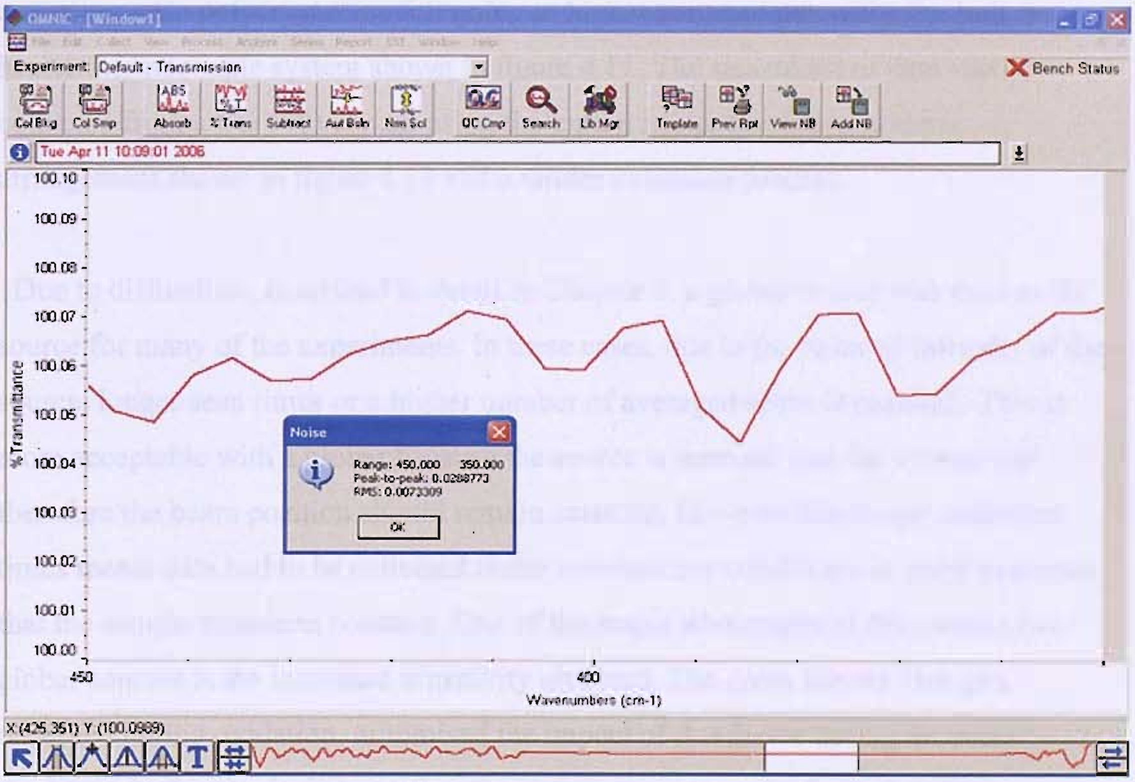

Range: 450.000 350.000
Peak-to-peak: 0.0288773
RMS: 0.0073309

Figure 4.14 – Peak to peak noise ratio of a 100 % line scan

As mentioned in Chapter 2.3 the work in this thesis was performed at the SRS at Daresbury laboratory. The benefits of using a synchrotron light source mean that much shorter experiment times are possible. In fact, when using synchrotron light as the source for these experiments it was found that a higher number of averaged scans led to a higher peak-to-peak noise ratio. At first glance this seems counter-intuitive as taking a higher number scans of the same surface should increase the real peaks and decrease the peaks that appear randomly due to noise. This is indeed the case with a fixed source, however synchrotron light does not always remain fixed. In fact there is a period of time after injection when the beam is settling, where the position of greatest intensity will shift. This means a smaller number of co-added scans and by extension a shorter experiment time is more suitable when using synchrotron radiation. This problem also explains why a background scan cannot be associated with a sample scan taken from a different fill of the synchrotron ring. When using synchrotron radiation as the light source, scans on beamline 13.3 are generally performed with a resolution of 8 cm^{-1}, a mirror velocity of 3.16 cm s^{-1} and 256 co-added scans. Two sets of experiments were performed using synchrotron radiation, one using a Cu polycrystalline foil going to higher temperatures using the button heater/thermocouple system shown in figure 4.11. The second set of data was collected from a Cu(100) crystal using the button heater/thermistor sample arrangement shown in figure 4.12 and a milder oxidation process.

Due to difficulties, described in detail in Chapter 6, a globar source was used as the source for many of the experiments. In these cases, due to the reduced intensity of the source, longer scan times or a higher number of averaged scans is required. This is more acceptable with a globar because the source is screwed into the system and therefore the beam position should remain constant. However the longer collection times meant data had to be collected under non-reactive conditions in order to ensure that the sample remained constant. One of the major advantages of SR sources over globar sources is the increased sensitivity obtained. The gross feature changes, observed during oxidation, minimised the impact of this factor during the work presented in this thesis. When using the globar, scans were performed with a resolution of 8 cm^{-1}, a mirror velocity of 1.89 cm s^{-1} and 5120 co-added scans. One set of data was collected using the glowbar source, the button heater/thermistor arrangement was used over 200-700 cm^{-1} and mild oxidation conditions were used.

With a clean crystal and optimum collection setup obtained, the crystal was then lowered into the goblet. Rotation of the lid caused the lid to lock, further rotation then proceeded to unlock the goblet from the sample stage, the completed HPRC could then be raised to the RAIRS level. During preliminary testing of the HPRC it was found that in order to minimise the inherent noise in the system all scans must be performed in the presence of the same pressure of gas. It was concluded that this is due to the higher gas pressure slightly overcoming the resistance of the spring mounted screws attached to the bonnet of the HPRC lid, shown in figure 4.7, thus altering the position of the crystal. In order to satisfy this criterion the HPRC was filled with 200 mbar of argon when background scans were run. When using the SRS scans could be taken at temperature due to the short collection time. Thus, a set of background lines were taken at a range of temperatures allowing each experimental scan to have a more accurate background file to compare with post experiment. As explained above, this was not possible for data collected with the globar source due to the long collection times, and therefore only one background scan was required.

The HPRC was then evacuated and refilled with 200 mbar of oxygen, the purity of the gas could be monitored via the QMS on the UHV chamber due to a slight leak across the O-ring seals raising the pressure of the UHV chamber to approximately 1×10^{-6} mbar.

The button heater on the sample stage was then activated. Whilst using synchrotron light, scans were taken at a range of temperatures, after each 'at temperature' scan the crystal was allowed to cool to approximately 350 K and a second scan was taken before heating the sample up to the next temperature. With the globar source, the sample was heated to a set temperature and then allowed to cool to approximately 330 K where a scan was run before heating the crystal to a higher temperature.

Once an oxide layer had been achieved the HPRC was evacuated and refilled with 200 mbar Ar in order to confirm that the stability of the oxide layer was not reliant on the atmosphere it was observed under.

With a stable oxide surface it was then possible to attempt a reduction of the surface with carbon monoxide. However with the high pressures of gas used in this experiment there are additional complications of contaminants. Carbon monoxide is kept in stainless steel cylinders and at these high pressures the CO can react with the cylinder to produce trace quantities of nickel and iron carbonyls, which may adsorb on the sample surface. In order to remove this possibility, a copper tubing gas line was constructed which is shown in figure 4.15.

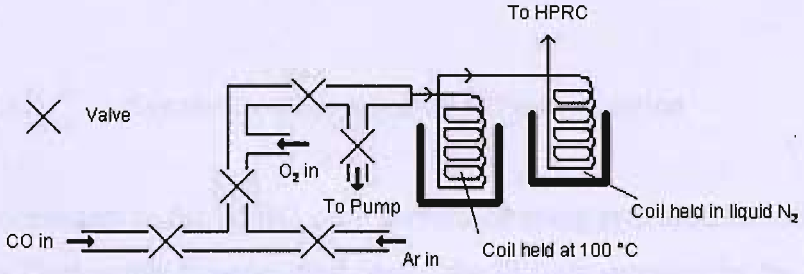

Figure 4.15 – Copper gas line to remove iron and nickel carbonyls

With a background scan of the oxide layer in an atmosphere of Ar, the HPRC was evacuated and then filled with 200 mbar of CO. The same experimental process, as mentioned above, dependent on which source was used, was followed for these experiments. Once again the purity of the gas could be monitored via the QMS, and if any gas products were formed during the attempted reduction they were also detectable.

With the experiments completed the HPRC was lowered to the sample stage, rotation locked the goblet to the sample stage, further rotation unlocked the lid and upon raising was disengaged from the goblet, allowing the manipulator to be removed from the UHV chamber.

4.4 Results and Discussions

4.4.1 Far-IR Study of the Oxidation of Cu(100) at Realistic Pressures

In the following section the IR source and sample type are given as the section headings.

4.4.1.1 Synchrotron Polycrystalline Foil Oxidation

Original experiments in the HPRC were performed using synchrotron radiation as the far-IR source. During this experimental period the IR light supplied by the SRS was found to be unstable. In order to reduce the effect of this on the data the following conditions were used: a resolution of 8 cm^{-1}, a mirror velocity of 5.12 cm s^{-1} and 512 co-added scans. Despite this, the peak-to-peak noise level detectable on a 100 % line was found to be around 0.35 %, which is over ten times the ideal working conditions, this issue is discussed in greater detail in Chapter 6.

The progressive oxidation of a polycrystalline Cu foil exposed to 200 mbar of oxygen is shown in figure 4.16. Scans were taken at specific temperature and compared to a background of the clean sample, obtained in 200 mbar Ar at similar sample temperatures. It can be seen that the baseline of the spectra decreases substantially as the foil is oxidised, this can be attributed to the sample slowly turning black due to CuO formation. As the sample changes colour less light will be reflected and therefore the signal will go down.

From this data it can be concluded that the oxidation of the copper foil occurs between 373 and 423 K with the appearance of a large peak around 637 cm^{-1}. This peak is shown to be characteristic of Cu_2O by reference to the literature [28, 42, 47]. By 493 K this peak has become a shoulder on a larger peak around 580 cm^{-1}.

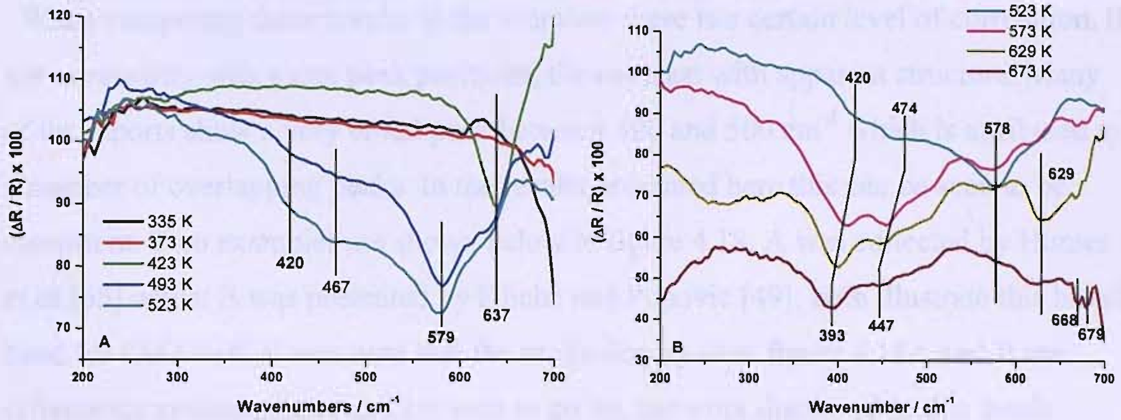

Figure 4.16 – Oxidation of a Cu foil in 200 mbar O_2 using SR far-IR RAIRS, 8 cm^{-1} resolution, 5.12 cm s^{-1} mirror velocity, 512 co-added scans. Light blue spectra are identical for plots A and B

Along with the large peak at 580 cm^{-1}, two shoulders are seen around 420 cm^{-1} and 460 cm^{-1}. As the oxidation proceeds to higher temperatures, shown in figure 4.16B, these two shoulders shift to lower frequency and become more dominant, whilst the peak at 580 cm^{-1} greatly diminishes and the one near 630 cm^{-1} reappears. Upon close inspection of the scans at higher temperature two other peaks appear, as indicated by the dotted lines in figure 4.17. In the higher temperature scans a further two peaks can be seen at high wavenumbers, around 670 cm^{-1}, these will be discussed later in the chapter.

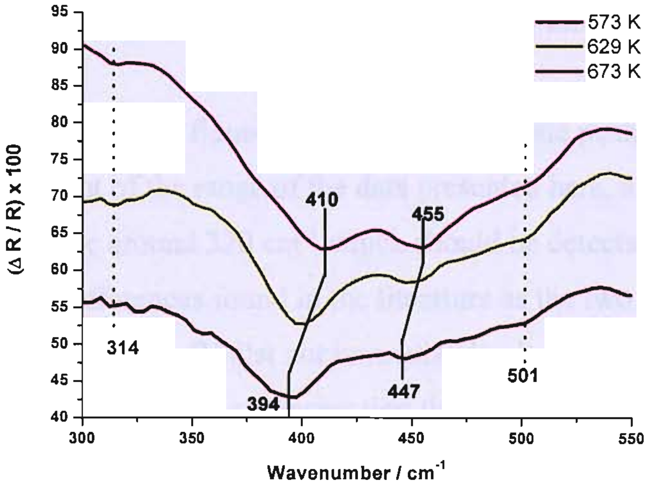

Figure 4.17 – Potential extra peaks in figure 4.16B

When comparing these results to the literature there is a certain level of correlation, if not necessarily with exact peak positions, then at least with apparent structure. Many of the reports show a very broad peak between 400 and 500 cm^{-1} which is attributed to a number of overlapping peaks. In the results presented here this can be seen to be consistent. Two examples are shown below in figure 4.18, A was collected by Homes *et al.*[65] whilst B was presented by Kliche and Popovic [49], both illustrate this broad band for CuO well. Please note that the peaks displayed in figure 4.18A and B are reflectance measurements and are seen to go up, the work displayed in this thesis features peaks which go down, but are equivalent.

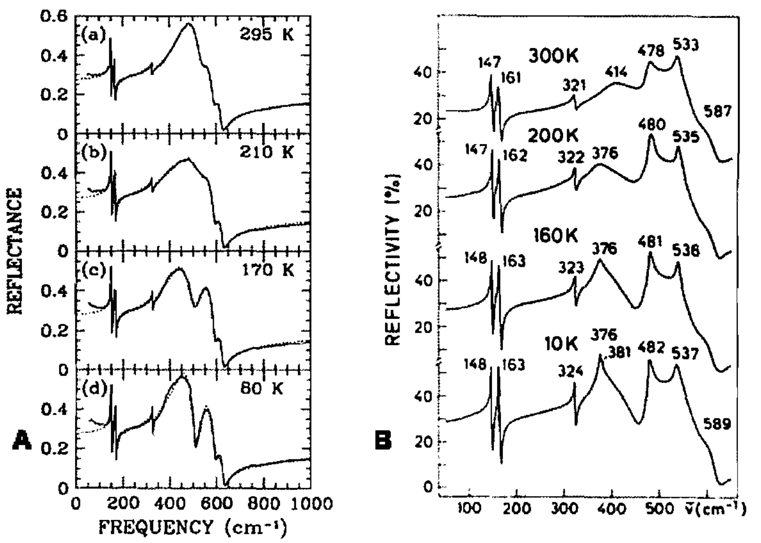

Figure 4.18 – Examples of far-IR reflectance spectra of pressed powders of CuO collected at different temperatures: A [65] and B [49]

Both of the literature spectra in figure 4.18 show two definite peaks below 200 cm^{-1}, which is unfortunately out of the range of the data presented here, although both sets also show a strong feature around 320 cm^{-1} which should be detectable. These two examples illustrate the differences found in the literature as the two peak shapes of the broad feature are quite different. Whilst not immediately clear in the data presented from the HPRC in figure 4.16, on close inspection there may be a slight peak marked at 314 cm^{-1} most notably in the scan at 573 K in figure 4.17, although the noise levels of the data make this assignment unreliable. It is worth noting that many investigations into CuO only measure above 400 cm^{-1}, and would not report this band. However there are also a couple of examples in the literature where the band is not seen at all. For example the IR transmission spectrum shown by Hagemann *et al.*[63] and a reflectance spectra from Guha *et al.*[64] are shown in figure 4.19. Both still have a broad feature dominating the spectra, but neither show the peak reported around 320 cm^{-1}, this absence is not really discussed in the literature. Figure 4.19A involves peaks viewed going down, whereas in figure 4.19B, the peaks are seen to go up, despite this the peaks are equivalent.

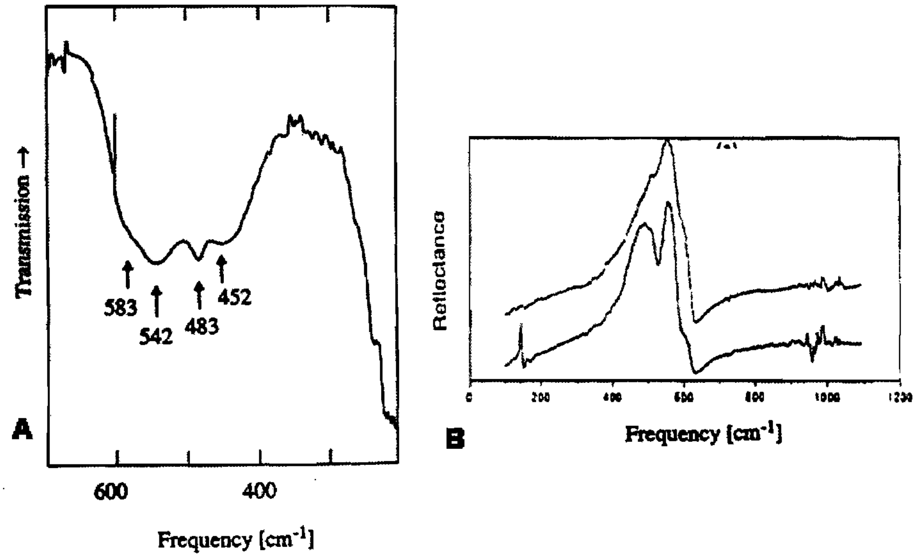

Figure 4.19 – Far-IR data for CuO where a peak at 320 cm^{-1} is absent,
A – Transmission spectra of CuO in a paraffin mull at RT [63]
B – Reflectance spectrum of single crystal with
'X' and 'Z' incident polarization [64]

In work by Kuz'menko *et al.*[46] taking reflections from the (010) and (001) crystal faces of CuO only certain vibrations are detected due to the orientation of the motion of the vibrations. The peak at 320 cm^{-1}, attributed to the A_{2u} mode, shown in figure 4.7, was clearly present when observing the (001) face but undetected on the (010) crystal face. Although the data presented here and that shown by Hagemann *et al.*[63], are of a polycrystalline sample, consistent with the data shown in figure 4.18, it may be that the peak is diluted to a point that it is hard to detect against the dominant broad peak seen in the spectrum. When observing the (010) face, Kuz'menko *et al.*[46] noted small yet clear peaks attributed to the A_{1u} and A_{3u} modes at approximately

160 cm^{-1} and 400 cm^{-1}, when these two modes should be undetectable when viewing this face. This may suggest that these two modes are more easily detectable than the A_{2u} mode when the crystal orientation is unfavourable.

In the literature a band around 580 cm^{-1} has been noted by many groups however it is generally very weak, e.g. figure 4.18B, as opposed to the strong band clearly visible in figure 4.16A. The band has been assigned to a thick layer of Cu_2O and will be discussed later in section 4.4.1.3. The exposure of this oxide film to 200 mbar CO is also discussed in section 4.4.2.1.

The data presented here shows that the HPRC works well in practice and that the oxidation of a copper foil to CuO was achieved. Unfortunately the work was held back by the uncommonly high noise levels present on the station during the beamtime, the cause of this was subsequently found and eliminated. A second issue with this data surrounds the reliability of the temperatures quoted, although they are taken directly from the thermocouple reading. This is due to the initial reaction of the thermocouple to the activation of the button heater which was unusual, as discussed in section 4.2.2.

4.4.1.2 Synchrotron Cu(100) Single Crystal Oxidation

A second experiment involving the oxidation of copper was performed using synchrotron radiation as the source, however a few changes were made. A new sample stage was incorporated into the system, shown in figure 4.12, which used a Pt resistance thermometer to monitor the temperature of the sample, the sample was also changed from a Cu foil to a Cu(100) crystal. Scans were performed with a resolution of 8 cm^{-1}, a mirror velocity of 3.16 cm s^{-1} and 256 co-added scans, this gave a peak-to-peak value in the 100 % line of approximately 0.15, which was still quite high in comparison to the ideal, but acceptable for the bands considered here.

The progressive oxidation of Cu(100) exposed to 200 mbar of oxygen is shown in figures 4.20A and B, the plots have been offset for clarity. Scans were taken once the crystal had been heated to temperature and allowed to cool to 348 K and compared to a background taken of the clean sample in 200 mbar Ar at 348 K.

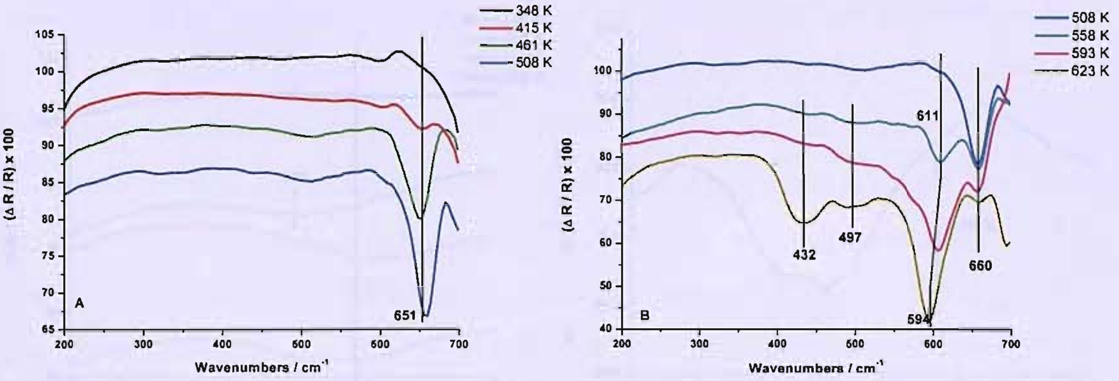

Figure 4.20 - Oxidation of Cu(100) in 200 mbar O_2 using SR far-IR RAIRS, 8 cm^{-1} resolution, 3.16 cm s^{-1} mirror velocity, 256 co-added scans, plots are offset for clarity. Dark blue spectra are identical for plots A and B

Once again signs of the characteristic peak of Cu_2O, near 650 cm^{-1}, start to appear around 415 K, this peak steadily grows in intensity until 558 K where a second peak closer to 600 cm^{-1} appears. As the temperature is raised further, the peak at 650 cm^{-1} diminishes and the peak around 600 cm^{-1} increases, with the appearance of two further bands around 430 and 500 cm^{-1}. Some parallels can be drawn with the data shown in figure 4.16. The peaks around 640 and 580 cm^{-1} are likely to correspond to the peaks around 650 and 600 cm^{-1} shown in figure 4.20. Also, both sets of data have the broad feature between 400 and 500 cm^{-1} associated with CuO, although on the Cu foil the peaks within this feature are, as with the lower temperature data, found at slightly lower wavenumbers. At first glance there is an absence of a peak near 320 cm^{-1} which is consistent with the data from the polycrystalline films, however on closer inspection there is compelling evidence of a small peak present above 593 K, as shown in figure 4.21. As the peak intensity is twice the peak-to-peak noise value of the 100 % line, it is reasonable to assume this is the A_{2u} mode.

In further experiments this oxide layer was exposed to 200 mbar of CO, the results of which are discussed in section 4.4.2.2.

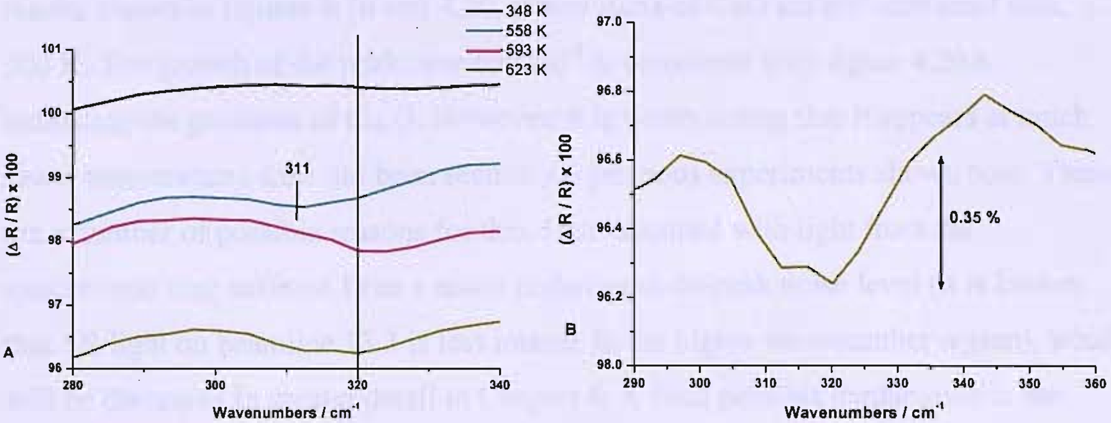

Figure 4.21 - Oxidation of Cu(100) in 200 mbar O_2 using SR far-IR RAIRS, 8 cm^{-1} resolution, 3.16 cm s^{-1} mirror velocity, 256 co-added scans.
A – Potential 320 cm^{-1} peak following high temperature oxidation
B – close up view of 623 K scan

4.4.1.3 Globar Cu(100) Single Crystal Oxidation

A third set of copper oxidation data was obtained, however due to the difficulties previously experienced with the synchrotron ring, a globar source was used. For far-IR RAIRS this would normally cause an issue, due to the monolayer coverages investigated, however due to the large bands seen during oxidation this issue was found to be negligible. In this experiment the oxidation was not taken to such high temperatures, which should allow the crystal to be easily cleaned via sputtering, whereas previously it needed to be sent back to the manufacturer to be repolished. Spectra were collected with a resolution of 8 cm^{-1}, a mirror velocity of 1.89 cm s^{-1} with 5120 co-added scans, this gave a peak-to-peak value of approximately 0.035 in the 100 % line.

The progressive oxidation of Cu(100) exposed to 200 mbar of oxygen is shown in figure 4.22. Scans were taken once the crystal had been heated to temperature and allowed to cool to approximately 328 K and compared to a background of the clean sample, obtained in 200 mbar Ar at 328 K.

Due to the lower temperatures investigated during this process the oxidation is expected to only progress to the formation of Cu_2O, in agreement with the other results shown in figures 4.16 and 4.20, where signs of CuO are not seen until near 500 K. The growth of the peak near 650 cm^{-1} is consistent with figure 4.20A indicating the presence of Cu_2O. However, it is worth noting that it appears at much lower temperatures than has been seen in the previous experiments shown here. There are a number of possible reasons for this. Data obtained with light from the synchrotron ring suffered from a much higher peak-to-peak noise level (it is known that SR light on beamline 13.3 is less intense in the higher wavenumber region), which will be discussed in greater detail in Chapter 6. A final possible explanation is the exposure time of the crystal in 200 mbar of O_2; for the second set of data, with SR light, 256 scans were collected, this took under ten minutes per scan, whereas for the globar data 5120 scans were collected leading to a collection time per scan of over one hour. This clearly leads to difficulties directly correlating the two sets of data.

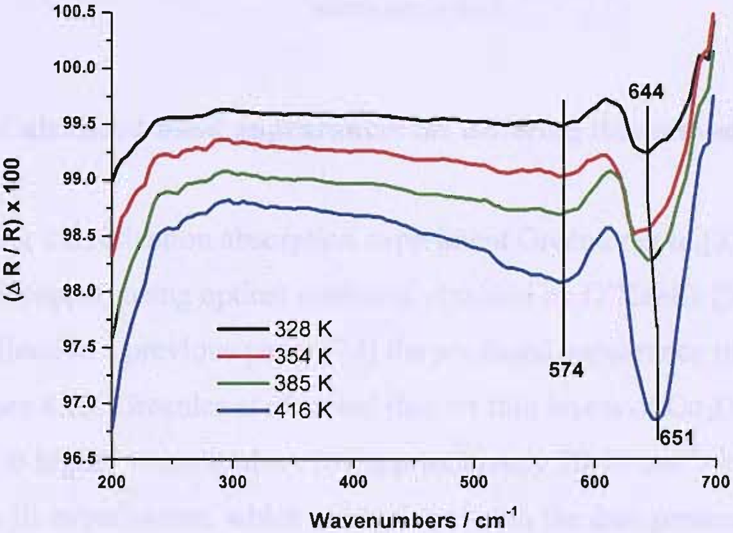

Figure 4.22 - Oxidation of Cu(100) in 200 mbar O_2 using a globar source, 8 cm^{-1} resolution, 1.89 cm s^{-1} mirror velocity, 5120 co-added scans.

As seen in figure 4.22 a second peak appears to grow around 574 cm^{-1}. However, the shape is unusual and may be an artefact of the glowbar in relation to the relatively large peak at 650 cm^{-1} and the hump before it around 610 cm^{-1}. Alternatively, the data presented in figures 4.16 and 4.20 both show a peak present just below 600 cm^{-1}, it is possible the peak at 574 cm^{-1} in figure 4.22 is consistent with those results. The intensity of this peak in the synchrotron sourced data is far greater than would be expected from the higher end vibrational modes of CuO, i.e. the B_{3u} mode. In the data presented in figure 4.22 the peak appears at a much lower temperature than would be expected if it was associated with the formation of CuO. Thus it is reasonable to assume that it may be connected to the formation of Cu_2O.

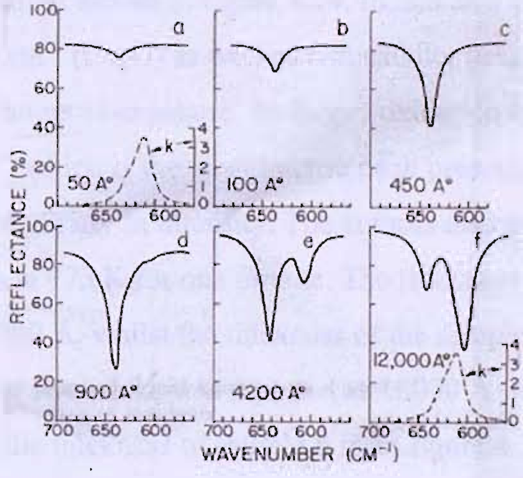

Figure 4.23 – Calculated band appearances for differing thicknesses of Cu_2O [53]

When designing the reflection absorption experiment Greenler *et al.*[53] considered the oxidation of copper, using optical constants obtained by O'Keeffe [54] in a calculation outlined in a previous paper [74] the predicted appearance of a band was shown, see figure 4.23. Greenler *et al.* noted that for thin layers of Cu_2O the observed band is shifted to higher wavenumbers (by approximately 20-30 cm^{-1}) in comparison to transmission IR experiments, which is consistent with the data presented in this thesis. The authors also showed that, according to their calculations, for thicker layers of Cu_2O a second peak appears near 600 cm^{-1} which, as the thickness increases, begins to dominate the spectra. This looks very consistent with the data shown in figure 4.20, and could in some respects explain what is seen in figures 4.16 and 4.22. However in their paper Greenler *et al.*[53] performed some preliminary investigations and found no second peak for a sample of thickness 4200 ± 300 Å. The authors performed these experiments on vacuum deposited Cu films which were then oxidised at 418 K in approximately 230 mbar O_2, however no time scale was discussed.

This peak shifting as a result of oxide thickness has not been shown or discussed in great detail in the literature, as a large quantity of data has been obtained directly from powders or anodic films. Two papers cover the progressive oxidation of copper, the second of these papers published by Lefez *et al.*[67] discusses the oxidation of Cu in dry synthetic air at 473 K, a difference in spectra for oxidation performed over 4 hours and over 24 hours is seen, as shown in figure 4.24. In this data it is possible to see a single peak around 650 cm^{-1} (Cu_2O) as well as two smaller peaks around 500 and 440 cm^{-1} (CuO) after 4 hours of exposure. At longer oxidation times an extra peak appears around 600 cm^{-1} which is the most intense peak present, the peak around 650 cm^{-1} having reduced greatly in intensity. The authors also note a double peak when oxidising samples at 773 K for one minute. The thickness of sample a in figure 4.24 is reported to be 3000 Å, whilst the thickness of the sample oxidised at higher temperature, showing the two peaks was reported as 18000 Å (not shown here). The authors do not mention the thickness of sample b from figure 4.24.

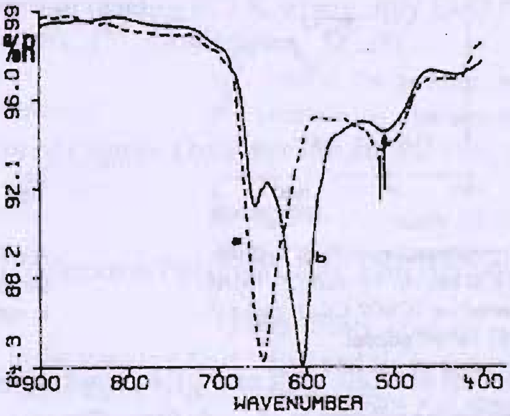

Figure 4.24 – IR reflectance spectra of Cu oxidised in air: (a) at 473 K for 4 h; (b) at 473 K for 24 h [67].

The earlier paper covering the progressive oxidation of Cu was published by an associated group, the report is less in depth but reports similar findings when oxidising a Cu sample in air at 573 K. The authors attribute the peak at 650 cm^{-1} to the LO mode and the peak near 600 cm^{-1} to the TO mode from Cu_2O [28]. It was reported that the TO peak was observed with oxide thicknesses of 5000 Å, the TO peak was then found to have the highest intensity when thicknesses grew beyond 6000 Å.

From this data it seems unreasonable to conclude that this is the effect seen in figure 4.22 as it is highly unlikely a Cu_2O film of suitable thickness would have formed at that temperature even given the long exposure times experienced due to the use of a globar source.

The data presented in these 3 sections, especially in figure 4.20, seems consistent with the literature results discussed here. Oxidation of a Cu(100) crystal in 200 mbar O_2 occurs at temperatures as low as 328 K to form Cu_2O as evidenced by the strong peak near 650 cm^{-1}. As the temperature and exposure time increases the intensity of this peak increases indicating further oxide formation. Once this Cu_2O layer grows above 4000 Å thick, a second peak is detectable near 600 cm^{-1} which is associated with the TO mode of Cu_2O. As the oxide layer grows further the intensity of this second peak grows at the expense of the first peak at 650 cm^{-1}. As the exposure temperature is raised above 523 K peaks attributable to the formation of the second form of copper oxide, CuO, appear in the spectra. The two oxide forms appear to co-exist until the temperature reaches 673 K where only CuO remains detectable.

4.4.2 Far-IR Reduction of Copper Oxides in the HPRC

4.4.2.1 Synchrotron Polycrystalline Foil Reduction

The oxide layer formed in figure 4.16 was then allowed to cool in 200 mbar of oxygen, the cell evacuated and refilled with 200 mbar Ar and a number of scans taken as background files in 200 mbar Ar at different temperatures. This caused the oxide layer to change, as shown in figure 4.25. Following the cooling and annealing process, the oxide peaks appear broader, the peak associated with a thin layer of Cu_2O around 630 cm^{-1} is quite dominant, and clear peaks are observed at 378 cm^{-1} and 448 cm^{-1} indicating the presence of CuO. The overall level of reflection has decreased, which would suggest a higher level of oxidation. The sharp peaks just below 700 cm^{-1} disappear with the process, this could be due to the lower temperature at which the scan was collected or the removal of the oxygen atmosphere.

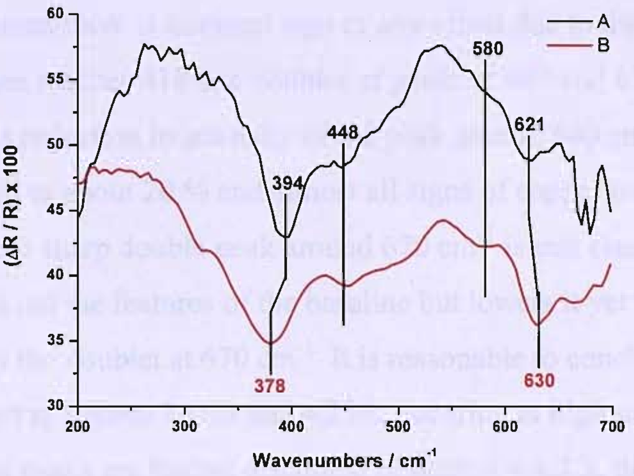

Figure 4.25 – Shift of oxide peaks upon cooling and annealing of foil sample. SR far-IR RAIRS, 8 cm^{-1} resolution, 5.12 cm s^{-1} mirror velocity, 512 scans.
A – Spectra recorded in 200 mbar O_2 at 673 K shown in figure 4.16
B – Spectra recorded after cooling in O_2 and subsequent annealing to 523 K and cooling to 338 K in 200 mbar Ar

The exposure of the oxide layer B, in figure 4.25, to 200 mbar of CO is shown in figure 4.26, scans were taken at temperature, all scans were compared to a background of clean Cu obtained at a similar temperature to the scan shown.

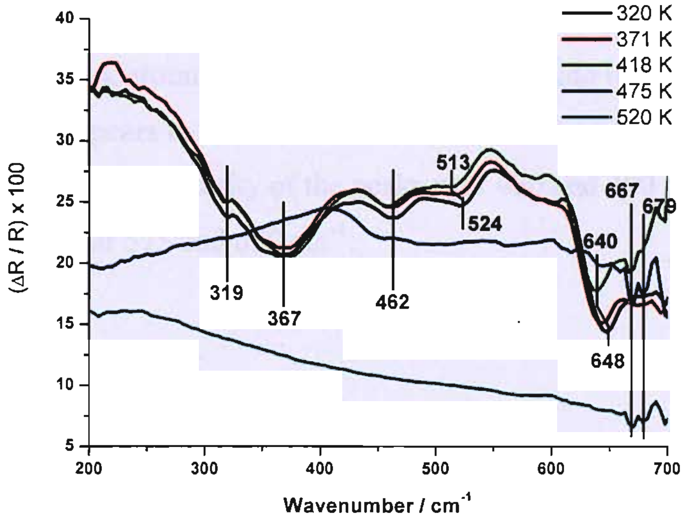

Figure 4.26 – Reduction of copper oxide layer on a polycrystalline foil in 200 mbar CO, using SR far-IR RAIRS
8 cm^{-1} resolution, 5.12 cm s^{-1} mirror velocity, 512 co-added scans.

At lower temperatures there is minimal sign of any effect due to the exposure to CO. Once the temperature reaches 418 K a doublet of peaks at 667 and 679 cm^{-1} starts to appear, with a slight reduction in intensity of the peak around 640 cm^{-1}. At 475 K the baseline has dropped to about 20 % and almost all signs of copper oxide have been removed, whereas the sharp double peak around 670 cm^{-1} is still clear. Increasing the temperature flattens out the features of the baseline but lowers it yet further, the only detectable feature is the doublet at 670 cm^{-1}. It is reasonable to conclude this doublet is the same as that seen in figures 4.16B and 4.25A, occuring at high sample temperatures. These peaks are further discussed in section 4.4.2.3, their presence in figures 4.16B and 4.25A is attributed to unexpected CO impurities in the system. A note of caution should be added that synchrotron light combined with the detector, which has a cut off at 700 cm^{-1} means the ability to detect bands appearing above 650 cm^{-1} can be compromised due to minimal signal.

4.4.2.2 Synchrotron Cu(100) Single Crystal Reduction

Having formed an oxide layer by exposing Cu(100) to 200 mbar O_2 the reduction of this layer was investigated using CO. To give a range of backgrounds to compare to, the oxide layer shown in figure 4.20 was heated in 200 mbar Ar to 623 K and scans taken at temperature and whilst the sample was cooling. This heating and cooling cycle caused observable changes to the structure of the oxide layer as shown in figure 4.27. Aside from the peak around 360 cm^{-1} annealing the oxide layer in an oxygen deficient atmosphere appears to have reduced much of the CuO down to Cu_2O as indicated by the decrease of intensity of the peaks near 430 and 490 cm^{-1} and the increase of the peaks near 575 and 650 cm^{-1}.

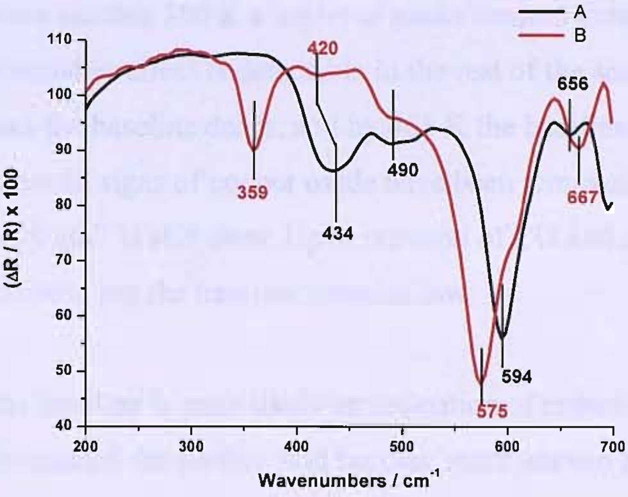

Figure 4.27 – Shift of oxide peaks upon annealing in 200 mbar Ar. SR-far-IR, 8 cm^{-1} resolution, 3.16 cm s^{-1} mirror velocity, 256 co-added scans.
A – Spectra recorded in 200 mbar Ar after oxidation shown in figure 4.18
B – Spectra recorded after annealing to 623 K and cooled in 200 mbar Ar

The reduction of this layer is shown in figure 4.28. Exposed to 200 mbar CO, the sample was heated and allowed to cool to 343 K before obtaining a scan. The sample was then heated further. For comparison a scan obtained once the oxide layer had been heated to 623 K in 200 mbar CO and then allowed to cool to 343 K and the CO replaced with Ar is shown in light blue.

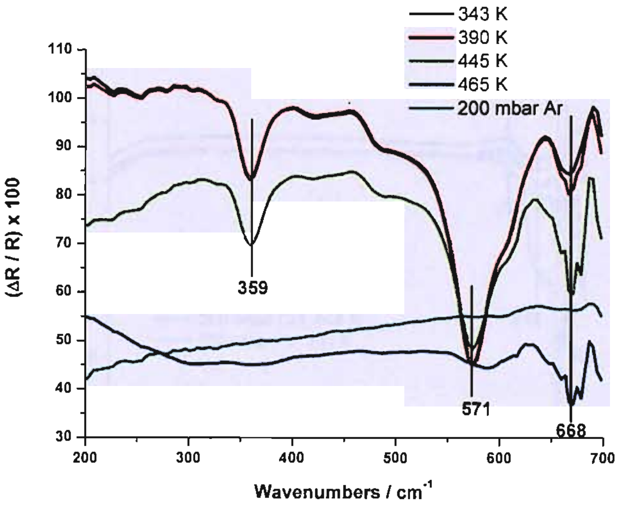

Figure 4.28 – Reduction of copper oxide layer in 200 mbar CO, using SR-far-IR 8 cm^{-1} resolution, 3.16 cm s^{-1} mirror velocity, 256 co-added scans.

Once the temperature reaches 390 K a triplet of peaks centred around 670 cm^{-1} starts to appear, however no other effect is detectable in the rest of the scan. As the temperature increases the baseline drops, and by 465 K the baseline has dropped to about 50 % and almost all signs of copper oxide have been removed, whereas the triple peak around 670 cm^{-1} is still clear. Upon removal of CO and replacing with Ar the triple peak is removed but the baseline remains low.

The dropping of the baseline is most likely an indication of reduction of the sample, as the oxide layer is reduced the surface will become more uneven leading to a reduced level of reflected light. As the triple band is present once the reduction is complete, but absent when CO has been replaced by Ar, it can be assumed to be caused by the presence of CO in the system as suggested in section 4.4.2.1.

4.4.2.3 Globar Cu(100) Single Crystal Reduction

The reduction experiment was also performed on the Cu_2O film shown in figure 4.20, using a globar source. Once again the oxide layer was heated in 200 mbar CO and allowed to cool before a scan was obtained and further heating performed. The results are shown in figure 4.29. Unfortunately, due to the length of time each scan took, the sample was only heated up to 448 K in CO before the beamtime finished. For comparison a scan obtained after the experiment with CO replaced by 200 mbar Ar is shown in light blue.

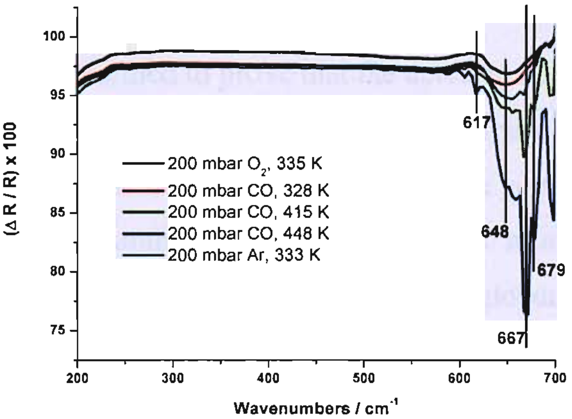

Figure 4.29 – Exposure of copper oxide layer to 200 mbar CO, using a globar 8 cm^{-1} resolution, 1.89 cm s^{-1} mirror velocity, 5120 co-added scans.

Once again a triplet of peaks is seen centred around 667 cm^{-1} once the temperature was raised above 415 K. Upon removal of CO these peaks disappear as discussed previously in section 4.4.2.2. There is also a small peak that appears at 617 cm^{-1} at higher temperatures, which could not be detected in the other reduction experiments.

Adsorption of CO on the Cu surface can be discounted, as not only would the peaks be far less intense, but from the literature, one would expect a band around 345 cm^{-1} for the Cu-CO bond as well as a derivative feature at 285 cm^{-1} attributed to a CO frustrated rotation mode [75]. Contamination of the CO can be ruled out because the species is not present at room temperature, which means the gas line, shown in figure 4.15, works well. If the feed gas is initially pure then a reaction must be occurring within the HPRC. It is at this point where the construction of the HPRC is called into question, the goblet itself is constructed from aluminium as was the original sample stage, however this raised issues under the extreme conditions used and needed to be replaced. The second sample stage was then constructed from stainless steel, without enough thought to the consequencies of using the readily available material. It is therefore possible that the high pressure of CO combined with the raised temperatures used in the reduction experiment could cause a reaction with the new sample stage. However if the doublet seen in the original synchrotron radiation experiments using the aluminium sample stage in section 4.4.2.1 is also attributed to the same species, then a question still remains regarding the origin of these species. A possible answer is that the presence of metal carbonyls due to the high temperature reaction between CO and the stainless steel screws attaching the sample stage in this experiment.

A final experiment was performed to prove that the detected species was present, largely in the gas phase, the results of which are shown in figure 4.30. The HPRC was orientated in such a way that the IR light passed through the goblet but without reflecting off the crystal. The sample was then heated in 200 mbar of CO and scans were taken once the sample had cooled to 320 K using the globar source. Once again the strong feature centred around 668 cm^{-1} appears above 419 K, as well as the small, sharp peak at 617 cm^{-1} seen in figure 4.29.

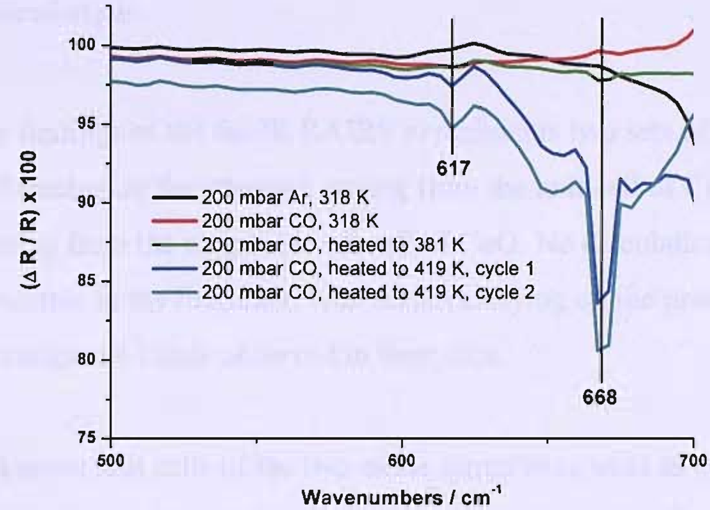

Figure 4.30 – Spectra obtained directly through the HPRC, not reflected off the crystal, using a globar source 8 cm^{-1} resolution, 1.89 cm s^{-1} mirror velocity, 5120 co-added scans.

From the literature, gas phase IR measurements for $Ni(CO)_4$ give peaks at 423, 459 and 541 cm^{-1} [76] in the region of interest, discounting this possibility. Whereas for $Fe(CO)_5$ IR bands are given at 646, 623, 570, 545, 476 and 430 cm^{-1} for the vapour-phase spectrum at low pressure [77]. Of these, the two peaks at higher wavenumbers are the most intense, these two peaks are close to the bands detected on heating in CO. An interaction between the surface and iron pentacarbonyl may explain the shift in the peak position of the 646 cm^{-1} feature by approximately 20 cm^{-1}. Therefore the contamination of the HPRC with $Fe(CO)_5$ from the stainless steel sample holder when heating a sample in 200 mbar CO seems a reasonable explanation.

The data presented in this section shows the reduction of a copper oxide film in 200 mbar CO using the HPRC. Reduction consistently occurred around 465 K, which is in line with the findings of Nagase *et al.*[42]. However difficulties were observed due to a reaction between the stainless steel sample stage and the high pressures of CO used at high temperatures, forming $Fe(CO)_5$ in the gas phase.

4.4.3 DFT Calculations

To support the findings of the far-IR RAIRS experiments two sets of calculations were run. One focusing on the phonons arising from the unit cell of Cu_2O and one on the phonons arising from the magnetic unit cell of CuO. No calculations of this type appear to be available in the literature, with authors relying on the predictions of the space group to assign the bands observed in their data.

Although the known unit cells of the two oxide forms were used as a starting point for the calculation, these parameters are theoretically optimised as the first step. This is essential since calculation of the phonon modes via finite difference relies the initial point being the minimum of the potential energy surface. The alpha and gamma angles were fixed at 90° for both CuO and Cu_2O. The beta angle was also set at 90° for Cu_2O. How much the values change gives a good indication of the errors present in the calculation. The calculated unit cell values are shown in table 4.3 along with the experimentally accepted values and the difference between them. These errors are within acceptable limits.

Experimental	a / Å	b / Å	c / Å	α / °	β / °	γ / °
Cu_2O[73]	4.27	4.27	4.27	90.00	90.00	90.00
CuO[49]	4.68	3.42	5.23	90.00	99.54	90.00
Theoretical						
Cu_2O	4.33	4.33	4.33	Fixed	Fixed	Fixed
CuO	4.83	3.38	5.16	Fixed	99.26	Fixed
Error in Calculation						
Cu_2O	+0.06	+0.06	+0.06	N/A	N/A	N/A
CuO	+0.15	-0.04	-0.07	N/A	-0.28	N/A

Table 4.3 – Experimental and DFT theoretical values for the unit cell of the two copper oxides and the differences between them

The calculated phonon frequencies and their assignments for Cu_2O are shown in table 4.4. These phonon modes were transferred into the DLV visualisation program and captured images of the vibrations are shown in figures 4.31 – 4.36.

Frequency / cm^{-1}	Assignment	Experimental / cm^{-1} [59]	Error / cm^{-1}	Activity
-0.220	Acoustic	N/A	N/A	Inactive
78	F_{2u}	N/A	N/A	Inactive
102	F_{1u}	146	-44	Infrared
105	E_u	N/A	N/A	Inactive
349	B_u	N/A	N/A	Inactive
506	F_{2g}	528	-22	Raman
616	F_{1u}	623	-7	Infrared

Table 4.4 – Calculated phonons for Cu_2O using the B3LYP functional

The negative value for the acoustic mode is not of concern, as it is the translation of the whole lattice and is expected to be around zero. The other values given from the calculation are lower than the experimentally observed vibrations, especially the low frequency mode. The errors of 7 and 22 cm^{-1} for the higher modes are within reasonable estimates given that the lattice parameters had relaxed with an error of approximately 1.5 % in comparison to the experimental values.

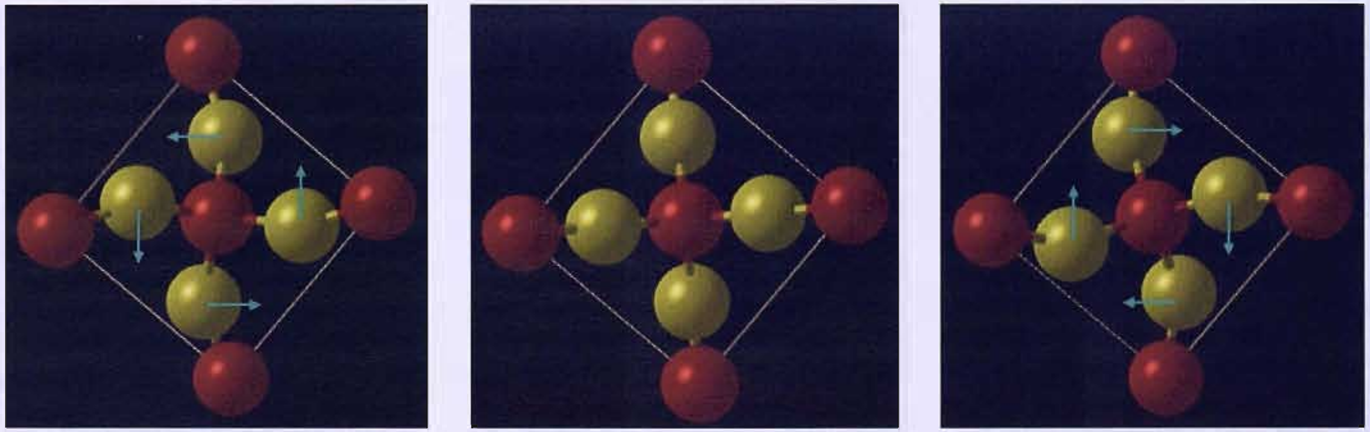

Figure 4.31 – Visualisation of three stages of the calculated phonon of Cu_2O at 78.4 cm^{-1}, assigned to the F_{2u} mode, O^{2-} ions as red spheres, Cu^{+} ions as gold spheres, blue arrows indicate direction of movement to return to relaxed position

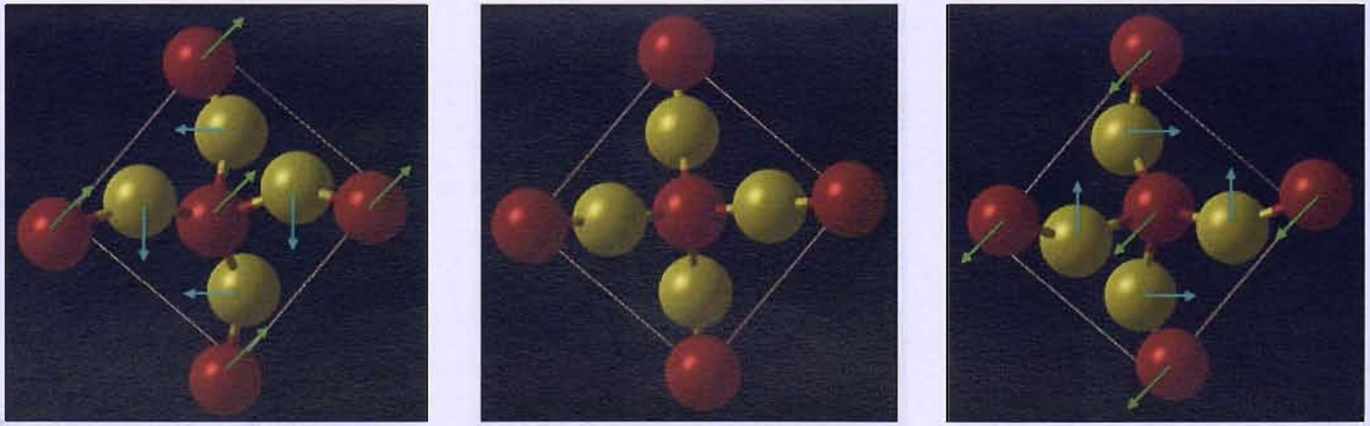

Figure 4.32 – Visualisation of three stages of the calculated phonon of Cu_2O at 102.4 cm^{-1}, assigned to the F_{1u} mode, O^{2-} ions as red spheres, Cu^{+} ions as gold spheres, blue and green arrows indicate direction of movement to return to relaxed position

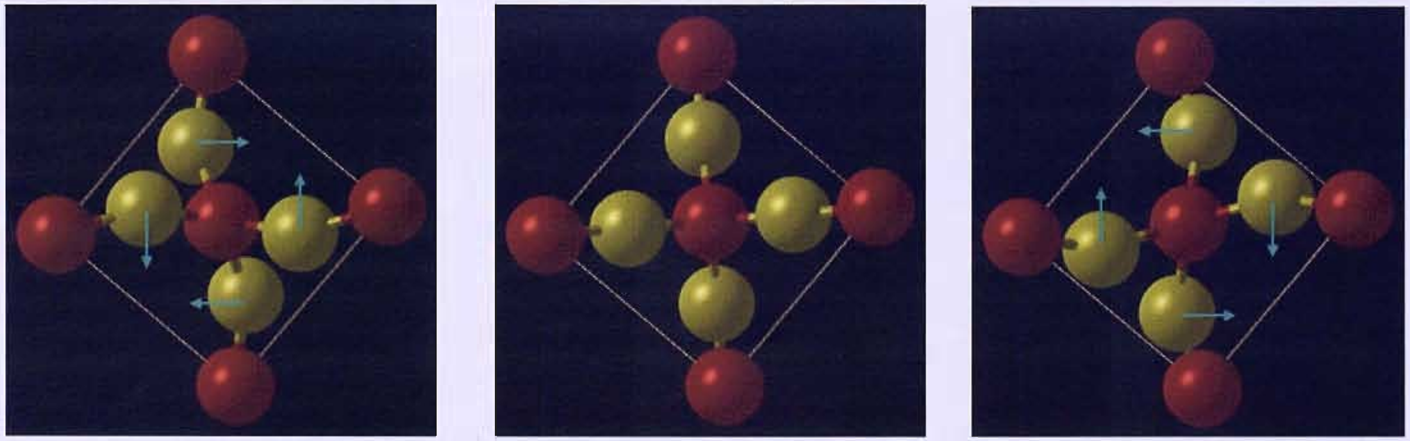

Figure 4.33 – Visualisation of three stages of the calculated phonon of Cu_2O at 104.6 cm^{-1}, assigned to the E_u mode, O^{2-} ions as red spheres, Cu^+ ions as gold spheres, blue arrows indicate direction of movement to return to relaxed position

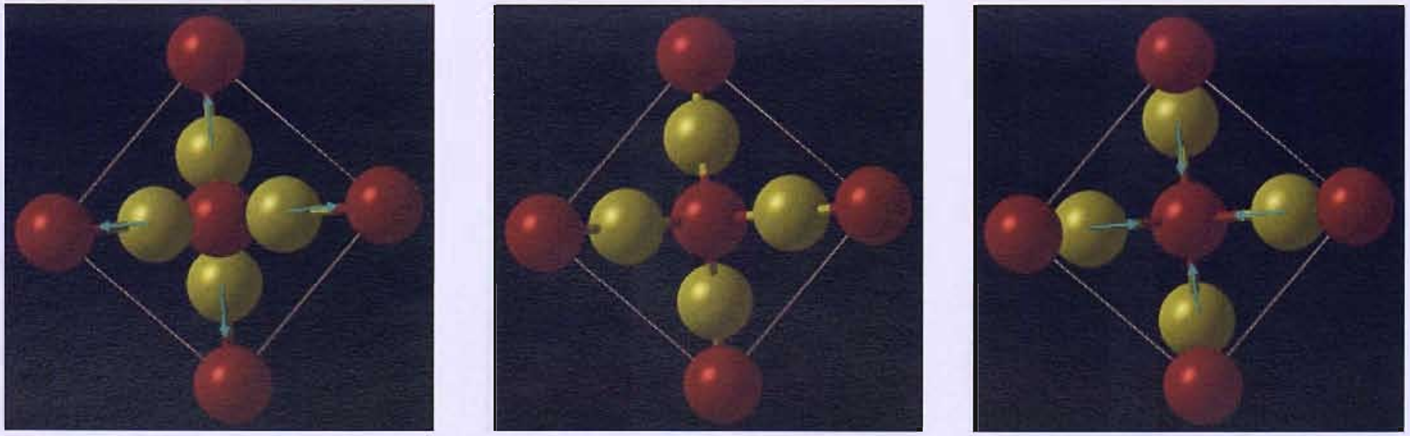

Figure 4.34 – Visualisation of three stages of the calculated phonon of Cu_2O at 349.3 cm^{-1}, assigned to the B_u mode, O^{2-} ions as red spheres, Cu^+ ions as gold spheres, blue arrows indicate direction of movement to return to relaxed position

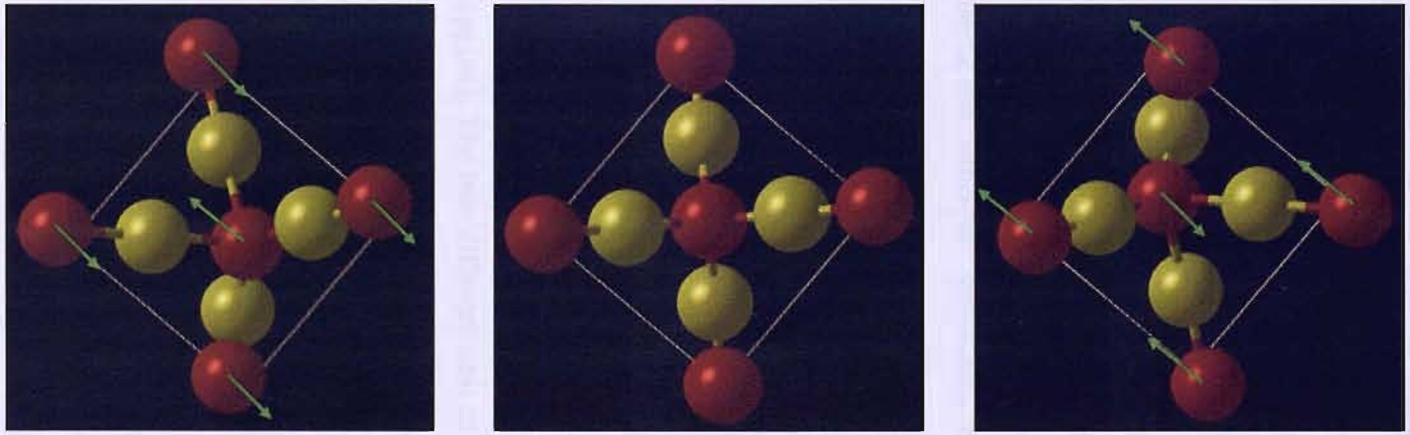

Figure 4.35 – Visualisation of three stages of the calculated phonon of Cu_2O at 509.5 cm^{-1}, assigned to the F_{2g} mode, O^{2-} ions as red spheres, Cu^+ ions as gold spheres, green arrows indicate direction of movement to return to relaxed position

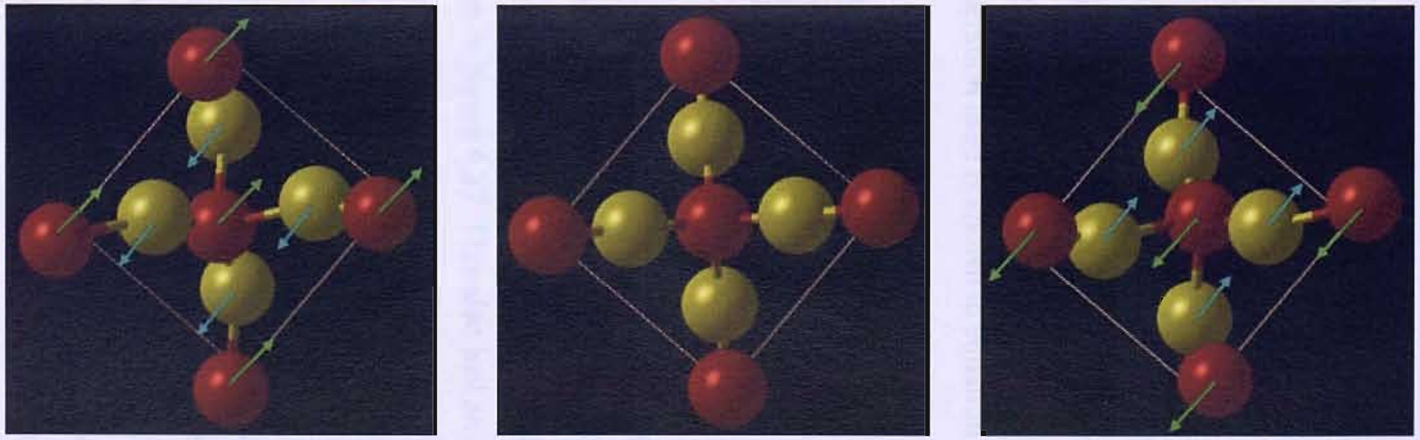

Figure 4.36 – Visualisation of three stages of the calculated phonon of Cu_2O at 615.7 cm^{-1}, assigned to the F_{1u} mode, O^{2-} ions as red spheres, Cu^+ ions as gold spheres, blue and green arrows indicate direction of movement to return to relaxed position

The two infrared active vibrational modes (F_{1u}) are very similar, in that they both involve movement of the O lattice as well as movement of the Cu ions, and could be easily mis-assigned. In comparison to the work presented by Dawson *et al.* [48], reproduced in figure 4.5, the first F_{1u} mode shown can be assigned as the 616 cm^{-1} phonon and the second F_{1u} mode as the 102 cm^{-1} phonon. This can be attributed with certainty as it is possible to view the 616 cm^{-1} vibration from such an angle that all motion is within that plane and no movement was observed. This is impossible with the vibration found at 102 cm^{-1}.

The calculation for CuO was more difficult than that performed for Cu_2O, as the electron spin orientation needed to be taken into account in order to model the effects arising from the +2 oxidation state of the copper. The structural cell was modified using the 'supercell' command, the matrix operation used is shown in equation 4.1.

$$\begin{pmatrix} 1 & -1 & 1 \\ 1 & 1 & 0 \\ -1 & 1 & 1 \end{pmatrix} \qquad \textbf{4.1}$$

The supercell command directs that the unit cell relates the new lattice vectors to the old lattice vectors via a transformation matrix leading to a volume which is four times greater than the original. The relative volume is given by the determinant of the matrix applied. The two different unit cells are shown in figure 4.37. This also had an effect on the number of calculated phonons. Many of these modes are only present in the supercell and not in the original (1 x 1) unit cell. It is clear that if the supercell instruction was not present, these vibrations would not be detected. Since IR is not sensitive to the magnetic moment of the atoms, the modes associated with the base (1 x 1) cell are the only modes of importance. The modes arising from the supercell can be ignored. An example of one of these modes is shown in figure 4.38. In total 48 phonons were detected, of these it is known that three are Raman active and six are infrared active as discussed in section 4.1.3. Only the results of these nine vibrations are shown in table 4.5 and figures 4.39 – 4.47, as many extra phonons have arisen due to the unit cell issue described above. All calculated vibrations are listed in Appendix A.

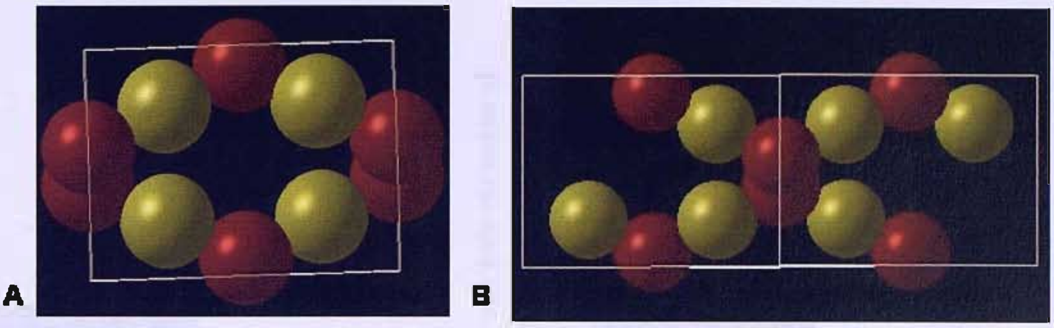

Figure 4.37 – Indication of the CuO unit cells as dictated by:
A – the experimental structure and B – the supercell operation.
O^{2-} ions as red spheres, Cu^{2+} ions as gold spheres

Frequency / cm^{-1}	Assignment	Experimental / cm^{-1} [49]	Error / cm^{-1}	Activity
167	B_{1u}	147	+20	Infrared
179	A_{1u}	161	+18	Infrared
330	A_g	301	+29	Raman
341	A_{2u}	321	+20	Infrared
383	B_{1g}	348	+35	Raman
426	A_{3u}	478	-52	Infrared
456	B_{2u}	530	-74	Infrared
580	B_{3u}	590	-10	Infrared
649	B_{2g}	632	+17	Raman

Table 4.5 – Calculated phonons for CuO using the B3LYP functional

The results from the calculation have on the whole overestimated the vibrational frequency, in accordance with a report by Scott and Radom [78], in which the authors compare the performance of a variety of modern functionals attempting to predict the vibrational frequencies for a large suite of test molecules. A more recent report suggests scaling factors of 0.9679 for vibrational frequencies, 1.010 for low-frequency vibrations and 0.9877 for zero-point energy vibrations when using the B3LYP functional [79]. When these scaling factors are incorporated the results presented are generally still a little high. In fact the low-frequency vibrations are more suited to the scale factor proposed for higher frequencies.

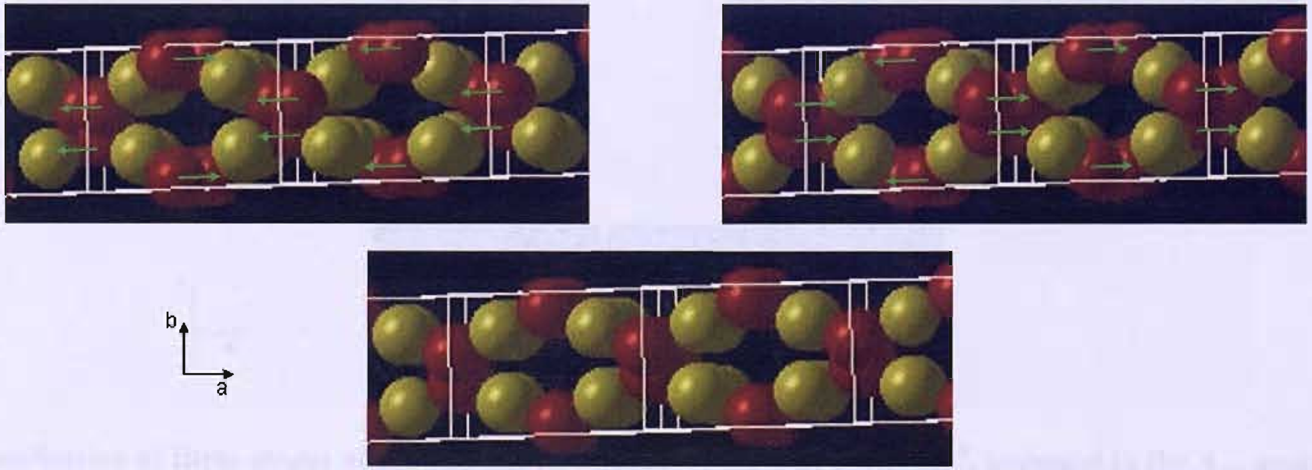

Figure 4.38 – Visualisation of three stages of the calculated phonon of CuO at 603.8 cm^{-1}, indicating the need to use two structural unit cells to map a phonon due to magnetic structure. green arrows indicate direction of movement to return to relaxed position

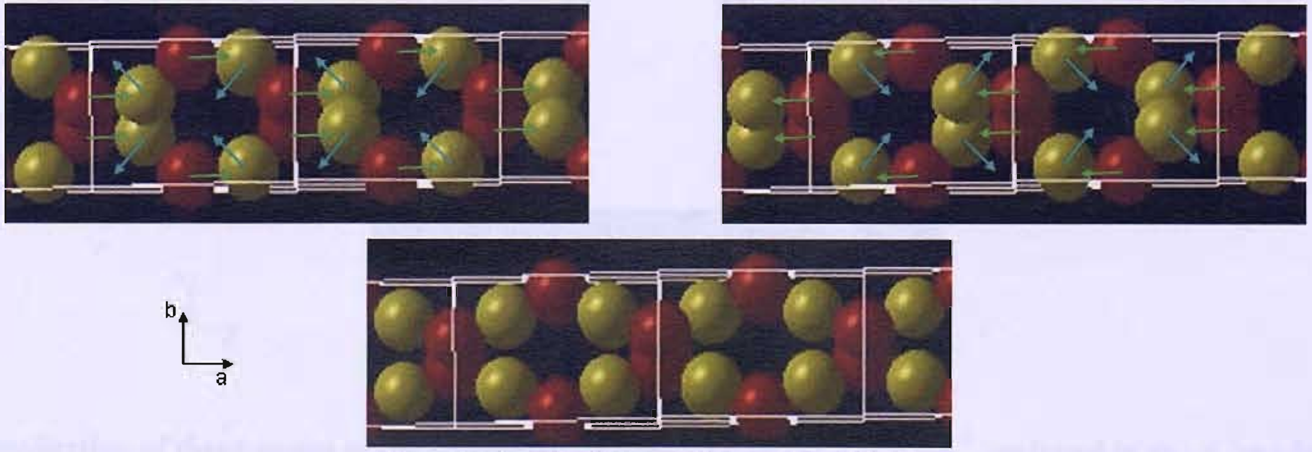

Figure 4.39 – Visualisation of three stages of the calculated phonon of CuO at 166.8 cm^{-1}, assigned to the B_{1u} mode, O^{2-} ions as red spheres, Cu^{2+} ions as gold spheres, green and blue arrows indicate direction of movement to return to relaxed position

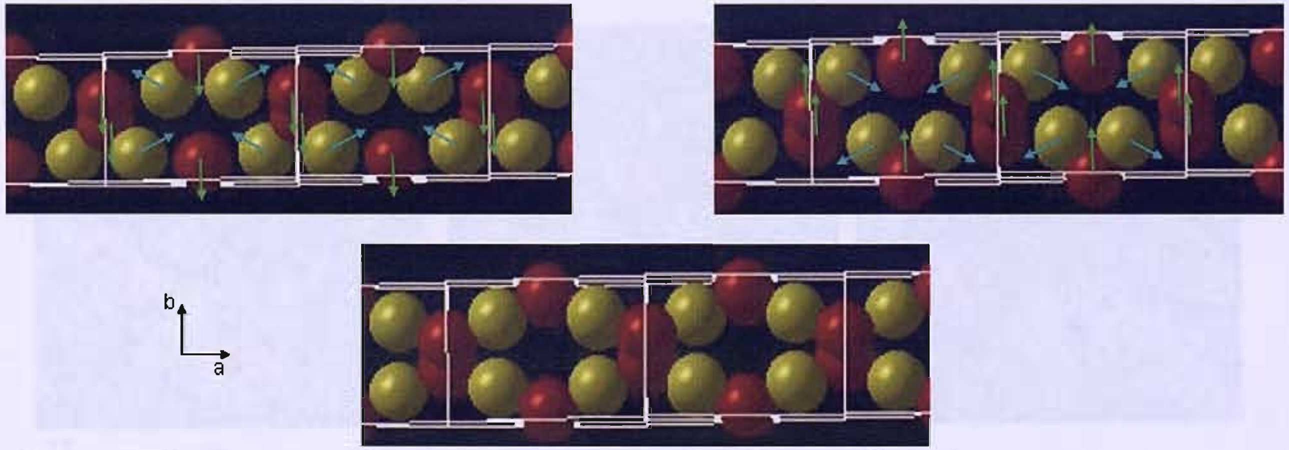

Figure 4.40 – Visualisation of three stages of the calculated phonon of CuO at 179.3 cm^{-1}, assigned to the A_{1u} mode, O^{2-} ions as red spheres, Cu^{2+} ions as gold spheres, green and blue arrows indicate direction of movement to return to relaxed position

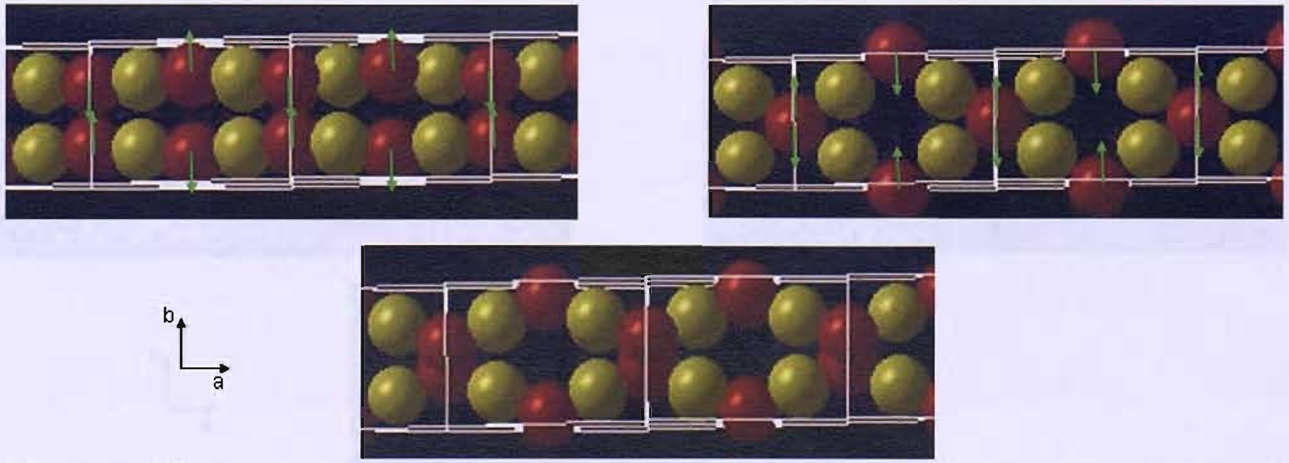

Figure 4.41 – Visualisation of three stages of the calculated phonon of CuO at 329.8 cm^{-1}, assigned to the A_g mode, O^{2-} ions as red spheres, Cu^{2+} ions as gold spheres, green arrows indicate direction of movement to return to relaxed position

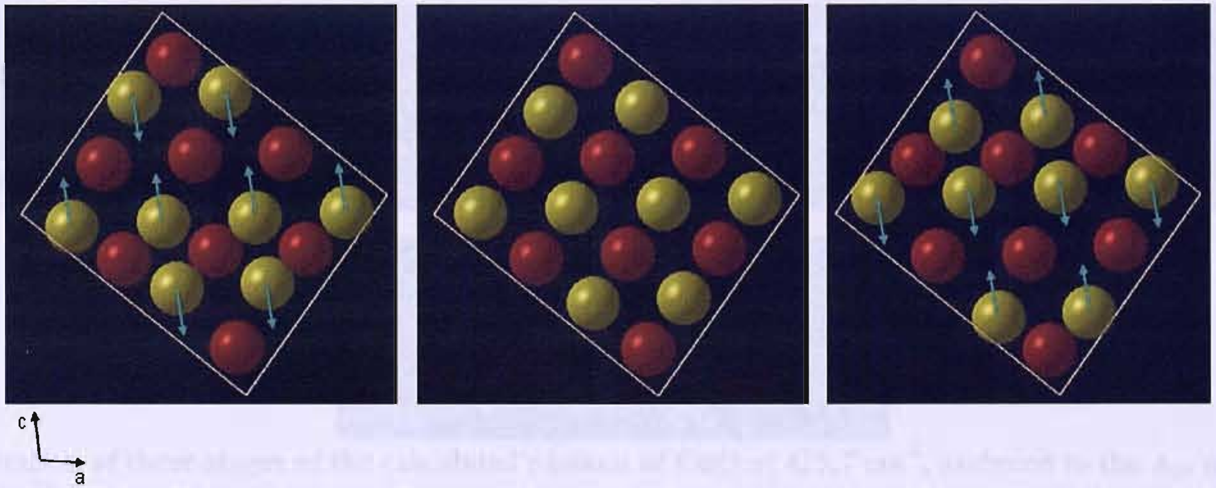

Figure 4.42 – Visualisation of three stages of the calculated phonon of CuO at 340.9 cm^{-1}, assigned to the A_{2u} mode, O^{2-} ions as red spheres, Cu^{2+} ions as gold spheres, green and blue arrows indicate direction of movement to return to relaxed position

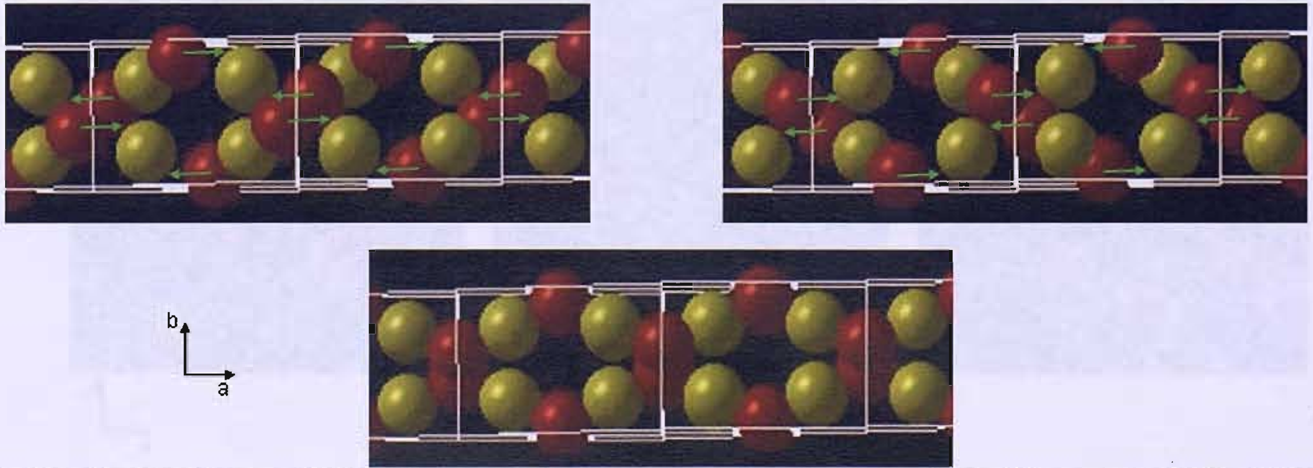

Figure 4.43 – Visualisation of three stages of the calculated phonon of CuO at 382.5 cm^{-1}, assigned to the B_{1g} mode, O^{2-} ions as red spheres, Cu^{2+} ions as gold spheres, green arrows indicate direction of movement to return to relaxed position

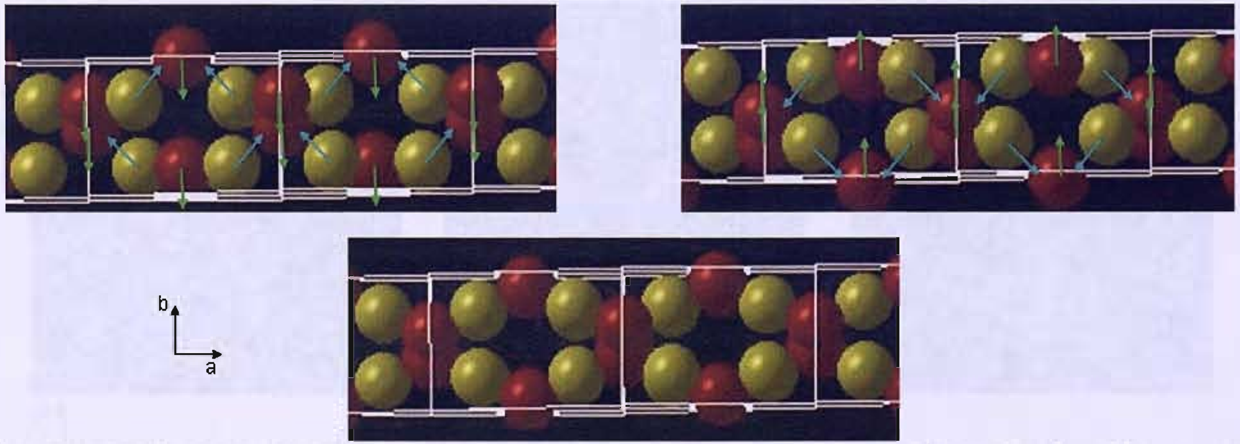

Figure 4.44 – Visualisation of three stages of the calculated phonon of CuO at 425.7 cm^{-1}, assigned to the A_{3u} mode, O^{2-} ions as red spheres, Cu^{2+} ions as gold spheres, blue arrows indicate direction of movement to return to relaxed position

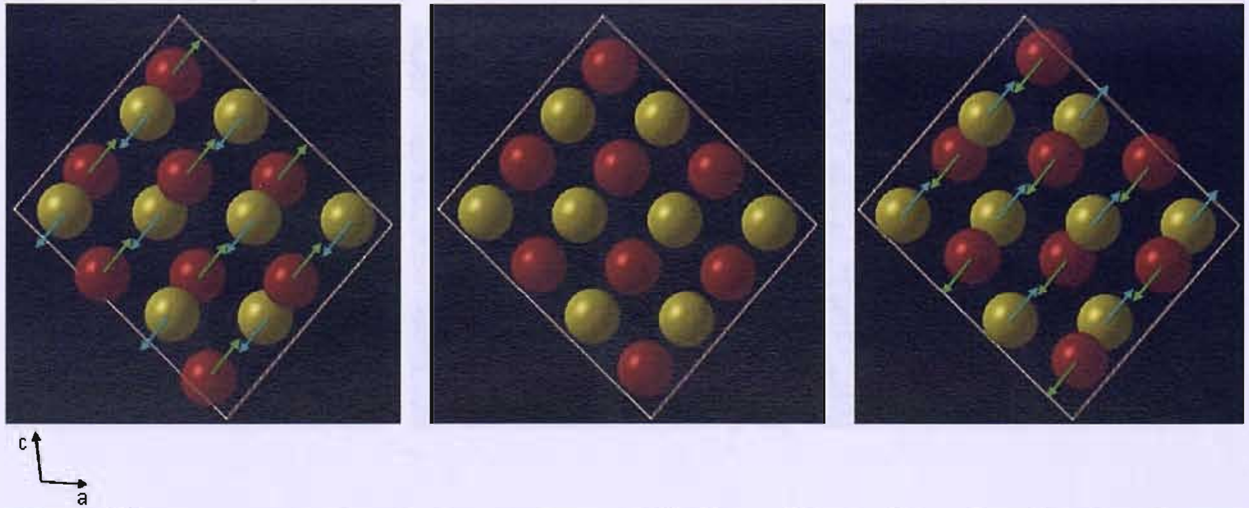

Figure 4.45 – Visualisation of three stages of the calculated phonon of CuO at 456.1 cm^{-1}, assigned to the B_{2u} mode, O^{2-} ions as red spheres, Cu^{2+} ions as gold spheres, blue arrows indicate direction of movement to return to relaxed position

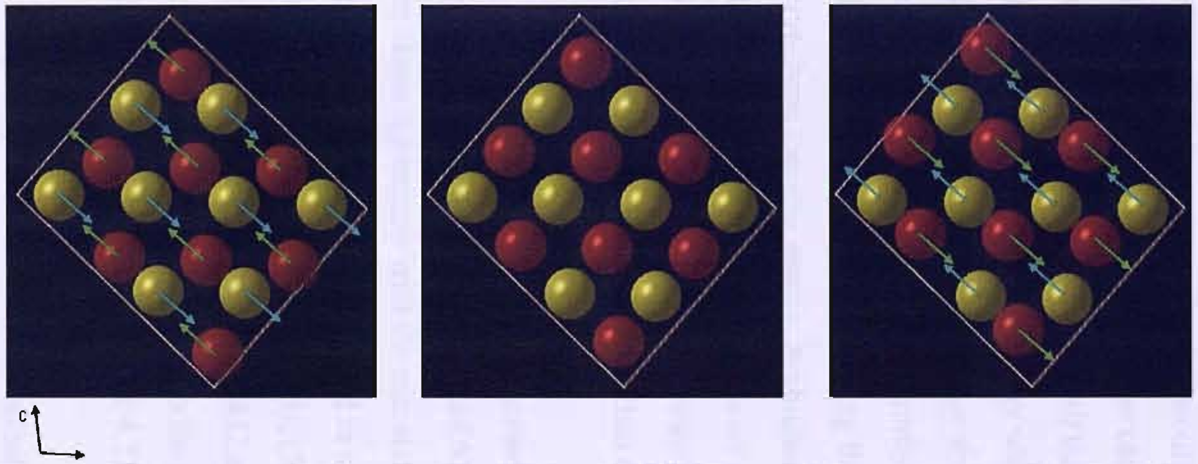

Figure 4.46 – Visualisation of three stages of the calculated phonon of CuO at 579.9 cm^{-1}, assigned to the B_{3u} mode, O^{2-} ions as red spheres, Cu^{2+} ions as gold spheres, green and blue arrows indicate direction of movement to return to relaxed position

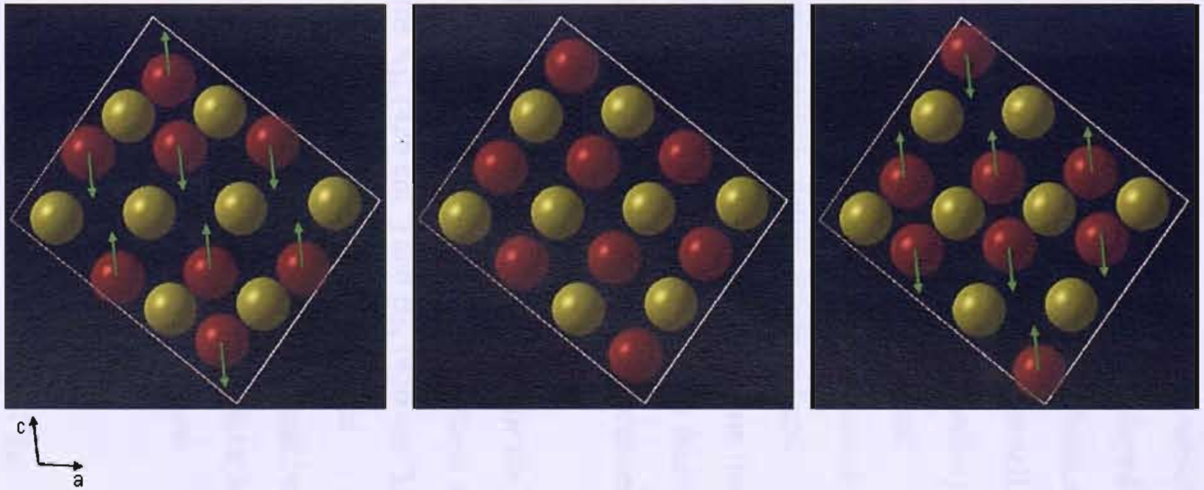

Figure 4.47 – Visualisation of three stages of the calculated phonon of CuO at 649.1 cm^{-1}, assigned to the B_{2g} mode, O^{2-} ions as red spheres, Cu^{2+} ions as gold spheres, green arrows indicate direction of movement to return to relaxed position

The least accurate prediction occurs for the B_{2u} phonon, calculated at 456 cm^{-1} with an error of -74 cm^{-1}. Upon comparison of the images presented in figure 4.45 it is clear that the motion of the two lattices do not overlap as well as they do in the equivalent vibration presented in figure 4.46. This indicates why the error in the calculation is quite so large. It is also interesting to note that in both of these vibrations involving the movement of entire lattices, the calculations underestimate the vibrational energy, although it is unclear why this would be the case. The other vibrational mode which has been underestimated in these calculations is of a different type and is displayed in figure 4.44. On comparison of all three modes, it appears that during these vibrations, ions come into greater proximity with other oppositely charged ions within the cell, than appears to occur in the other six vibrations. The interaction of these oppositely charged ions at such close proximity may have strong affects on the calculation. However it is worth remembering that this is merely conjecture, assisted by potentially fortuitous viewing angles. Additionally the experimentally detected infrared and Raman peaks have been found over a wide range of values and, thus, relying on the results of one group for comparison should be viewed with caution. It may be that the calculations are more accurate than concluded here, due to experimental differences.

In comparison to the data presented in this thesis a case could be proposed for the presence of bands at 420, 467 and 579 cm^{-1} in figure 4.16A. The first two of these are in closer agreement with the calculated phonons A_{3u} (426 cm^{-1}) and B_{2u} (456 cm^{-1}), than the literature values quoted in table 4.5, whilst the 579 cm^{-1} is in excellent agreement with the calculated B_{3u} (580 cm^{-1}) position. A similar argument could be presented for the peaks seen at 432 and 497 cm^{-1} in figure 4.20B. Whilst a similar level of accuracy could be ascribed to the calculated A_{2u} (341 cm^{-1}) band and the peak found around 320 cm^{-1} in figure 4.21B.

From the performance of the calculation of Cu_2O it seems wise to be wary of the peak positions provided from the calculation of the more complex CuO system. However, the calculation has confirmed the presence of the three Raman and six infrared active vibrations as described by Kliche and Popovic [49].

4.5 Conclusions

This chapter presents the first sets of data to be collected at the SRS at Daresbury laboratory using the new HPRC for far-IR RAIRS. The data presented for the *in-situ* oxidation and reduction of copper is largely consistent with the trends shown in the literature. Additional DFT calculations have confirmed the presence of one Raman and two infrared active modes for Cu_2O, the peak positions were calculated within a reasonable error. Four inactive vibrations were also calculated, the dynamics of which were found to be consistent with the literature [48]. A second set of calculations were run for the more complicated CuO structure utilising the supercell command to cope with electron spin orientation, this calculation found 48 phonons between 649 cm^{-1} and 142 cm^{-1}. Many of these modes could be discounted as their presence was attributed to the altered unit cell caused by the supercell command. However the three Raman and six infrared active modes described in the literature [49] were detected and assigned.

Unfortunately the peak positions attributed to CuO, both from the experimental data collected in this thesis and the calculations performed, alongside many reports in the literature all disagree on the specific positions for the IR active bands. However, the work presented in this thesis is consistent with a broader range of peak positions by comparison with a number of published works.

The calculations have provided results which are consistent enough that a conclusion can be drawn regarding a report in the literature. During an electrochemical experiment by Melendres *et al.* [69] a polished Cu electrode was held at -0.05 V vs. the Standard Calomel Electrode (SCE) in 0.1 M NaOH. An IR spectrum was obtained and referenced to a scan obtained at -0.90 V vs. SCE. Three peaks were assigned at 630, 790 and 1110 cm^{-1} and attributed to the formation of Cu_2O. The peak at 630 cm^{-1} is consistent with the calculated and observed frequency for the F_{1u} mode. However neither of the other two peaks bare any resemblance to the results of the calculation. The peak at 790 cm^{-1} has been reported previously in the literature during Raman measurements [80, 81], however the peak at 1110 cm^{-1} has neither been confirmed or discounted. With reference to the DFT calculations presented within this thesis, the peak at 1110 cm^{-1} should not be associated with Cu_2O. Whilst question marks should also be raised regarding the origins of the 790 cm^{-1} band.

The HPRC has been shown to successfully enable a rapid interchange between UHV and more realistic conditions, reducing potential contamination to the clean surface of a sample. The system has been shown to work with both synchrotron and globar sources, although the latter may not be possible with more sensitive experiments. An issue did arise regarding exposure of a sample within the HPRC to high pressures of CO at elevated temperatures, potential solutions to this are discussed in Chapter 6.

4.6 References

1. Somorjai, G.A., *Introduction to Surface Chemistry and Catalysis*. 1994, New York: John Wiley & Sons Ltd.
2. Li, J., Vizkelethy, G., Revesz, P., Mayer, J.W., and Tu, K.N., *J. Appl. Phys.*, 1991. **69**(2): p. 1020.
3. Li, J., Shacham-Diamand, Y., and Mayer, J.W., 1992. **9**: p. 1.
4. Thomsen, C., Cardona, M., Kress, W., Liu, R., Genzel, L., Bauer, M., Schonherr, E., and Schroder, U., *Solid State Commun.*, 1988. **65**(10): p. 1139.
5. Popovic, Z.V., Thomsen, C., Cardona, M., Liu, R., Stanisic, G., Kremer, R., and Konig, W., *Solid State Commun.*, 1988. **66**(9): p. 965.
6. Lee, R.N. and Farnsworth, H.E., *Surf. Sci.*, 1965. **3**: p. 461.
7. Boulliard, J.C., Domange, J.L., and Sotto, M., *Surf. Sci.*, 1986. **165**: p. 434.
8. Habraken, F.H.P.M., Mesters, C.M.A.M., and Bootsma, G.A., *Surf. Sci.*, 1980. **97**: p. 264.
9. Wuttig, M., Franchy, G., and Ibach, I., *Surf. Sci.*, 1989. **213**: p. 103.
10. Sotto, M., *Surf. Sci.*, 1992. **260**: p. 235.
11. Lederer, T., Arvanitis, D., Comelli, G., Troger, L., and Baberschke, K., *Phys. Rev. B*, 1993. **48**: p. 15390.
12. Fujita, T., Okawa, Y., Matsumoto, Y., and Tanaka, K., *Phys. Rev. B*, 1996. **54**: p. 2167.
13. Mohamed, M.H. and Kesmodel, L.L., *Surf. Sci.*, 1987. **185**: p. L467.
14. Sueyoshi, T., Sasaki, T., and Iwasawa, Y., *Appl. Surf. Sci.*, 1997. **121/122**: p. 562.
15. Jensen, F., Besenbacher, E., Laesgaard, E., and Stensgaard, I., *Phys. Rev. B*, 1990. **42**: p. 9206.

16. Zeng, H.C., McFarlane, R.A., and Mitchell, K.A.R., *Surf. Sci.*, 1989. **208**: p. L7.

17. Robinson, I.K., Vlieg, E., and Ferrer, S., *Phy. Rev. B*, 1990. **42**: p. 6954.

18. Tanaka, K., Fujita, T., and Okawa, Y., *Surf. Sci.*, 1998. **401**: p. L407.

19. Tylecote, R.F., *J. Inst. Metals*, 1950-51. **78**.

20. Ronnquist, A. and Fischmeister, H., *J. Inst. Metals*, 1960-61. **89**.

21. Wieder, H. and Czanderna, A.W., *J. Phys. Chem.*, 1962. **66**: p. 816.

22. Lefez, B., Kartouni, K., Lenglet, M., Ronnow, D., and Ribbing, C.G., *Surf. Interface Anal.*, 1994. **22**(1-12): p. 451.

23. Clarke, J.E.G. and Czanderna, A.W., *Surf. Sci.*, 1975. **49**: p. 529.

24. Hapase, M.G., Gharpurey, M.K., and Biswas, A.B., *Surf. Sci.*, 1968. **9**: p. 87.

25. Li, J., Mayer, J.W., and Colgan, E.G., *J. Appl. Phys.*, 1991. **70**(5): p. 2820.

26. O'Reilly, M., Jiang, X., Beechinor, J.T., Lynch, S., Ni Dheasuna, C., Patterson, J.C., and Crean, G.M., *Appl. Surf. Sci.*, 1995. **91**: p. 152.

27. Neumeister, H. and Jaenicke, W., *Z. Phys. Chem. Neue Folge*, 1978. **108**: p. 217.

28. Lenglet, M., Kartouni, K., Machefert, J., Claude, J.M., Steinmetz, P., Beauprez, E., Heinrich, J., and Celati, N., *Mater. Res. Bull.*, 1995. **30**(4): p. 393.

29. Hu, Y.Z., Sharangpani, R., and Tay, S.P., *J. Electrochem. Soc.*, 2001. **148**(12): p. G669.

30. Zhou, L., Gunther, S., Moszynski, D., and Imbihl, R., *J. Catal.*, 2005. **235**(2): p. 359.

31. Cocke, D.L., Chuah, G.K., Kruse, N., and Block, J.H., *Appl. Surf. Sci.*, 1995. **84**: p. 153.

32. Cocke, D.L., Schennach, R., Hossain, M.A., Mencer, D.E., McWhinney, H., Parga, J.R., Kesmez, M., Gomes, J.A.G., and Mollah, M.Y.A., *Vacuum*, 2005. **79**(1-2): p. 71.

33. Lenglet, M., Kartouni, K., and Delahaye, D., *J. Appl. Electrochem.*, 1991. **21**: p. 697.

34. Bellakhal, N., Draou, K., and Brisset, J.L., *J. Appl. Electrochem.*, 1997. **27**(4): p. 414.

35. Mencer, D.E., Hossain, M.A., Parga, J.R., and Cocke, D.L., *J. Mater. Sci. Lett.*, 2002. **21**(14): p. 125.

36. Mencer, D.E., Hossain, M.A., Parga, J.R., and Cocke, D.L., *J. Mater. Sci. Lett.*, 2002. **21**(14): p. 1143.

37. Cocke, D.L., Mencer, D.E., Hossain, M.A., Schennach, R., Kesmez, M., Parga, J.R., and Naugle, G.D., *J. Appl. Electrochem.*, 2004. **34**(9): p. 919.

38. Mencer, D.E., Hossain, M.A., Schennach, R., Grady, T., McWhinney, H., Gomes, J.A.G., Kesmez, M., Parga, J.R., Barr, T.L., and Cocke, D.L., *Vacuum*, 2004. **77**: p. 27.

39. O'Keeffe, M. and Bovir, J.O., *Am. Mineral.*, 1978. **63**: p. 180.

40. Kirsch, P.D. and Ekerdt, J.G., *J. Appl. Phys.*, 2001. **90**(8): p. 4256.

41. Li, J., Vizkelethy, G., Revesz, P., Mayer, J.W., Matienzo, L.J., Emmi, F., Ortega, C., and Siejka, J., *Appl. Phys. Lett.*, 1991. **58**(12): p. 1344.

42. Nagase, K., Zheng, Y., Kodama, Y., and Kakuta, J., *J. Catal.*, 1999. **187**(1): p. 123.

43. Wang, X.Q., Hanson, J.C., Frenkel, A.I., Kim, J.Y., and Rodriguez, J.A., *J. Phys. Chem. B*, 2004. **108**(36): p. 13667.

44. Kim, J.Y., Rodriguez, J.A., Hanson, J.C., Frenkel, A.I., and Lee, P.L., *J. Am. Chem. Soc.*, 2003. **125**(35): p. 10684.

45. Carabatos, C. and Prevot, B., *Phys. Stat. Sol. B*, 1971. **44**: p. 701.

46. Kuz'menko, A.B., van der Marel, D., van Bentum, P.J.M., Tishchenko, E.A., Presura, C., and Bush, A.A., *Phys. Rev. B.*, 2001. **63**: p. Article 094303.

47. Carabatos, C., *Phys. Stat. Sol.*, 1970. **37**: p. 773.

48. Dawson, P., Hargreave, M.M., and Wilkinson, G.R., *J. Phys. Chem. Solids*, 1973. **34**: p. 2201.

49. Kliche, G. and Popovic, Z.V., *Phys. Rev. B.*, 1990. **42**(16): p. 10060.

50. Pastrnyak, I., *Opt. Spectry.*, 1959. **4**: p. 64.

51. Bouster, C., Claudel, J., Gerbaux, X., and Hadni, A., *Ann. Phys. (Paris)*, 1963. **8**: p. 299.

52. Helmetes, E.C., *Phys. Rev.*, 1966. **141**(2): p. 803.

53. Greenler, R.G., Rahn, R.R., and Schwartz, J.P., *J. Catal.*, 1971. **23**: p. 42.

54. O'Keeffe, M., *J. Chem. Phys.*, 1963. **39**(7): p. 1789.

55. Yu, P.Y. and Shen, Y.R., *Phys. Rev. B*, 1975. **12**(4): p. 1377.

56. Yu, P.Y. and Shen, Y.R., *Phys. Rev. Lett.*, 1974. **32**(17): p. 939.

57. Yu, P.Y. and Shen, Y.R., *Phys. Rev. Lett.*, 1974. **32**(7): p. 373.

58. Compaan, A. and Cummins, H.Z., *Phys. Rev. Lett.*, 1973. **31**(1): p. 41.

59. Chan, H.Y.H., Takoudis, C.G., and Weaver, M.J., *Electrochem. Solid State Lett.*, 1999. **2**(4): p. 189.

60. Tevault, D.E., Mowery, R.L., De Marco, R.A., and Smardzeweski, R.R., *J. Chem. Phys.*, 1981. **74**(8): p. 4342.

61. Zhao, M.G., Zeng, X.L., Qian, Y.P., Yi, J., and Zhao, X.N., *J. Phys. C.*, 1987. **20**(32): p. L917.

62. Chrzanowski, J. and Irwin, J.C., *Solid State Commun.*, 1989. **70**(1): p. 11.

63. Hagemann, H., Bill, H., Sadowski, W., Walker, E., and Francois, M., *Solid State Commun.*, 1990. **73**(6): p. 447.

64. Guha, S., Peebles, D., and Wieting, J.T., *Bull. Mat. Sci.*, 1991. **14**(3): p. 539.

65. Homes, C.C., Ziaei, M., Clayman, B.P., Irwin, J.C., and Franck, J.P., *Phys. Rev. B*, 1995. **51**(5): p. 3140.

66. Narang, S.N., Kartha, V.B., and Patel, N.D., *Physica C*, 1992. **204**(1-2): p. 8.

67. Lefez, B., Souchet, R., Kartouni, K., and Lenglet, M., *Thin Solid Films*, 1995. **268**(1-2): p. 45.

68. Chertihin, G.V., Andrews, L., and Bauschlicher, C.W., *J. Phys. Chem. A.*, 1997. **101**(22): p. 4026.

69. Melendres, C.A., Bowmaker, G.A., Leger, J.M., and Beden, B., *J. Electroanal. Chem.*, 1998. **449**(1-2): p. 215.

70. Chan, H.Y.H., Takoudis, C.G., and Weaver, M.J., *J. Phys. Chem. B*, 1999. **103**(2): p. 357.

71. Niaura, G., *Electrochim. Acta*, 2000. **45**(21): p. 3507.

72. Jagminas, A., Kuzmarskyte, J., and Niaura, G., *Appl. Surf. Sci.*, 2002. **201**(1-4): p. 129.

73. Balamurugan, B. and Mehta, B.R., *Thin Solid Films*, 2001. **396**(1-2): p. 90.

74. Greenler, R.G., *J. Phys. Chem.*, 1966. **44**: p. 310.

75. Hirschmugl, C.J., Williams, G.P., Hoffmann, F.M., and Chabal, Y.J., *Phys. Rev. Lett.*, 1990. **65**(4): p. 480.

76. Jones, L.H., McDowell, R.S., and Goldblatt, M., *J. Chem. Phys.*, 1968. **48**(6): p. 2663.

77. Cataliotti, R., Foffani, A., and Marchetti, L., *Inorg. Chem.*, 1971. **10**(8): p. 1594.

78. Scott, A.P. and Radom, L., *J. Phys. Chem.*, 1996. **100**: p. 16502.

79. Andersson, M.P. and Uvdal, P., *J. Phys. Chem. A*, 2005. **109**: p. 2937.

80. Mayer, S.T. and Muller, R.H., *J. Electrochem. Soc.*, 1992. **139**(2): p. 426.

81. Hamilton, J.C., Farmer, J.C., and Anderson, R.J., *J. Electrochem. Soc.*, 1986. **133**(4): p. 739.

Chapter Five – The High Ambient Pressure Photoelectron SpectroscopY (HAPPY) System

5.1 Introduction

Photoelectron spectroscopy is a very highly regarded and, at base level, is an easily affordable experimental technique that has found use in many different areas of surface science. For example, with regards to the oxidation of copper, Lee *et al.*[1] used XPS to observe the shifting composition of a copper oxide film during vacuum annealing, using well defined peak positions from the literature as a guide to the species present.

As discussed previously in Chapter 2, X-ray photoelectron spectroscopy (XPS) is an electron based technique during which photons of a known energy impinge on a sample. Upon irradiation the sample emits core level photoelectrons, the energy of which can be monitored, the spread of these energies provides valuable insight into what elements are present at the surface of the sample. Most of the XPS results that are presented in the literature are collected under UHV conditions. XPS suffers at higher pressure due to the mean free path of the electrons, λ, which is the approximate distance the electrons can travel through a certain pressure, P, of a gas before being scattered. This obviously dictates the possible distance between the sample and the opening to the detector and depends largely on the electron scattering cross section of the gas, θ. If the distance travelled under high pressure is too great the electrons will become inelastically scattered by the gas molecules and will no longer carry information about the surface. The mean free path can be calculated using equation 5.1, where k_B is the Boltzmann constant and T is the temperature in K.

$$\lambda = \frac{4k_BT}{P\theta} \qquad \textbf{5.1}$$

Values of θ can be found in the literature for a number of gases and for a wide range of different electron energies. Using values for the scattering cross section of an electron at 300 eV, shown in table 5.1, and a temperature of 298 K, figure 5.1 shows the attenuation length of an electron in varying pressures of hydrogen, oxygen and helium.

	Hydrogen	Oxygen	Helium
θ / m^2	1.27 x 10^{-16} [2]	4.90 x 10^{-16} [3]	5.46 x 10^{-17} [4]

Table 5.1 – Scattering cross section of an electron at 300 eV

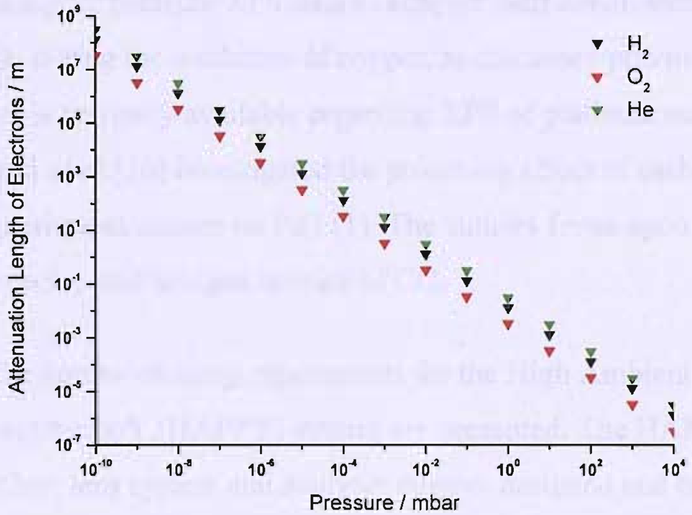

Figure 5.1 – Calculated attenuation lengths of 300 eV electrons

Experiments performed under UHV conditions can suffer from a pressure 'gap', an experimental discrepancy which occurs due to the difference between the idealised conditions, often found in surface science, and those found in real life catalysis. In this chapter the development and commissioning experiments of a newly constructed *in situ* XPS system based at the SRS at Daresbury laboratory, are discussed. The XPS investigation of a sample of a real catalyst, 20 wt % Pt/C, under relatively high pressures of hydrogen and oxygen is shown.

Large volumes of work have been published concerning the XPS of catalytic samples although much of the research is restricted to UHV conditions. Many different reactions, such as the decomposition of alkanethiols [5], the hydrogenation of adsorbed N atoms [6] and the decomposition of NO and NO_2 [7] have been investigated on different platinum metal surfaces using XPS in tandem with other surface science techniques. Platinum nanoparticle catalysts have also been widely researched, investigations into the effect of different pretreatments [8] and supports [9], as well as modification with CeO_2 [10], Cu [11] and Au [12] have been performed in recent years.

With the introduction of newly developed *in situ* XPS systems, data can now be obtained at higher gas pressures, work has been presented on methanol oxidation involving copper oxides [13] and the oxidation of a copper single crystal [14]. Cocke *et al.*[15] showed higher pressure XPS data to support their conclusions regarding the presence of Cu_3O_2 during the oxidation of copper, as discussed previously in Chapter 4. Only one report is currently available regarding XPS of platinum surfaces at higher pressures, Somorjai *et al.*[16] investigated the poisoning effect of carbon monoxide on the hydrogen/deuterium exchange on Pt(111). The authors focus upon the C and O 1s regions to detect on top and bridged species of CO.

In this chapter the commissioning experiments for the High Ambient Pressure Photoelectron spectroscopY (HAPPY) system are presented. The HAPPY setup is a small UHV chamber, lens system and analyser custom designed and built at the SRS at Daresbury laboratory. Constructed on a modest budget the system is designed to enable photoelectron spectroscopy to be performed on a sample from UHV up to approximately 10^{-2} mbar. This combination would enable the user to have control over the surface structure and cleanliness, associated with traditional UHV surface science experiments, whilst then allowing investigations into the surface reactions at more realistic pressures. Data was collected on a mounted sample of a real catalyst and the potential of the HAPPY analyser is shown, further developments to the system are discussed.

5.2 Design of the HAPPY Analyser

The HAPPY analyser is located at Daresbury laboratory. It was designed as a peripatetic end station so that it could be used on a number of experimental stations at the SRS, or attached to a lab source, if required. The development of HAPPY differed greatly from that of the high pressure reaction cell discussed in Chapter 4, the HAPPY analyser is an entire system as opposed to a sample cell like the HPRC. The major aims for the system are shown below:

1. Obtain UHV conditions in the chamber
2. Allow sample cleaning
3. Obtain at least four orders of magnitude pressure difference between sample and analyser

The first two requirements are easily met and are catered for by any standard UHV chamber which has a port directed towards the sample, where an ion gun can be installed, and the ability to introduce gas into the chamber. The third aim is where many of the difficulties lie. As shown in the introduction, if a high pressure of gas is desired the distance between sample and the entrance to the detector must be as small as possible, in essence this dictates the size of the UHV chamber. In order to perform experiments within the system a source, detector and pump are needed, in addition to the ion gun and sample manipulator required to achieve aim two, as such a minimum of five ports is essential. Further to achieving the third aim, it would not be possible to attach a detector directly to the chamber as the pressure would remain too high for operation of the analyser. A differential pumping line needs to be constructed, which would also necessitate additional focussing of the electrons in order to cater for the extra distance travelled by the photoelectrons before reaching the detector.

5.2.1 The Chamber

The chamber is a stainless steel cube with sides of 70 mm, specially constructed by Caburn MDC. Each one of the six faces has a port machined into it. These six ports are attached to a source, a detector, an ion gun, an x, y, z, θ manipulator, a pump and a view port, using the standard UHV knife-edge/gasket arrangement. The ion gun is used to clean the sample via ion sputtering and the manipulator enables the sample to be rotated from the cleaning position to the experimental position and to optimise the sample position. The chamber has three fixed ceramic heaters which are used to bake the chamber to obtain UHV, a frame surrounding the chamber allows the system to be enclosed by a set of bakeout covers. Attached to the manipulator is a sample stage which uses thick wires to ensure a sample remains in place, this arrangement is shown in figure 5.2.

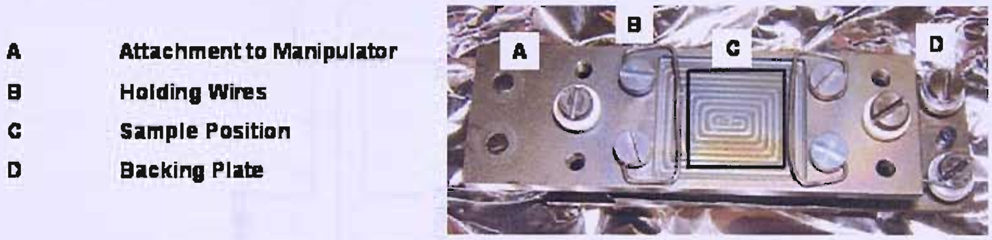

Figure 5.2 – Sample stage for the HAPPY system

Gases can be dosed into the chamber via a leak valve. Three pressure gauges are present on the HAPPY system, these are placed at different points along the pumping stages. A picture of the HAPPY system can be found in figure 5.3 alongside a line diagram which also shows the approximate path of the X-rays upon entering the cube as if the beam were exiting the paper towards the reader.

In order to protect the beamline from the high pressures used in the experiment the chamber is isolated by two differentially pumped boron windows. The binding energy of the 1s electron of boron is 188 eV [17], at this energy the absorption cross section will be quite high however as the photon energy increases this will drop off rapidly making it suitable for measurements with photon energies between 450 and 650 eV as shown in this chapter.

A	Ion Gun
B	HAPPY Cube
C	Pressure Gauges
D	Electrostatic Lens
E	Turbo Pumps
F	Hemispherical Analyser
G	Detector
H	Valve

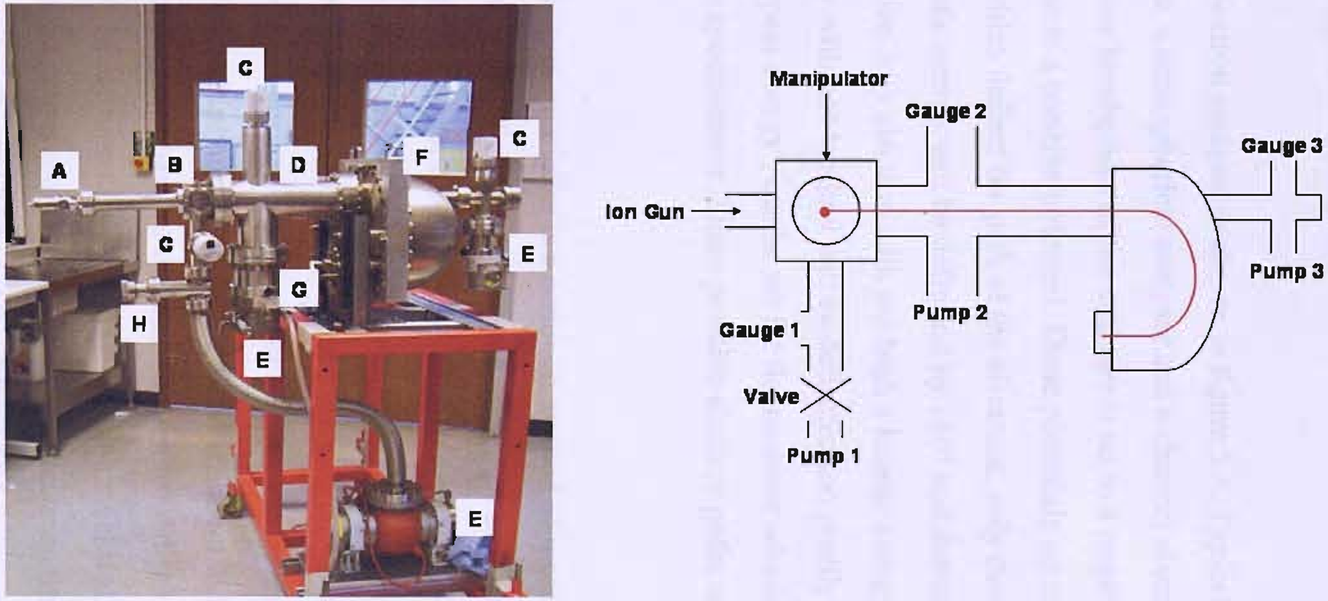

Figure 5.3 – The HAPPY system, source would be directed out of the page, the manipulator enters from above at tag B (as 09-05). Also shown is the simplified path of the X-ray beam (in red) through a line diagram of the spectrometer.

5.2.2 The Hemispherical Analyser

A traditional electron analyser is shown in figure 5.4. Typically they contain an electrostatic lens, a hemispherical analyser and a channel electron multiplier (CEM) detector. The outer hemisphere of the analyser is set to a negative potential and the inner hemisphere to a positive potential. These potentials set up an electric field between them which deflect the path of the electrons, only those electrons with an appropriate kinetic energy will be deflected by 180° and detected by a channel electron multiplier. Any electron with too high a kinetic energy will hit the outer hemisphere, any with one too low will be deflected too greatly and hit the inner hemisphere. A 'pass energy', can be set for the analyser which determines the resolution of the spectrometer. These possible electron paths are also shown in figure 5.4.

The channel electron multiplier is a common method of increasing the signal supplied by the number of electrons detected during an experiment. The CEM is a thin tube made of glass or ceramic with the inside coated in a semi-conducting layer, often BeCu or AgMg. When an electron strikes the semi-conducting surface several secondary electrons are emitted, as these secondary electrons travel further into the channel they strike the surface causing more electrons to be emitted and increasing the signal further. The multiplying effect of the CEM is shown in figure 5.5, they are curved to suppress after-pulsing of the ionised background gas and ensure that as electrons pass down the tube they collide with the channel walls. A potential difference is created across the CEM to attract the electrons through the tube. The nature of the semi-conducting layer means if the CEM is operated at a high voltage a high pressure of gas could cause the CEM to discharge, destroying the electron emissive coating. Due to this restriction the CEM is always operated at pressures below 1 x 10^{-6} mbar.

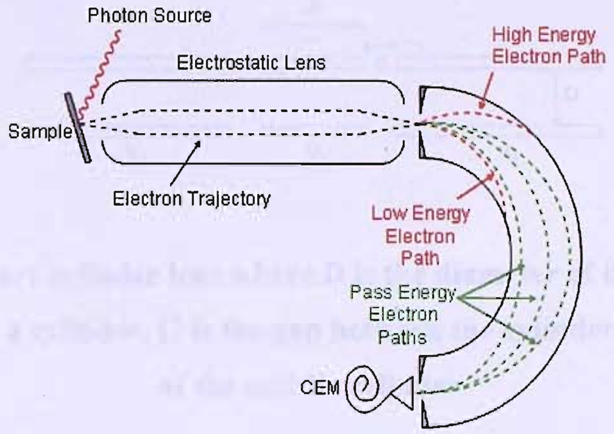

Figure 5.4 – Typical electron paths through a hemispherical analyser

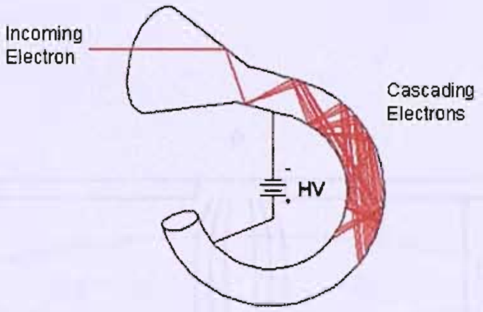

Figure 5.5 – Channel electron multiplier showing electron multiplication and the bias applied across the channel.

The electrostatic lens is used to retard the electrons, this enables the pass energy of the analyser to be lowered, thus improving the resolution. It not only serves this purpose, but as the name suggests, it is also used to focus the electrons towards the analyser. Typically cylinder lenses are used, they consists of two or more cylindrical electrodes, oriented parallel to the optical axis, with small gaps between the electrodes, an example is shown in figure 5.6. Each cylinder is held at a different voltage and the gaps between them act as a lens, the magnification of which can be changed with different voltage combinations, however this can also change the focal point. A three cylinder arrangement can change the magnification whilst ensuring the object and image positions remain constant due to the two gaps both working as lenses.

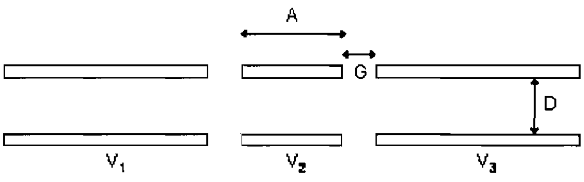

Figure 5.6 – 3-part cylinder lens where D is the diameter of the lens, V_x is the voltage applied to a cylinder, G is the gap between the cylinders and A the length of the middle cylinder

When a charged particle passes through an electric field a force acts upon it, in this case the force experienced is proportional to the displacement of the electron from the optical axis. The variation in the electrostatic field, caused by the voltage differences on the cylindrical elements, leads to a focussing effect on the electrons as seen in figure 5.7.

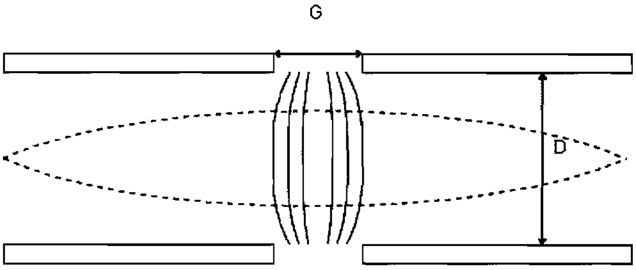

Figure 5.7 – Focussing of a cylinder lens. Equipotential lines shown as solid lines, electron path shown as dashed lines

On the HAPPY system there are two cylinder lenses used in tandem, with dimensions A = 1 D, G = 0.1 D and D = 40 mm, where D is the diameter of the lens, as defined in figure 5.5. The first lens, nearest the sample, consists of three electrodes held at V_1, V_2 and V_3. The second of the cylinder lenses consists of seven electrodes which can be arranged in three orientations providing low, medium or high magnification. The lens positions are shown in figure 5.8.

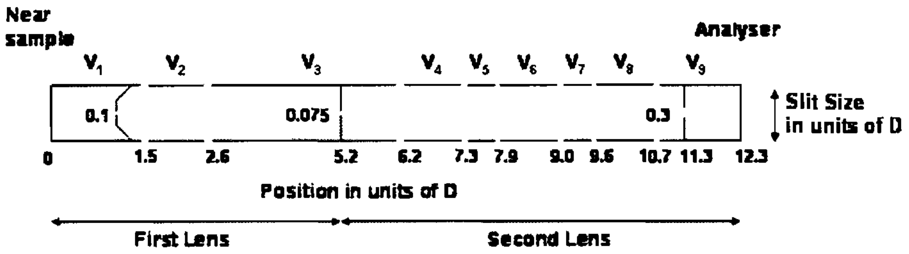

Figure 5.8 – The HAPPY lens system

Regardless of the magnification setting V_1 is always set to the kinetic energy of the photoelectrons and V_3 is always the connecting voltage between the two lenses, V_2 is the focussing voltage which is dependant on which setting is used. Under the low magnification setting, the same voltage is applied to V_3, V_4, V_6 and V_7, whilst V_5 and V_8 are set to the same focussing voltage as V_2. The voltage at V_9 is equal to the pass energy of the analyser.

5.2.3 The Pressure Gradient

If the analyser can only be operated at pressures lower than 1 x 10^{-6} mbar, due to the potential break down of the CEM, and samples are to be investigated at realistic pressures a large pressure gradient from the sample to the analyser is required.

On the HAPPY system this pressure gradient is achieved using differential pumping over four sections, separated by small apertures for the electrons to pass through. Three turbomolecular vacuum pumps are utilised at different points on the system, shown in figure 5.9, these have had additional nose cones introduced to improve their efficiency.

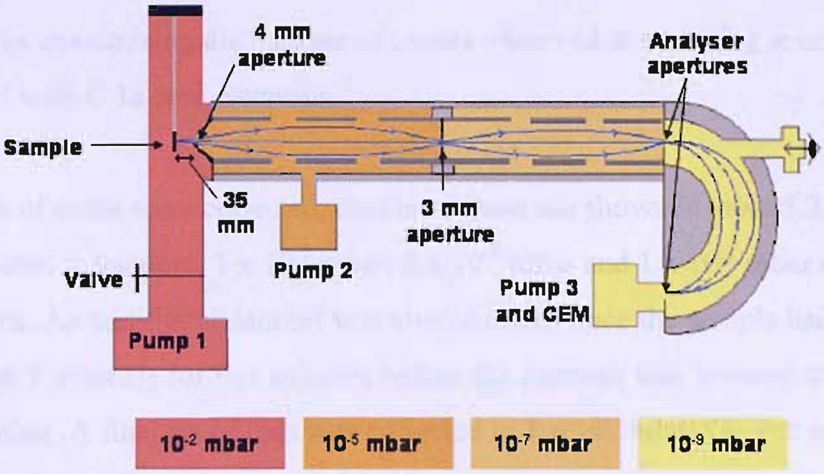

Figure 5.9 – Desired pressure gradient of the HAPPY system with source directed out of the paper

The pump attached directly to the cube is rated at 53 l s^{-1}, the second pump attached to the first cylinder lens is rated at 1000 l s^{-1} and the strongest pump attached to the analyser is rated at 1100 l s^{-1}.

5.3 Experimental

The photoelectron spectroscopy results presented in this chapter were obtained using the specially designed UHV chamber, base pressure at the time of experiment was 5 x 10^{-8} mbar, the specifics of which are shown in section 5.2. All the experiments were performed on beamline 1.1 at the SRS facility at Daresbury laboratory.

A sample of 20 wt % Pt/C was ground to a fine powder using a pestle and mortar, and dispersed in carbon tetrachloride. The suspension was then added dropwise to a sample of high purity Al foil (100 mm^2) using disposable Pasteur pipettes and the solvent allowed to evaporate in a fume hood following the method described by Turner, Thomas and Russell [18].

The sample was transferred onto the manipulator and moved into the HAPPY chamber. Due to the nature of the sample no cleaning of the sample was required and data could immediately be collected once the optimal position was found, this was achieved by maximising the number of counts observed at a binding energy of 285 eV associated with C 1s core electrons.

Two sets of scans were collected, details of these are shown in table 5.2, and each was collected in vacuum, 1×10^{-3} mbar, 5×10^{-3} mbar and 1×10^{-2} mbar of dihydrogen. An additional data set was also obtained once the sample had been exposed to 5 mbar H_2 for five minutes before the pressure was lowered to 1×10^{-3} mbar. A final set of data was collected in 1×10^{-3} mbar O_2. For all data sets the electron multiplier was set to 2.2 keV.

Coadded Scans	Photon Energy / eV	Kinetic Energy Range / eV	Step / eV	FAT
5	650	50 – 700	1.0	90
20	450	140 – 180 350 – 400	0.5	44

Table 5.2 – The two data sets collected using HAPPY for a 20 wt % Pt/C sample mounted on an aluminium foil

The second of these data sets enabled both the carbon 1s and platinum 4f peaks to be collected in a reasonable time scale and at a fairly high quality. In this way the data could all be calibrated to the C 1s peak if any drift in the photon energy occurred.

Other scans were taken whenever unexpected peaks were observed in the data, focussing with high resolution on these areas, but upon review of this second set of data, any features were found to be inconsistent and attributed to noise in the data.

5.4 Results and Discussions

Full range scans of the Pt/C surface are shown in figure 5.10. Because beamline 1.1 is an entrance slitless monochromator the photon energy can drift with source position. In order to compensate for this all spectra are calibrated to the carbon 1s peak at 285 eV.

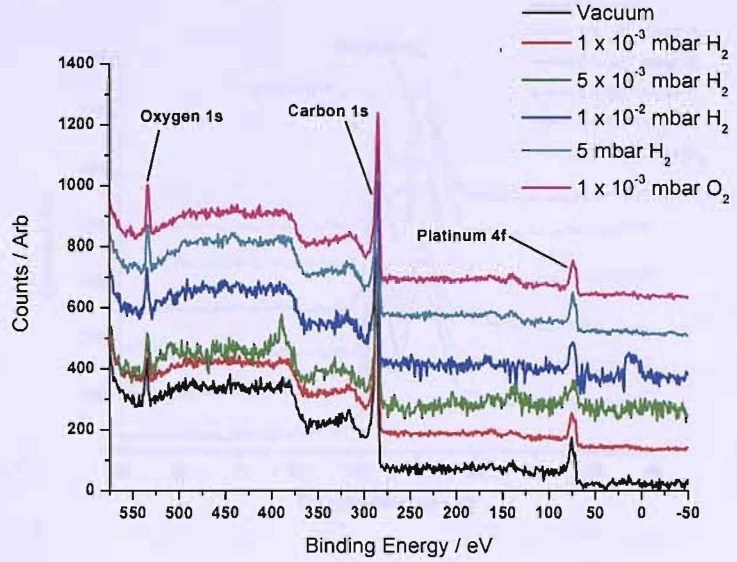

Figure 5.10 – 5 coadded and averaged XPS scans of 20 wt % Pt/C on Al, hυ 650 eV, FAT 90 eV, step size 1.0 eV, scans offset for clarity

The features seen at a binding energy of 130 and 360 eV at 5 x 10^{-3} mbar H$_2$ and 10 eV in 1 x 10^{-2} mbar H$_2$ were not present during a second set of scans and as such can be discounted as noise. All the expected features of the sample are seen within this data, the main feature to notice is the quality of data obtained in 1 x10^{-3} mbar of either gas is of comparable quality to those obtained in vacuum, however at pressures above this level the data quality suffers somewhat.

Figure 5.11 shows higher quality data with scans focussed on the platinum 4f peaks, these sets of data were collected at the same time as scans covering the C 1s region (not shown) allowing all data sets to be calibrated. Data quality was improved by using a smaller energy range allowing the step size to be reduced, reducing the pass energy (FAT), and collecting a higher number of scans due to the overall collection time being reduced.

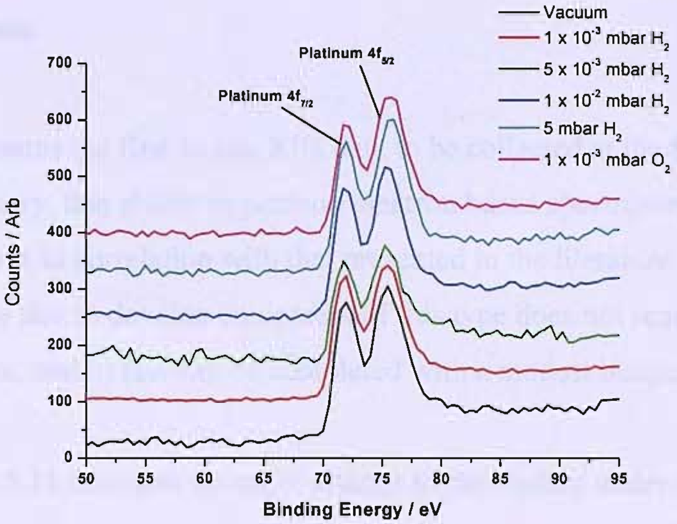

Figure 5.11 – 20 coadded and averaged XPS scans of 20 wt % Pt/C on Al, hυ 450 eV, FAT 44 eV, step size 0.5 eV, scans offset for clarity

From this data it was hoped that slight shifts in the position of the platinum 4f peaks would be detectable, however this does not appear to be the case. The data quality of these 4f peaks may have been compromised by the use of aluminium as the backing plate for the sample. The Pt 4f peaks are expected at BE = 71 and 75 eV, whereas the Al 2p peaks would be seen as a very tight doublet around BE = 73 eV [19]. However if the presence of Al was a major issue one would also expect to see signs of the Al 2s peak around 118 eV [20], there are no indications of this in the data shown in figure 5.10.

Another issue with the data presented which may have limited any observed effects is the resolution of the spectra, it was not possible to obtain reasonable data using a lower pass energy (higher resolution), due to insufficient photon flux on beamline 1.1. However, beamtime was not available on the undulator beamline 5U for these initial trial experiments.

5.5 Conclusions

This chapter presents the first *in situ* XPS data to be collected at the SRS at Daresbury laboratory, this ability to perform electron based spectroscopy at more realistic pressures is in correlation with that presented in the literature. Specifically this chapter shows that to develop equipment of this type does not require funding in six figures or more, and in fact can be completed with a modest budget.

Although figure 5.11 indicates no major change to the surface under the high pressure of hydrogen or oxygen, the mere fact a spectrum was obtainable means the HAPPY system is functional.

At the time of experimentation a number of problems existed with the HAPPY system, however, many of these had straight forward solutions. The maximum pressure obtained during these experiments was still short of what was desired, with the addition of larger pumps a steeper pressure gradient could be obtained. This also lowers the base pressure of the chamber and with the addition of a new manipulator designed to allow heating at high pressures, means the HAPPY chamber is now well equipped for UHV based experiments as well.

The data quality obtained during these experiments was below the standard seen in the literature for other *in situ* XPS systems. To increase the number of electrons reaching the detector a set of Helmholtz coils were specifically designed for the experimental chamber, these effectively neutralise any magnetic fields present in the working area which may cause the electrons to deflect away from the detector. Also the source quality could be improved, by using a beamline with a higher flux than found on 1.1.

The new HAPPY system, shown in figure 5.12, illustrates a few of these changes. An XPS experiment investigating the oxidation of copper had been scheduled which would have been able to test these improvements, unfortunately as the beamtime approached the SRS system suffered a water leak and was closed down for repairs.

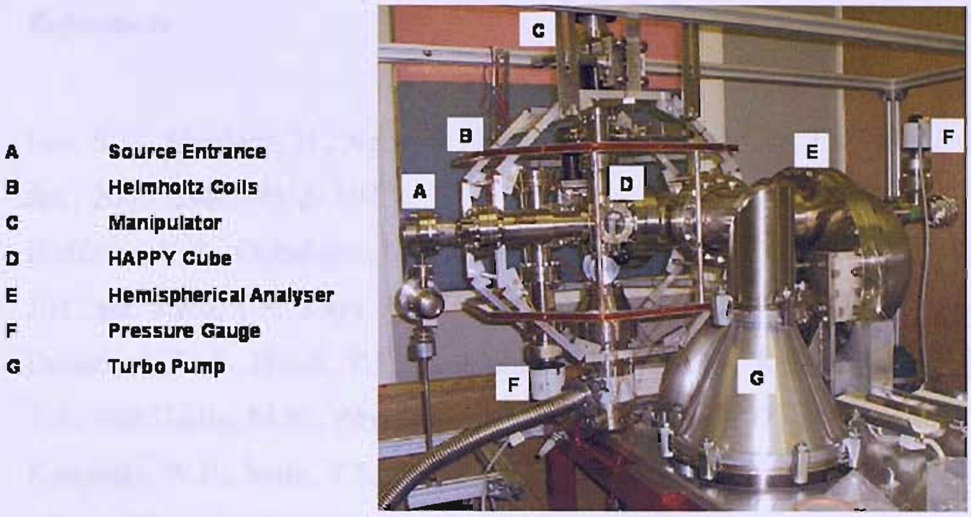

Figure 5.12 – Current setup of the HAPPY system (01-07)

A beamtime application was submitted by Lindsay *et al.* to investigate the exposure of TiO_2 to H_2O on beamline 5U using the HAPPY system. This application was successful, with the improvements made on the chamber and the opportunity of using an undulator beamline, resolutions of < 1 eV were obtained. The group found they could detect the presence of water on the surface of the TiO_2 separately to the O 1s peak [21]. It is highly unlikely that without the preliminary data presented in this chapter that the applications for extra funding for further modifications and for the beamtime on 5U would have been approved.

A new lens system is currently being developed for the chamber, if successful, this will allow another stage of pumping leading the way to higher accessible sample pressures. Also distance between the sample and opening aperture for the detector is likely to be reduced, which should reduce the number of lost electrons and further improve the quality of the data.

Future work had been planned to use the HAPPY system to investigate the oxidation and reduction of a Cu(100) crystal, to support the RAIRS work presented in Chapter 4. Unfortunately due to a number of difficulties experienced by the SRS system during the latter stages of this Ph.D., combined with the added restrictions associated with the scheduled shutdown of the SRS, this work was not possible.

5.6 References

1. Lee, S.Y., Mettlach, N., Nguyen, N., Sun, Y.M., and White, J.M., *Appl. Surf. Sci.*, 2003. **206**(1-4): p. 102.
2. Hoffman, K.R., Dababneh, M.S., Hsieh, Y.F., Kauppila, W.E., Pol, V., Smart, J.H., and Stein, T.S., *Phys. Rev. A*, 1982. **25**(3): p. 1393.
3. Dababneh, M.S., Hsieh, Y.F., Kauppila, W.E., Kwan, C.K., Smith, S.J., Stein, T.S., and Uddin, M.N., *Phys. Rev. A*, 1988. **38**(3): p. 1207.
4. Kauppila, W.E., Stein, T.S., Smart, J.H., Dababneh, M.S., Ho, Y.K., Downing, J.P., and Pol, V., *Phys. Rev. A*, 1981. **24**(2): p. 725.
5. Lin, T.H., Huang, T.P., Liu, Y.L., Yeh, C.C., Lai, Y.H., and Hung, W.H., *J. Phys. Chem. B*, 2005. **109**(29): p. 14079.
6. Herceg, E., Jones, J., Mudiyanselage, K., and Trenary, M., *Surf. Sci.*, 2006. **600**(19): p. 4563.
7. Jiang, Z.Q., Huang, W.X., Tan, D.L., Zhai, R.S., and Bao, X.H., *Surf. Sci.*, 2006. **600**(21): p. 4860.
8. Alderucci, V., Pino, L., Antonucci, P.L., Roh, W., Cho, J., Kim, H., Cocke, D.L., and Antonucci, V., *Mater. Chem. Phys.*, 1995. **41**(1): p. 9.
9. Granger, P., Dathy, C., Lecomte, J.J., Leclercq, L., Prigent, M., Mabilon, G., and Leclercq, G., *J. Catal.*, 1998. **173**(2): p. 304.
10. Riguetto, B.A., Damyanova, S., Gouliev, G., Marques, C.M.P., Petrov, L., and Bueno, J.M.C., *J. Phys. Chem. B*, 2004. **108**(17): p. 5349.
11. Tseng, C.J., Lo, S.T., Lo, S.C., and Chu, P.P., *Mater. Chem. Phys.*, 2006. **100**(2-3): p. 385.
12. Zhao, D. and Xu, B.Q., *Phys. Chem. Chem. Phys.*, 2006. **8**(43): p. 5106.
13. Bluhm, H., Havecker, M., Knop-Gericke, A., Kleimenov, E., Schlogl, R., Teschner, D., Bukhtiyarov, V.I., Ogletree, D.F., and Salmeron, M., *J. Phys. Chem. B*, 2004. **108**(38): p. 14340.
14. Hirsimaki, M., Lampimaki, M., Lahtonen, K., Chorkendoff, I., and Valden, M., *Surf. Sci.*, 2005. **583**(2-3): p. 157.
15. Cocke, D.L., Schennach, R., Hossain, M.A., Mencer, D.E., McWhinney, H., Parga, J.R., Kesmez, M., Gomes, J.A.G., and Mollah, M.Y.A., *Vacuum*, 2005. **79**(1-2): p. 71.

16. Montano, M., Bratlie, K., Salmeron, M., and Somorjai, G.A., *J. Am. Chem. Soc.*, 2006. **128**(40): p. 13229.
17. Cardona, M. and Ley, L., *Photoemission in Solids. Vol. 1: General Principles*. Topics in Applied Physics, ed. M. Cardona and L. Ley. 1978, Berlin: Springer-Verlag.
18. Turner, J.A., Thomas, K.M., and Russell, A.E., *Carbon*, 1997. **35**(7): p. 983.
19. Kammerer, R., Barth, J., Gerken, F., Kunz, C., Flodstrom, S.A., and Johansson, L.I., *Phys. Rev. B*, 1982. **26**(6): p. 3491.
20. Briggs, D. and Grant, J.T., *Surface Analysis by Auger and X-Ray Photoelectron Spectroscopy*. 2003, Chichester and Manchester: IM Publications and Surface Spectra Limited.
21. Bailey, L., Purton, J., Siggel-King, M.R.F., Surman, M., Hearn, C., and Lindsay, R., *To be published*, 2007.

Chapter Six – Conclusions

6.1 Experimental Conclusions

The aim of this thesis was to develop experimental methods which bridge the 'pressure gap' often suffered by traditional ultra high vacuum surface science experiments. Two new pieces of equipment have been brought to a stage where they are now available to the scientific community as shown by the use of HAPPY by Lindsey *et al.* to investigate water on TiO_2 [1]. Both of these new systems offer UHV quality cleaning and electron based techniques combined with additional experimental techniques at higher pressures; 200 mbar for RAIRS experiments in the HPRC and XPS up to 1×10^{-2} mbar in the HAPPY system.

Although no change in the catalyst under investigation was observed, using the HAPPY system, during the exposure of the Pt/C to 1×10^{-2} mbar pressures of both H_2 and O_2, these were the first experiments in the country to obtain XPS measurements at such high pressures. The proof of this achieved potential, enhanced proposals for further funding for additional development and beamtime. The peripatetic nature of the system raises the appeal of HAPPY yet further, enabling different beamlines to be used and extending its lifespan far beyond that of the soon to be closed SRS.

The overall cost incurred in developing the HAPPY system to its current level, which is now beyond that presented in this thesis, is far below that spent on developing other systems currently being used elsewhere in the world [2, 3]. This is encouraging and shows that once a system has originally been shown to work, similar equipment can then be produced at greatly reduced cost, as much of the refinement has already taken place, allowing the technique to then become available to a far wider range of people.

The data obtained *in situ* for the oxidation of copper presented in this thesis is consistent with data previously reported in the literature. When copper is exposed to high pressures of oxygen, oxidation begins to occur at fairly low temperatures, 328 K, initially forming a layer of Cu_2O indicated by a peak around 650 cm^{-1} in the data presented. With a reasonable exposure time at lower temperatures the thickness of the Cu_2O layer increases and eventually this changes the appearance of the far-IR spectra. Above a certain thickness, a second peak around 600 cm^{-1} begins to appear and as the thickness grows this peak starts to dominate and the initial peak at 650 cm^{-1} reduces in intensity, as predicted by Greenler *et al.*[4]. The peaks are assigned as the TO mode of the F_{1u} vibration at 650 cm^{-1} and the LO mode of the same vibration at 600 cm^{-1} in accordance with the data published by Lenglet *et al.*[5].

At temperatures above 500 K the preferential form of the oxide becomes CuO, indicated by a broad feature between 400 and 500 cm^{-1}. As in previous reports it is difficult to pinpoint the exact positions of each vibrational mode due to the broad nature of this feature. However, a small peak around 320 cm^{-1} can be attributed to the A_{2u} vibration with certainty, in accordance with the literature [6]. Within the broad feature itself a number of bands can be tentatively assigned with assistance from the literature. A peak in the region 360-400 cm^{-1} is seen in both sets of data obtained for the extreme oxidation, discussed in sections 4.4.1.1 and 4.4.1.2. On comparison to work presented by Kuz'menko *et al.*[7], this band can be attributed to the A_{3u} vibrational mode. However, it is worth noting many other authors report detecting this mode at higher wavenumbers, the maximum being reported as 478 cm^{-1} [6]. In the literature the B_{2u} mode is reported between 470 and 530 cm^{-1}. From the data presented here it seems reasonable to assume the peaks appearing towards the bottom end of this range, 450 – 490 cm^{-1}, are attributable to this vibrational mode. The final mode expected within the range investigated in this thesis has, once again, been detected over a very wide range 522 – 590 cm^{-1}, it is also regularly shown as a shoulder to the main broad feature which dominates the CuO spectrum. In the data presented here the band appearing between 580 and 610 cm^{-1} has been assigned to the presence of a thick layer of Cu_2O and this does not leave another obvious feature in the spectrum unassigned. However, in figure 4.17 a potential peak at 500 cm^{-1} is discussed and in figure 4.26 a shoulder around 515 cm^{-1} is apparent. If these were assigned to the B_{3u} mode sitting in the lower range of reported wavenumbers this would be consistent with the other assigned ranges.

Data obtained in this work indicates why the assignment of the peak positions of the four vibrational modes A_{2u}, A_{3u}, B_{2u} and B_{3u} has been so difficult in the past. In figures 4.25 and 4.27 the presented data show the shifts in peak positions when the oxide layers have either been allowed to cool in the presence of oxygen, or having been heated in Ar in order to collect consistent background data files for the next experiment. Shifts as large as 20 cm^{-1} are observed, these can only be attributed to changes in structure either due to further oxidation or slight reduction of the oxide layer. If minor changes such as these can change the peak position so much, then it is unsurprising that entirely different experiments run by different groups will also lead to large inconsistencies in the data presented.

The reduction experiments performed in this thesis are consistent with data shown in the literature for CuO. Under a strong flow of 5 % CO/He, a CuO catalyst was found to reduce directly to Cu around 473 K [8], in the work presented here the oxide layer was reduced in 200 mbar O_2 to Cu by 465 K. Under a reduced flow of CO the authors found signs of Cu_2O formation as an intermediate stage during the reduction, unsurprisingly no such signs were observed with the much greater reducing atmosphere applied here.

In the literature the reduction of Cu_2O is generally considered more difficult than CuO and occurs at higher temperatures [9]. In the data presented in this thesis, the reduction of the surface appears to occur as one step, i.e. once the sample reaches a certain temperature the entire oxide layer was reduced with no clear preference to either oxide form. It is worth arguing that many reduction experiments are performed on pure samples of powdered CuO or Cu_2O, as opposed to the grown oxide discussed here. Nagase *et al.*[9] published findings that suggest the 'history' of a sample had an effect on the ease of reduction. An 'as new' sample of Cu_2O was found to be resistant to CO reduction up to 623 K, however once the sample had been oxidised to CuO, reduced and then reoxidised to Cu_2O, reduction in CO began to occur around 523 K. This would suggest that grown layers of Cu_2O do reduce easier than powdered or single crystal samples, consistent with the finding presented here. The relative strengths of reducing atmosphere may also have played a large part.

The first DFT calculations of the phonon modes of Cu_2O and CuO are presented in this thesis and appear quite consistent to the experimental data presented both here and in the literature, especially for Cu_2O. With reference to an IR spectrum collected in an electrochemical environment by Melendres *et al.* [10] these calculations raise a strong argument regarding two of the three peaks assigned to the presence of Cu_2O. The DFT results presented in this thesis confirm a fundamental IR active phonon present around 630 cm^{-1}, however there are no phonons calculated around 790 and 1110 cm^{-1}, and the origins of these assigned peaks should be placed in doubt.

The calculations performed for CuO do not appear as reliable as those shown for Cu_2O. This can be attributed to the need to consider electron spin when defining the unit cell of the compound. This created a more complex unit cell than would normally be required for an entirely structural prediction of the spectral properties of CuO. Limited conclusions can be raised from the results aside from confirming the presence of the three Raman and six infrared active modes presented by Kliche and Popovic [6]. If it was possible to calculate the relative intensities of the various phonons this might give some insight into the accuracy of the calculated peak positions in reference to experimental data.

The results presented in this thesis clearly indicate the successful development of the high pressure reaction cell. Due to the ease of manipulation afforded by the additions of a nose cone and view ports to the original design, a sample's environment can be changed from UHV, and the ability to clean the sample, to 200 mbar of gas, where upon background and experimental scans can be obtained, in around five minutes. This possibility greatly reduces the risk of any contamination of the surface which may occur. The combination of an oxygen tolerant button heater and platinum resistance thermometer, appears to be highly robust and produces repeatable high performance levels allowing confidence in the accuracy of the data collected. Although not investigated within the scale of this thesis there would be no apparent reason why the system could not be used at intermediate pressures between UHV and 200 mbar, if desired, as long as backgrounds are collected at the same gas pressure.

One problem with the current HPRC design which has been revealed in this thesis is the inability to investigate the effect of high pressures of CO at elevated temperatures without contamination of $Fe(CO)_5$. To solve this issue a new, less reactive, sample stage could be made, potentially out of molybdenum, although this would be quite expensive, or alternatively a different reducing agent could be used such as H_2, with appropriate safety measures implemented.

6.2 The Future of Synchrotron Far-IR RAIRS

Whilst the applications for the HAPPY system are immediate and far reaching, in line with other *in situ* XPS systems developed in recent years, the use for SR far-IR RAIRS remains of limited appeal. So with the closure of beamline 13.3 at Daresbury Laboratory and no far-IR beamlines currently planned for Diamond or Soleil, what does the future hold for SR far-IR RAIRS?

The information afforded by the combination of synchrotron radiation with the RAIRS technique has in the past provided useful insight into crystal/adsorbate systems as discussed in the introduction chapter to this thesis. However these pieces of data could only ever be obtained with a slice of fortune, when a number of factors all worked in favour.

As the UHV chamber used in the SR-RAIRS experiments is permanently attached to a synchrotron ring this means that access is limited to set periods of beamtime. There are a number of standard surface science difficulties which many beamlines based on a synchrotron source can suffer from. In order to obtain UHV conditions a bake out is required which generally takes over 24 hours, if something within the chamber itself breaks, for example the filament on the ion gauge or quadrupole mass spectrometer, the vacuum needs to be broken to fix the problem before the system is evacuated and baked again. This in itself can cause difficulties, if a sample is particularly reactive and previously unused, then potentially the length of time spent cleaning the sample can use up a large proportion of the allotted time. If the sample then needs to be removed between beamtime allocation periods this cleaning process would then need to be repeated, continually eroding potential experimentation opportunities. This difficulty prevented possible UHV and subsequent HPRC work to be carried out on a ruthenium crystal concerning the oxide layer which forms a highly active catalytic surface discovered by Peden *et al.*[11], which was one of the original target experiments for this Ph.D.

In the case of beamline 13.3 it has been built above the synchrotron ring, in order to save floor space, possible because the quality of the IR light is largely unaffected by a vertical manipulation. At the SRS at Daresbury laboratory this causes a problem, whenever the beam is injected into the storage ring, radiation levels reach potentially unsafe limits on the station. This means the beamline must be evacuated before refill can occur, depending on the lifetime experienced by the storage ring this can happen between one and three times a day. If everything goes to plan these refills last one hour and are all that are needed, however this is not always the case as sometimes the beam is lost and occasional issues during reinjecting can be experienced. Obviously these issues affect all users of the SRS, however the added issue of being unable to access the station during these periods to prepare a sample for experiments, disadvantages users of far-IR beamlines further.

When the SRS was built it was a state of the art facility, as time has passed the technology and equipment used has been superceded, indicated by the UK Government's decision to close the SRS and replace it with the Diamond light source. As the age of the machine has increased, unsurprisingly the reliability of many parts of the system has decreased leading to some extended repairs over the time period covered by this thesis. Although access to the 13.3 beamline was not restricted during much of the repair work, the lack of a primary source hindered potential research, it was during these periods that a globar source was used instead of synchrotron light.

One of the major advantages listed for RAIRS is the sensitivity which enables the detection of very small peaks which may appear in the spectral region for monolayer systems. Baily *et al.*[12] observed the lifting of the (1 x 2) reconstruction of the Pt(110) surface by exposure to CO, this involved monitoring peaks as small as 0.05 %. This required sensitivity means that after an extended shutdown the beam quality is of a level where, whilst it is useful for other stations, it is largely unusable for far-IR RAIRS. As such, an extra week or two is required to allow the beam to improve before experiments can be performed. Despite these additional periods it is clear, looking at the data in this thesis, that the experiments performed on Pt(110) would not have been repeatable under the conditions experienced. Using the synchrotron source the lowest peak-to-peak noise ratio obtained in this thesis was approximately 0.15 %, and whilst not massively detrimental to the data collected in this thesis, makes a number of other potential experiments unviable.

Interestingly, the sensitivity afforded by RAIRS provided evidence of potential problems on the SRS itself before the operators or any other users were aware of them. At the time of collection of the first set of data presented in this thesis the peak-to-peak noise ratio was noticeably worse than previously experienced on the beamline. When the interferogram was inspected there was a large oscillating feature detected shown in figure 6.1 where the black interferogram was collected during the first set of data presented in the thesis and the red one during the second set.

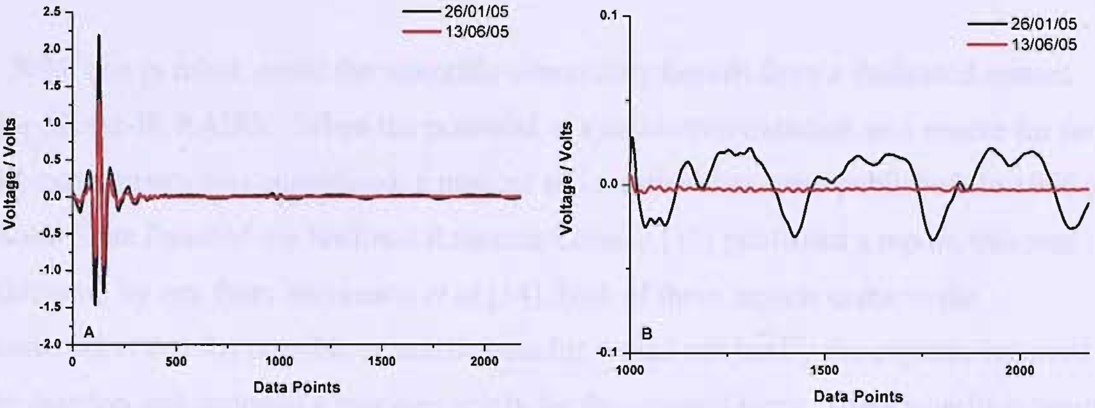

Figure 6.1 – Interferogram showing the presence of an oscillating feature

The two interferograms were collected under slightly different conditions; the black with 5.12 cm s^{-1} mirror velocity, 512 co-added scans, 179.2 mA ring current and the red with 3.16 cm s^{-1} mirror velocity, 256 co-added scans, 208.4 mA ring current, both were obtained in 200 mbar of Ar. In figure 6.1A it can be seen that the red interferogram is of lower intensity, most likely due to the differing conditions, with reference to figure 6.1B it is clear that this does not account for the major difference in the plots. From the interferogram collected in January 2005 there is an obvious oscillating pattern to the noise observed, this effect had gone almost entirely unnoticed by both the operators and the users, only users on other IR beamlines experienced difficulties with unexplained high noise levels. With the evidence provided by beamline 13.3 investigations were undertaken into what caused the observed oscillation. These investigations involved changing the filling method of the

SRS and monitoring for any changes, eventually an RF power supply was found to be malfunctioning, causing the oscillation. It is worth considering that without the equipment on beamline 13.3 the issue may have taken much longer to be raised and a solution discovered.

The red interferogram shown in figure 6.1, whilst undoubtedly of better quality, still produced noise levels higher than those experienced by Baily *et al.*[12]. So whilst extreme conditions such as those illustrated by the black interferogram can pass largely unnoticed by other users of the SRS, even an interferogram which looks reasonable in comparison, as with the red plot, is still well below the ideal conditions for SR far-IR RAIRS, with all other users happy with the performance of the SRS.

With this in mind, could the scientific community benefit from a dedicated system for SR far-IR RAIRS? When the potential of synchrotron radiation as a source for far-IR experiments was considered, a number of investigations were published. In 1966 a Solid State Panel of the National Research Council [13] published a report, this was followed by one from Stevenson *et al.*[14], both of these reports came to the conclusion that the possible scientific benefits would not justify the expense incurred to develop and maintain a machine solely for far-infrared work. There is unfortunately no reason to believe that this conclusion has changed over intervening years. Meaning users of SR far-IR RAIRS will have to continue to live with the potential of extended periods where experimentation is either impossible or below desired capabilities, if the technique has any future at all.

Without synchrotron light sources, where would that leave far-IR RAIRS experiments? Before the advent of SR far-IR the only sources available were blackbody sources known as globars. The main benefits of synchrotron sources for far-IR RAIRS experiments over globars are a high flux and a low étendue which leads to high sensitivity and resolution, these benefits are discussed in more detail in section 2.3.3 in this thesis. All this seems rather damning for globar sources, however when comparing the data presented here a much lower noise level was observed for the globar source in comparison to the synchrotron data. This illustrates that if the SRS is not performing optimally then a globar source can at least be comparable at the higher end of the spectrum.

In figure 6.2 the single beam spectra of the globar and synchrotron sources are compared. This data illustrates another issue which arises from synchrotron sources, whilst the signal from a globar remains constant during experimentation, the signal from the synchrotron relates to the beam current of the machine as shown by the black plot obtained at 232.6 mA and the green collected at 196.8 mA. This means all data needs to be normalised to the beam current at which the data was collected before it can be compared properly.

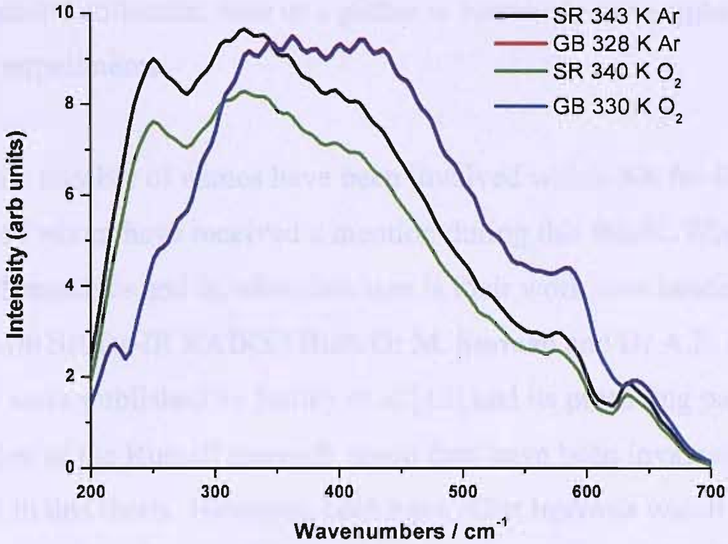

Figure 6.2 – Synchrotron (SR) vs. globar (GB) plots

Figures 6.2 shows the performance of the synchrotron source far out weighing that of the globar below 350 cm^{-1}, however, even at high beam current more signal is available from a globar source at the higher end of the spectral scale of interest.

As well as the signal at lower wavenumbers, another area where the globar fails to compete with the performance of the synchrotron is the experimental timescale. The data shown in this thesis was obtained in under ten minutes when using the synchrotron source, whereas for the globar the data took over an hour for each scan. These longer collection times could allow data to be affected by contamination leading to broader peaks observed in the data, potentially obscuring doublets or other close-set features.

If a synchrotron source did not allow for quicker data collection, it would never have been considered as a source for far-IR work as beamtime allocation periods would be too prohibitive and minimal research could be performed. However a globar source is much more affordable for individual scientific research groups, and could be attached to a dedicated UHV chamber taking up little more space than a medium sized room. With this in mind the entire setup could be obtained and available to two or three research groups, based in one place, and be available 24 hours a day, 7 days a week for sample preparation and experimentation. In a world where invariably time equals money, the extended collection time of a globar is seemingly outweighed by its availability for experiments.

Over the years a number of names have been involved within SR far-IR RAIRS research, most of whom have received a mention during this thesis. Where do these scientists find themselves and in what direction is their work now heading, are they still involved with SR far-IR RAIRS? Both Dr M. Surman and Dr A.E. Russell were involved in the work published by Bailey *et al.*[12] and its preceding paper [15], as the latest member of the Russell research group they have been invaluable during the work presented in this thesis. However, both have other interests which are starting to take a greater role in their lives; Dr. Russell is still greatly involved in fuel cell catalysis, but is also following investigations using surface enhanced Raman spectroscopy (SERS) [16], whereas Dr. Surman is one of the major contributors to the energy recovery linac prototype (ERLP) system based at Daresbury lab which is the fore-runner to the planned 4th generation light source (4GLS) [17]. Professor M. A. Chesters has in recent years been Director of Synchrotron Radiation at the SRS, has been involved in 4GLS and the research has seemingly shifted to standard RAIRS investigations [18]. Dr. Raval has continued working on the adsorption of more complex molecules to single crystal surfaces whist focussing more on the higher end of the infrared spectrum combining results with other surface science techniques [19, 20]. Mention should also be made to Dr. Hollins who sadly passed away during the time-span of this Ph.D.

Aside from the paper published from the work presented in this thesis [21], the most recent surface science research using far-IR was published by the Gardner group [22, 23]. This group also used beamline 13.3 at the SRS around the start of the work presented here, however it is worth noting that no applications for beamtime were submitted by this group for the final allocation period, suggesting that they have also changed the focus of their work.

So it seems that SR far-IR RAIRS has largely come to the end of its useful life, the benefits gained from the technique seem largely outweighed by the difficulty in obtaining peak performance results. In which case, aside from using a globar source, what other techniques are available for the detection of adsorbates?

High resolution electron energy loss spectroscopy (HREELS) is the immediately obvious technique for surface scientists seeking to replace far-IR when monitoring surface adsorbate vibrations. The technique involves firing a beam of monoenergetic electrons of a known energy, E_0, at a surface from an angle as shown in figure 6.3 and detecting the inelastically scattered electrons.

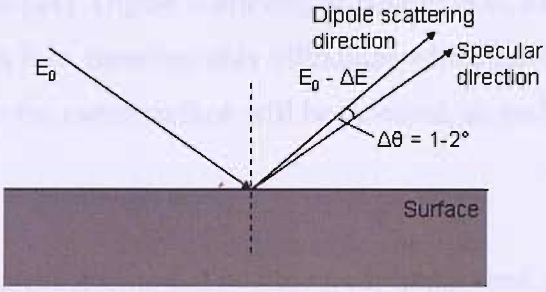

Figure 6.3 – The principle of EELS showing inelastically scattered electrons at a slightly off-specular direction

A very small proportion of the electrons impinging on the surface will be inelastically scattered, however, and using the loss of energy, the vibrational frequency, v_{vib}, can be calculated using equation 6.1.

$$\Delta E = h\nu_{vib} \qquad \textbf{6.1}$$

where h is Planck's constant

In order to be useful HREELS requires a resolution of 1-10 meV, which is much smaller than most electron based spectroscopy methods. A monochromator is used to focus minimise the energy range of the electrons, this range is a major factor in the resolution of the technique, many of the top range spectrometers can now obtain 8 cm^{-1} or better.

In figure 6.3 the scattered beam is shown at a slightly off-specular direction, this is due to conservation of momentum parallel to the surface. As the adsorbate molecules oscillate they create an electric field, interacting with the incoming electrons, this field is at its strongest when the molecules oscillate in phase. If the electrons were to reflect from the surface with no interaction from the adsorbates, parallel kinetic energy would be conserved and the electrons would be reflected in the specular direction. However with dipole scattering where a strong interaction is observed, there is a small energy transfer as shown in eqn 6.1, in order to conserve momentum parallel to the surface this is observed as a slight decrease in the scattering angle, in relation to the normal, of the electrons [24]. Dipole scattering in HREELS is, like RAIRS, affected by the surface selection rule, meaning only vibrations which have an oscillating dipole perpendicular to the metal surface will be detected, as such, this simplifies the spectra obtained.

Two other scattering mechanisms can be observed; impact and negative ion resonance scattering. Impact scattering involves collisions of the electrons with adsorbed species, whilst obeying selection rules different to the dipole scattering discussed above. Peaks detected on an off-specular angle can provide information regarding adsorbate structures. Negative ion resonance scattering involves electrons becoming trapped in the molecular orbitals. Upon ejection the electrons are found to have taken on characteristics of the orbital in which they were trapped.

As HREELS is electron based, in order to perform experiments at a more realistic pressure, a system more akin to the HAPPY chamber would need to be developed as opposed to the HPRC. However, unlike photoelectron spectroscopy in HAPPY, the activating species in HREELS is also an electron and therefore highly affected by the surrounding pressure before, as well as after, hitting the sample which would make a system very difficult to design.

Another technique used for the detection of an adsorbate at a surface is Raman spectroscopy. When the oscillating electric field associated with a photon interacts with a molecule a small dipole moment is induced through the polarisability of the molecule. The oscillation of this dipole will be at the same frequency as the exciting photon. This in turn releases light with the same oscillation, but not necessarily in the same direction as the original photon was travelling, this is termed Rayleigh scattering and is shown in figure 6.4a.

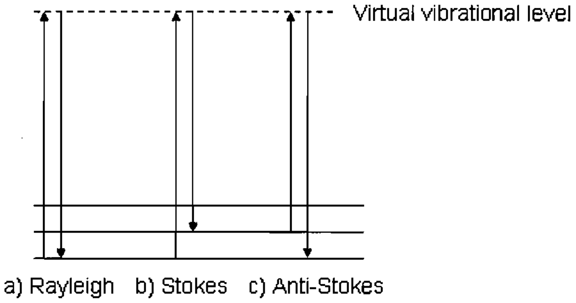

Figure 6.4 – Excitation and relaxation of electrons via a photon, leading to the Raman effect

The molecules under observation are also vibrating, these vibrations correspond to normal modes of motion, the frequencies of which can interact with the incoming photon and produce scattered radiation. This radiation will be shifted from the Rayleigh scattered radiation and is known as Raman scattering. Two types of Raman scattering are known; one to longer wavelengths, known as Stokes scattering, and one to shorter wavelengths, known as anti-Stokes scattering, as shown in figures 6.4b and c respectively.

Raman scattering occurs much less frequently than Rayleigh scattering, in fact only about 1 in 10^7 incident photons are actually scattered, this combined with the small deviations observed demands the use of intense monochromatic sources (i.e. lasers). Even with these sources the Raman signal remains very weak, however, two techniques have been developed to increase the signal; resonant Raman spectroscopy and surface enhanced Raman spectroscopy.

Resonance Raman spectroscopy (RRS) occurs when the energy of the exciting photon is approximately equal to an electric dipole allowed transition of the molecule in question.

Surface enhanced Raman spectroscopy (SERS), discovered by Fleischmann [25] in the 1970s, occurs on roughened surfaces leading to an enhancement of the Raman signal, which was originally assigned to the increased surface area, this has since been dismissed [26]. Instead two other potential theories have been proposed to explain the enhancement; chemical enhancement or electromagnetic enhancement.

The chemical enhancement model attributes the enhancement to interactions between the adsorbed molecule and the metal surface, effects of orientation, coverage of the adsorbed molecules and surface structure are included within the model. The intensity of the signal observed from the chemical enhancement model depends on the charge transfer state mechanism in action. The transfer is proposed to occur due to a slight overlap of the molecular energy levels of the adsorbate with the conduction band of the metal. The enhancement is predicted to be more effective when the surface is rough, as the peaks in the film provide a route for the hot electrons to reach the adsorbed molecule [27].

The electromagnetic enhancement theory involves the change in the local electric field of the adsorbed molecule, enhancement of this field is caused by the local electromagnetic field at the metal surface. If the wavelength of the incident light is comparable to the plasma wavelength of the metal surface, conduction band electrons can be excited to a state called a surface plasmon resonance. Molecules close to these resonances experience a large electromagnetic field, vibrational modes normal to the surface being especially enhanced.

The electromagnetic enhancement is discussed in much more detail by Moskovits [28] where the author shows that most of the properties observed in SERS are attributable to this enhancement. The author does concede that not all properties can be attributed to this enhancement and proposes that a combination of the electromagnetic and chemical enhancements exist.

Raman spectroscopy is a photon based technique and as such, it lends itself well to *in situ* measurements. Raman is non-invasive and is also unaffected by the presence of liquid water. However, RRS is only applicable in a certain number of cases when the laser light is tuned appropriately for the adsorbate, there are also large problems with fluorescence affecting the background. SERS on the other hand only occurs on certain metals, and to differing levels depending on this metal. These substrates also require a roughened surface, discounting the opportunity to work on specific adsorption sites. Originally the surfaces were electrochemically roughened electrodes, which have a random surface structure. However, recently efforts have been made to try and construct reusable SERS active substrates with much better defined surfaces, to a repeatable level of quality [29, 30]. Due to the required structure of the substrates it would not be possible to clean the surfaces to a UHV compatible level.

As discussed briefly in this thesis, XPS systems can detect the presence of an element at a surface even at very low level concentrations. At high resolutions it is possible to distinguish the same species adsorbed at different sites due to its peak position. Whilst traditionally a UHV technique, with specially designed equipment, such as HAPPY presented here, it is possible to record spectra under more realistic pressures. A drawback with XPS can be found when using more complex adsorbates as it can be difficult to conclude what species are present and how they are bonded to the surface.

Although it seems that no other technique quite matches the qualities of SR far-IR RAIRS; the ability to perform experiments in UHV and real world conditions with minimal modification, high sensitivity and easily interpreted data on adsorption sites and species; the difficulty in obtaining these conditions outweighs the benefits. With the other techniques mentioned above, combined with other widely available experimental techniques, data which provides the same conclusions is more easily obtainable. As such an end to this type of spectroscopy seems inevitable, leaving globar sources to be used as the major source for far-IR spectroscopy, despite its shortcomings between 200 and 400 cm^{-1}.

6.3 Terahertz Radiation

Terahertz radiation is defined as the frequency region 0.1 to 10 x 10^{12} Hz, it has been found to be one of the most difficult regions to create, falling as it does inbetween the electronic and photonic sides of the electromagnetic spectrum as shown in figure 6.5. Using optical sources, a normal 1400 K black body source will only provide nanowatts of power over the THz region due to Planck's radiation law. Regarding electronic sources, the power supplied by oscillators decreases as the frequency increases.

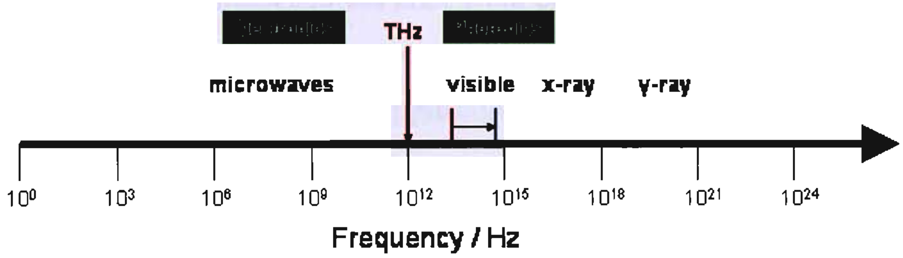

Figure 6.5 – The electromagnetic spectrum

However the terahertz region is not as unknown as the picture painted may suggest, in fact, given more suitable units it can be seen that the top end of the range has already been discussed in this thesis, as the terahertz region is in fact equivalent to 3 – 330 cm^{-1}. It has been mentioned previously that the emmitance of the SRS is highest at 100 cm^{-1} and drops off at higher wavenumbers in the infrared, the lower limit is present due to the diffractive splitting of the beam.

A number of different lab sources exist for THz experimentation, however these are generally found to produce very low power. Photoconductive emitters can produce broadband THz radiation with an average power of 40 μW [31], the emitters are generally made from semiconductors with small effective electron masses, due to rapid photocurrent rise and decay times. The sources are activated by the creation of an electron hole pair using an ultrafast laser pulse, which has a photon energy larger than the bandgap. These free carriers accelerate in the static bias field, creating a transient photocurrent which emits terahertz radiation. Due to this the maximum bias applicable to the material is also an important factor to consider [32]. Optical rectification can also be used as a method to produce broadband terahertz radiation, although producing lower power output than photoconductive emitters, they often provide much higher bandwidths [33]. Optical rectification works by the inverse of the electro-optic effect, the energy of the THz radiation comes directly from the ultrafast laser pulses used for excitation. The important properties to consider for the suitability of a material as a source are its non-linear coefficient and phase-matching conditions [32].

Narrowband THz sources are also available for the lab, these are often used for high-resolution spectroscopy. Most sources arise from extensions of the range of microwave oscillators, such as voltage-controlled oscillators and dielectric-resonance oscillators. Gas lasers also find some applications as narrowband THz sources, although they provide quite high power outputs, they generally require large cavities at low pressure and kilowatt power supplies. A few optical techniques have also been developed to produce terahertz radiation, one method involves the non-linear photomixing of two laser sources. The two sources interfere, resulting in output oscillations at the sum and difference of the two laser frequencies, the second of these can be designed to appear in the THz region.

Lab sources generally struggle to produce THz radiation above 1 mW, with optical methods generally more powerful than their electronic counterparts. Thus, in this case it is not so hard to understand why the region has not been investigated too deeply. More powerful sources are available however, via the use of modified synchrotrons. Coherent synchrotron radiation (CSR) occurs when very short electron bunches are fired around a synchrotron ring, if the bunch length of the electrons is shorter than the wavelength CSR is emitted, this can lead to a huge increase in power even when using modest currents. The power output from incoherent synchrotron radiation, i.e. that which is produced by a standard synchrotron set up, is proportional to the number of electrons in a bunch, N, whereas in CSR the power is proportional to N^2. One of the first reports discussing CSR as a source for THz radiation was published by Carr *et al.*[34] the authors presented data showing the power output of three systems; the Jefferson Laboratory energy recovery linac (ERL), the NSLS VUV ring at

Brookhaven National Laboratory and from a 2000 K thermal source, this is shown in figure 6.6.

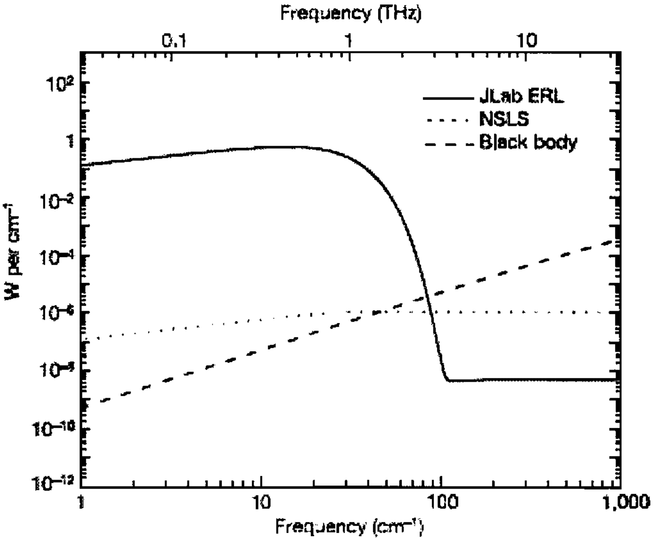

Figure 6.6 – Indicating the increased power output between CSR THz production and other traditional sources [34]

The calculations involved in producing the data shown above assumed the ERL to run at an average current of 3.7 mA, whereas the NSLS was assumed to run with a stored current of 800 mA. In the incoherent region this gives the NSLS 216 times the power per cm^{-1}, however in the terahertz region it is clear how much more power is provided by the ERL. The power output change between non-CSR and CSR occurs around 100 cm^{-1} and amounts to a factor of approximately 10^8. It has been found that the possible wavelengths for CSR bursting are limited by vacuum chamber shielding at an upper limit. The bunch energy spread can generate londitudinal “remixing” which can counteract the growth of the microbunching at shorter wavelengths [35]. With careful planning, future sources can be designed to minimise these issues and maximise stable coherent synchrotron radiation thanks to models described by Sannibale *et al.*[36].

CSR is more easily obtainable from free electron lasers (FEL) and energy recovery linacs (ERL) than the traditional synchrotron source such as the SRS at Daresbury laboratory.

FELs provide intense, powerful beams of laser light which can be tuned to a precise colour or wavelength, using an electron beam as the lasing medium instead of a gas or solid as used in more traditional lasers. FELs can absorb and release energy at any wavelength, because the electrons are freed of atoms, enabling the FEL to be controlled more precisely than conventional lasers and produce intense beams in brief bursts with extreme precision. Due to the absence of a lasing medium in the cavity the laser is able to operate at very high power levels without the usual cavity heating problems. The electrons pass through a linear accelerator (linac) before moving on to an insertion device, i.e. an undulator or wiggler, during which the electrons are oscillated in step, producing the coherent radiation desired. A number of FELs operate around the world, over a wide range of wavelengths, including DESY (Germany), iFEL (Japan), FELIX (Netherlands), CLIO (France) and JINR (Russia). The tunable nature of FELs also make them very appealing as compatriot sources to dedicated THz systems, in order to extend the range of experimentation wavelengths.

In an energy recovered linac, electrons are accelerated and passed through a loop, around this circuit the electrons pass through a number of insertion devices to produce coherent radiation. By the end of the circuit the electrons are 180 ° out of phase with the emerging electrons, the returning electrons pass back into the linac, where they are now decelerated and much of their energy recovered due to the phase shift, before the electrons are then dumped. In this manner continuous bunches can be sent out of the linac at a consistent charge, unlike a storage ring whose current decays over time. ERLs are a relatively new development with proposals currently underway at Cornell University (America), Novisibirsk (Russia), JAERI (Japan) and 4GLS/ERLP (UK). Many of these plan upgrades to combine the ERL with a FEL in a similar way to the JLab setup at Brookhaven. The predicted power output of the XUV FEL branch of 4GLS is shown in figure 6.7 combined with three points indicating the capabilities of the proposed far-IR FEL.

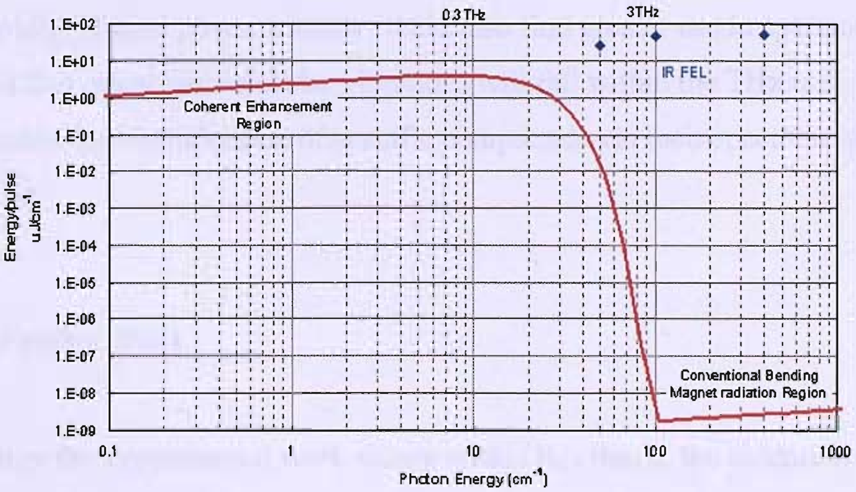

Figure 6.7 – Predicted energy per pulse for the XUV FEL and three photon energies for the far-IR FEL proposed for 4GLS [37]

As a relatively new avenue for scientific investigations it is clear that a wide range of work needs to be performed before the full extent of its abilities becomes obvious. With these new higher powered sources there may be signal to noise difficulties which will not become apparent until a number of investigations have been performed. Diagnostics of the beam will also be required, using a beam splitter in order to obtain samples of the beam in smaller pulses, which could give clearer data regarding the properties of these new sources.

Current knowledge of this previously elusive region of the electromagnetic spectrum is still small, but what is known offers encouragement for further development. All matter produces THz radiation to a very small degree, it is known that metals and water give off more than all other substances, this has led to detectors being constructed which offer the potential for detecting hidden metal or water samples [38]. Given that THz radiation can pass through all materials apart from metal and water but without the risk of ionisation it can also gain use in medical applications. It has been found that THz allows the detection of cancerous cells as well as early stages of tooth decay without the need for the shielding associated with X-rays. Although these applications are more suited for low power lab sources as opposed to the higher power sources discussed here, they give an idea for future work. It is known that 500 μW of THz power enables scanning of 1 cm^2 in 5 minutes [39], if a power source is able to reach closer to 100 W then the scanning process will be achieved much more rapidly. Higher power sources would also find greater use in spectroscopy, it is predicted that many biomolecular vibrations will fall within the THz region which could enable the identification of specific compounds via their spectroscopic fingerprint.

6.4 Further Work

To further the experimental work shown within this thesis, the oxidation of copper could be performed with the exposure time of the sample to the oxygen atmosphere closely monitored. This combined with a method to calculate the thickness of any layers formed would enable clearer conclusions regarding the surface composition especially surrounding the 650 cm^{-1} to 600 cm^{-1} band shift assigned to a layer of Cu_2O thicker than 4200 Å in accordance with Greenler *et al.*[4] as detailed in section 4.4.1.3.

It has been shown that with the current setup it is not possible to reduce a sample in the high pressure reaction cell using CO, due to contamination arising from the sample stage. Further work could be continued using H_2 as a reducing agent, with an appropriate safety system in place, or the sample stage, including any screws and nuts, could be changed from stainless steel to a less reactive material.

One of the fundamental aims of this thesis was to develop the HPRC and illustrate its capabilities, during this process however serious doubts have been raised over the time and effort expended in using SR far-IR RAIRS. Whilst this thesis concludes that the income does not exceed, or indeed, match the expenditure of the technique, except in fortuitous circumstances; this should not suggest the HPRC itself is looked upon unfavourably. There are no reasons why, with a few modifications, the HPRC setup could not be moved to a mid-IR setup elsewhere. Future work may also benefit from the ability to cool samples as well as heat them, although this would involve quite a large reworking of the lid and sample stage.

With the potential loss of SR far-IR RAIRS as an available technique, attention turns towards the emergence of high powered THz sources as a possible replacement.

Whilst still largely in its infancy, the technique shows a great deal of potential over a huge range of known and novel applications, which the scientific community should hope it fulfils and assist it where possible in its development.

The HAPPY system has been brought to a performance level which is competitive to that shown elsewhere in the world as indicated by the results obtained by Lindsey *et al.* investigating water on TiO_2 [1]. With further developments planned on the lens system, there seems no reason why the HAPPY system can not continue to help further wide-ranging *in situ* PES investigations. The closure of the SRS at Daresbury laboratory should have little impact upon the future use of the system, a benefit of its transportable nature.

6.5 References

1. Bailey, L., Purton, J., Siggel-King, M.R.F., Surman, M., Hearn, C., and Lindsay, R., *To be published*, 2007.
2. Ogletree, D.F., Bluhm, H., Lebedev, G., Fadley, C.S., Hussain, Z., and Salmeron, M., *Rev. Sci. Instrum.*, 2002. **73**(11): p. 3872.
3. Pantforder, J., Pollmann, S., Zhu, J.F., Borgmann, D., Denecke, R., and Steinruck, H.P., *Rev. Sci. Instrum.*, 2005. **76**(1).
4. Greenler, R.G., Rahn, R.R., and Schwartz, J.P., *J. Catal.*, 1971. **23**: p. 42.
5. Lenglet, M., Kartouni, K., Machefert, J., Claude, J.M., Steinmetz, P., Beauprez, E., Heinrich, J., and Celati, N., *Mater. Res. Bull.*, 1995. **30**(4): p. 393.
6. Kliche, G. and Popovic, Z.V., *Phys. Rev. B.*, 1990. **42**(16): p. 10060.
7. Kuz'menko, A.B., van der Marel, D., van Bentum, P.J.M., Tishchenko, E.A., Presura, C., and Bush, A.A., *Phys. Rev. B.*, 2001. **63**: p. Article 094303.
8. Wang, X.Q., Hanson, J.C., Frenkel, A.I., Kim, J.Y., and Rodriguez, J.A., *J. Phys. Chem. B*, 2004. **108**(36): p. 13667.
9. Nagase, K., Zheng, Y., Kodama, Y., and Kakuta, J., *J. Catal.*, 1999. **187**(1): p. 123.
10. Melendres, C.A., Bowmaker, G.A., Leger, J.M., and Beden, B., *J. Electroanal. Chem.*, 1998. **449**(1-2): p. 215.

11. Peden, C.H.F., Goodman, D.W., Weisel, M.D., and Hoffmann, F.M., *Surf. Sci.*, 1991. **253**(1-3): p. 44.
12. Baily, C.J., Surman, M., and Russell, A.E., *Surf. Sci.*, 2003. **523**(1-2): p. 111.
13. Brown, F.C., Hartman, P.L., Kruger, P.G., Lax, B., Smith, R.A., and Vineyard, G.H., *Synchrotron Radiation as a Source for the Spectroscopy of Solids*. 1966, NRC Solid State Panel Subcommittee Rep.
14. Stevenson, J.R., Ellis, H., and Bartlett, R., *Appl. Opt.*, 1973. **12**(12): p. 2884.
15. Surman, M., Hagans, P.L., Wilson, N.E., Baily, C.J., and Russell, A.E., *Surf. Sci.*, 2002. **511**(1-3): p. L303.
16. Cintra, S., Abdelsalam, M.E., Bartlett, P.N., Baumberg, J.J., Kelf, T.A., Sugawara, Y., and Russell, A.E., *Faraday Discuss.*, 2006. **132**: p. 191.
17. Flavell, W.R., Seddon, E.A., Weightman, P., Chesters, M.A., Poole, M.W., Quinn, F.M., Clarke, D.T., Clarke, J.A., and Tobin, M.J., *J. Phys.: Condens. Matter*, 2004. **16**: p. S2405.
18. Fiorin, V., McCoustra, M.R.S., and Chesters, M.A., *J. Phys. Chem. B*, 2004. **108**(30): p. 10981.
19. Chalker, S., Haq, S., Birtill, J.J., Nunney, T.S., and Raval, R., *Surf. Sci.*, 2006. **600**(11): p. 2364.
20. Fustin, C.A., Haq, S., Wingen, A., Gregoire, C., Raval, R., Dumas, P., Hannam, J.S., Leigh, D.A., and Rudolf, P., *Surf. Sci.*, 2005. **580**(1-3): p. 57.
21. Quin, D., Russell, A.E., Pere-Laperne, N., Patel, S., Lee, T., Flaherty, J., Burrows, I., Purton, J., and Surman, M., *Surf. Sci.*, 2006. **600**(18): p. 4260.
22. Pilling, M.J., Fonseca, A.A., Cousins, M.J., Waugh, K.C., Surman, M., and Gardner, P., *Surf. Sci.*, 2005. **587**(1-2): p. 78.
23. Le Vent, S., Pilling, M.J., and Gardner, P., *Surf. Sci.*, 2005. **587**(1-2): p. 150.
24. McCash, E.M., *Surface Chemistry*. 2001, Oxford: Oxford University Press.
25. Fleischmann, M., Hendra, P.J., and McQuillan, A.J., *Chem. Phys. Lett.*, 1974. **26**(2): p. 163.
26. Albrecht, A. and Creighton, C.G., *J. Am. Chem. Soc.*, 1977. **99**: p. 5215.
27. Kambhampati, P., Child, C.M., Foster, M.C., and Campion, A., *J. Chem. Phys.*, 1998. **108**(12): p. 5013.
28. Moskovits, M., *J. Raman. Spectrosc.*, 2005. **36**: p. 485.
29. Perney, N., Baumberg, J.J., Zoorob, M., Charlton, M., Mahnkopf, S., and Netti, C., *Opt. Express*, 2006. **14**: p. 847.

30. Mahajan, S., Abdelsalam, M., Suguwara, Y., Cintra, S., Russell, A., Baumberg, J., and Bartlett, P., *Phys. Chem. Chem. Phys.*, 2007. **9**(1): p. 104.
31. Zhao, G. and Schouten, R.N., *Rev. Sci. Instrum.*, 2002. **73**: p. 1715.
32. Ferguson, B. and Zhang, X.C., *Nature Mater.*, 2002. **1**: p. 26.
33. Bonvalet, A., Joffre, M., Martin, J.L., and Migus, A., *Appl. Phys. Lett.*, 1995. **67**(20): p. 2907.
34. Carr, G.L., Martin, M.C., McKinney, W.R., Jordan, K., Neil, G.R., and Williams, G.P., *Nature*, 2002. **420**(6912): p. 153.
35. Byrd, J.M., Leemans, W.P., Loftsdottir, A., Marcelis, B., Martin, M.C., McKinney, W.R., Sannibale, F., Scarvie, T., and Steier, C., *Phys. Rev. Lett.*, 2002. **89**(22).
36. Sannibale, F., Byrd, J.M., Loftsdottir, A., Venturini, M., Abo-Bakr, M., Feikes, J., Holldack, K., Kuske, P., Wustefeld, G., Hubers, H.W., and Warnock, R., *Phys. Rev. Lett.*, 2004. **93**(9).
37. Bowler, M.A., Surman, M., and Quinn, F.M. *THz output from 4GLS and ERLP Poster*. 2006.
38. Clery, D., *Science*, 2002. **297**(5582): p. 761.
39. Williams, G.P., *Rep. Prog. Phys.*, 2006. **69**(2): p. 301.

Appendix A: Full list of calculated phonons for CuO

Mode	Wavenumber / cm^{-1}	Mode	Wavenumber / cm^{-1}
1	-0.8	25	341.2
2	0.0	26	382.5 (B_{1g})
3	0.0	27	400.0
4	142.1	28	402.2
5	142.7	29	413.9
6	156.5	30	415.0 (I)
7	159.0	31	415.0 (II)
8	160.6	32	425.7 (A_{3u})
9	166.8 (B_{1u})	33	431.6
10	179.3 (A_{1u})	34	443.5
11	183.3	35	456.1 (B_{2u})
12	188.6	36	466.8
13	200.5	37	469.5
14	213.7	38	494.5
15	214.1	39	503.8
16	227.8	40	505.9
17	238.9	41	570.1
18	241.1	42	579.9 (B_{3u})
19	246.9	43	603.8
20	287.6	44	608.2
21	288.5	45	612.0
22	288.8	46	612.6
23	329.8 (A_g)	47	648.8
24	340.9 (A_{2u})	48	649.1 (B_{2g})